Advanced Magnetic Nanomaterials and Nanotechnology for Applications of Nuclear Radiation Detection and Ultrahigh Frequency Electronics

A Dissertation

Presented in Partial Fulfillment of the Requirements for the

Degree of Doctor of Philosophy

with a

Major in Physics

in the

College of Graduate Studies

University of Idaho

by

Lokendra Raj Khanal

Major Professor: You Qiang, Ph.D.

Committee Members: Ruprecht Machleidt, Ph.D.; Indrajit Charit, Ph.D.; Yuehe Lin, Ph.D.

Department Administrator: John Hiller, Ph.D.

May 2020

Authorization to Submit Dissertation

This dissertation of Lokendra R. Khanal, submitted for the degree of Doctor of Philosophy with a Major in Physics and titled "Advanced Magnetic Nanomaterials and Nanotechnology for Applications of Nuclear Radiation Detection and Ultrahigh Frequency Electronics" has been reviewed in final form. Permission, as indicated by the signatures and dates below, is now granted to submit final copies to the College of Graduate Studies for approval.

Major Professor: _____ Date: _____

You Qiang, Ph.D.

Committee Members: _____ Date: _____

Ruprecht Machleidt, Ph.D.

_____ Date: _____

Indrajit Charit, Ph.D.

_____ Date: _____

Yuehe Lin, Ph.D.

Department

Administrator: _____ Date: _____

John Hiller, Ph.D.

Abstract

This dissertation presents the study on novel magnetic nanoparticles (NPs) with unique structure-property relationship. Iron based magnetic NPs for this study have been synthesized using nanocluster deposition system by soft and energetic landing on the surface of silicon substrates, and studied with respect to their nanostructures, morphologies, sizes, shapes and magnetic and electric properties for two different projects: (i) advanced nano-sensor and monitoring of radiation detection for nuclear energy applications at high temperature, and (ii) advanced magnetic nanomaterials for ultrahigh frequency electronics.

In order to test the NPs compatibility for nuclear radiation detection and monitoring at high temperature, the iron-based NPs prepared using nanocluster deposition techniques by soft landing on silicon substrates were heat treated in argon, oxygen and vacuum environment up to 800 ^{0}C. The structure-property relationship pre- and post- heat treatment of the NPs have been studied. The NPs have shown stable morphology, shapes, phase and structure even up to 800 ^{0}C in vacuum environment. The results from the high temperature test and previous in-situ radiation tests are very promising for the application of the NPs as a radiation sensing material for monitoring radiation fluxes in the high temperature core of the nuclear reactors

A new CMOS-integration compatible soft magnet is developed by applying energetic impact of Fe/Fe_3O_4 core-shell nanoparticles onto tilted Si substrates for ultrahigh frequency applications. At room temperature, the in-plane uniaxial anisotropy is induced and tuned, which is interpreted by the uniaxial shape anisotropy of the ellipsoidal nanoparticles and the nanoparticle assembly alignment. Meanwhile, excellent magnetic softness and large resistivity are obtained in the nanocomposites at 5 kV. The good and adjustable uniaxial anisotropy and magnetic softness have been obtained with the large resistivities demonstrating excellent potential for high-frequency performance in miniaturized electronic devices for next generation (5G and 6G) wireless network.

Acknowledgements

I would like to extend my deep and sincere gratitude to my advisor Dr. You Qiang for providing me the opportunity to conduct my Ph.D. research in the nanophysics lab at the University of Idaho (UI). I am extremely grateful for his constant support and motivation, valuable advice and timely guidance, which encouraged me to successfully continue with my studies and to perform research effectively. Without his guidance and persistent support, this dissertation would not have been possible.

I would like to acknowledge my dissertation committee members, Dr. Ruprecht Machleidt, Dr. Indrajit Charit, and Dr. Yuehe Lin for taking their precious time in evaluating my dissertation and providing insightful comments. I would also like to acknowledge the department of physics at UI for allowing me to study and work as a teaching assistant.

I owe great thanks to Dr. John S. McCloy from Washington State University (WSU) for his great ideas and collaboration as well as allowing me to use vibrating sample magnetometer in his lab. I also would like to thank Dr. Mostafa Ahmadzadeh from WSU for his support to conduct magnetic measurement.

Additionally, I am grateful to Dr. Thomas William for training me to use transmission electron microscope, scanning electron microscope, x-ray diffractometer and energy dispersive x-ray spectrometer in electron microscopy lab and allowing to use these tools for the characterization of samples.

Special thanks go to our department scientific instrument maker Mr. John Failla and Mr. Brian Petty for their technical help in experiment instrumentation during my Ph.D. study at UI.

My completion of this project could not have been accomplished without the support of my lab colleague Dr. Jennifer Anand Sundararajan, who have continuously supported and guided me in using the nanocluster deposition system, vibrating sample magnetometer and in troubleshooting of these tools. I would like to thank my fellow group members and friends Dr. Huijin Zhang (Jin), Mr. Mohammad Khan, Mr. Ahmed Alalnazi, Mr. Jeremiah Chapleski and Mr. Carlos Munoz for their

constant support and cooperation. I would like to convey my special gratitude to Dr. Rabi Khanal, and Dr. Dinesh Thapa for their constant support and motivations.

I would like to thank my family members in particular my wife, Binita Basnet, and my brother, Rabindra Khanal for encouraging me when the time got toughs and motivating me in my career. I would like to thank my parents for all the loves, the values, endless support and encouragement throughout my journey. I am grateful to all my friends in Moscow and Pullman area for their constant support and encouragement.

This research is supported by DOE-FC07-08ID14926, by the INL-LDRD administered by CAES under the DOE Contract DE-AC07-05ID14517, DOD-AFRL (FA9453-06-1-0355-P1) and DOE-BES (DE-FG02-06ER15777)

Table of Contents

List of Tables

List of Figures

Statement of Contribution

Coauthors for this works are Dr. Thomas William, Dr. Jennifer Sundararajan, Dr. Mostafa Ahmadzadeh, Dr. John S. McCloy, Dr. Qi Yao, and Dr. You Qiang. The conceptualization for this project was supervised by my graduate advisor Dr. You Qiang. Experimental designing, sample fabrication and heat treatment of the samples, all data works and analysis were completed by me. Validation of results was a joint effort by Dr. Sundararajan, Dr. McCloy and Dr. Qiang. The original draft was developed by me, and review and editing were completed as a joint effort by Dr. Ruprecht Machleidt, Dr. Indrajit Charit, Dr. Yuhe Lin, and Dr. Qiang.

Project 1: **Advanced Nano-sensor and Monitoring System of Radiation Detection for Nuclear Energy Applications at High Temperature**

Chapter 1: Introduction to Nuclear Energy and Nanotechnology

1.1. Nuclear Energy Challenges

It has been estimated by the International Energy Agency that world energy consumption will grow by 56% by the end of 2040.[1] Although fossil fuels and natural gas continue to supply most of the world's energy, emission and pollution from these energy sources stand as a major threat to the environment. Moreover, in a few hundred years the world's supply of oil, coal and natural gas will likely run out.[2] Renewable energy[3,4] and nuclear power[5,6] are the world's fastest-growing energy sources, each increasing by 2.5 percent per year, and are considered to be the major sources of energy for the near future. Renewable energy comes from resources such as sunlight, wind, rain, tides, and geothermal heat, which are naturally replenished. However, nuclear energy is attracting revived interest as a potential alternate for electric power generation, as nuclear power is considered to be one of the most efficient, economical, productive and carbon-emission-free power sources.[7] Today, 13-14% of the electricity used worldwide is generated by nuclear power.[2] In the United States of America, 20% of all electricity is provided by nuclear power. The International Atomic Energy Agency (IAEA) predicted that by 2030 the nuclear power capacity could double.[2,7] However, there are challenges involved in all stages of the nuclear fuel cycle, including nuclear fuel extraction and fabrication, fission product capturing, creating robust reactor materials, radiation sensing and monitoring, radioactive waste separation and spent nuclear fuel reprocessing. Storage of nuclear waste is an environmental issue, hence storage and reprocessing of spent nuclear fuel is essential.[8,9] Reprocessing of spent nuclear fuel can be an economically viable option as it reduces high radioactive load in nuclear waste repositories.[10] In addition, during fuel burn-up the formation of fission products and production of radiation-induced defects pose operational risks. The key to solving this issue lies in extracting, synthesizing and fabricating advanced nuclear fuels with controlled nano-scale structure so that the nuclear waste generation, reprocessing and radiation-induced material degradation can be reduced. During the course of nuclear technological evolution, history has witnessed numerous

accidents due to material degradation,[11] some more severe than those registered in the other non-nuclear power plants.[12] In light of the recent Fukushima Daiichi power plant disaster in Japan (March 2012) and other similar events, a huge responsibility is laid upon scientific communities to quicken their progress, which demand the utmost safety in future generation nuclear power plants to avoid such disaster. Due to such events, public confidence in nuclear power has decreased, which underscores the importance of meeting the highest standards of safety in the operation of existing nuclear power plants and in new designs of advanced nuclear reactors. At the present time, most of the existing reactors are reaching their operational lifetime and the demand for technologies that will sustain the safety of current reactors is critical, including advanced monitoring systems that can quantify the "state of health" of structural materials in the current reactor fleet and predict their residual safe operating life. Such monitoring systems can be integrated into advanced reactors and new builds for inspectability and safety enhancement.

It is clear that improvements are needed for all stages and areas of the nuclear fuel cycle, from nuclear fuel fabrication to used fuel reprocessing, and a slight improvement in each of these areas will certainly contribute to the advancement of performance and safety in nuclear energy systems. In its Research and Development Roadmap - Report to Congress dated April 2010, the Department of Energy's (DOE) Office of Nuclear Energy clearly identified four research and development objectives, among which include, "Developing technologies and other solutions that can improve the reliability, sustain the safety, and extend the life of current nuclear reactors," "Develop Improvements in the Affordability of New Reactors," and "Develop Sustainable Nuclear Fuel Cycles" and "Understand and Minimize the Risks of Nuclear Proliferation and Terrorism."[13] Scientific communities around the world are working towards achieving these objectives and demands in various ways, including via Nuclear Nano-Technology (NNT), which is an efficient tool and candidate for achieving the goal of utmost safety and performance. NNT deals with the use of latest engineered-nanomaterials on improving the nuclear power performances and safety in all areas

of nuclear energy production to bring new generations of nuclear power units. A significant contribution in the NNT areas would result in the development of new capabilities that could be useful to nuclear energy, which can help to build devices to support the development of sustainable nuclear fuel cycles, to control their effects and implementations in nuclear power.

1.2. Nuclear Nano-Technology

The ongoing research in the field of NNT based on the areas in nuclear energy are focused on nano-technology engineered fuels, nanomaterials for fission product capturing, nanotechnology aided reactor materials, nano nuclear waste separation and nanotechnology enabled radiation sensors, detectors and monitors. The engineered nanoparticles, nanoscale materials, properties, or processes are used to enhance mechanical, chemical, physical, or thermo-hydraulic properties and performance in nuclear energy systems.

NNT addresses the issue of performance and safety from various angles and works in different areas to achieve it. Nanotechnology enabled sensors and/or in-service monitors can directly monitor the properties of a material under extreme conditions, such as radiation, temperature and pressure. Real time investigations of material properties and mechanical response along with corrosion, neutron flux, stress/strain or even chemistry with nominal effect on system performance by significant modification in shape, size, structures and morphology could be utilized for enhanced sensitivity and performance of the nanomaterials. Nanotechnology-based detectors can discriminate between different types of radiations, such as neutron and gamma and have improved response for sensing fissile materials even with very low radiation fluxes. A literature review in chapter 2 deals with the structure and property changes of nanomaterials due to irradiation.

1.3. Magnetic Nanoparticles for Radiation Sensing Application

Magnetic nanoparticles (NPs) are a class of nanoparticles that can be manipulated using magnetic fields. Such particles commonly consist of magnetic materials, often iron, nickel, and cobalt. While nanoparticles are the particles that have sizes smaller than 1 micrometer (typically 1 -

100 nanometer). The basic magnetic property of a magnetic material is demonstrated below as the magnetization (M) of a material vs applied field (H).

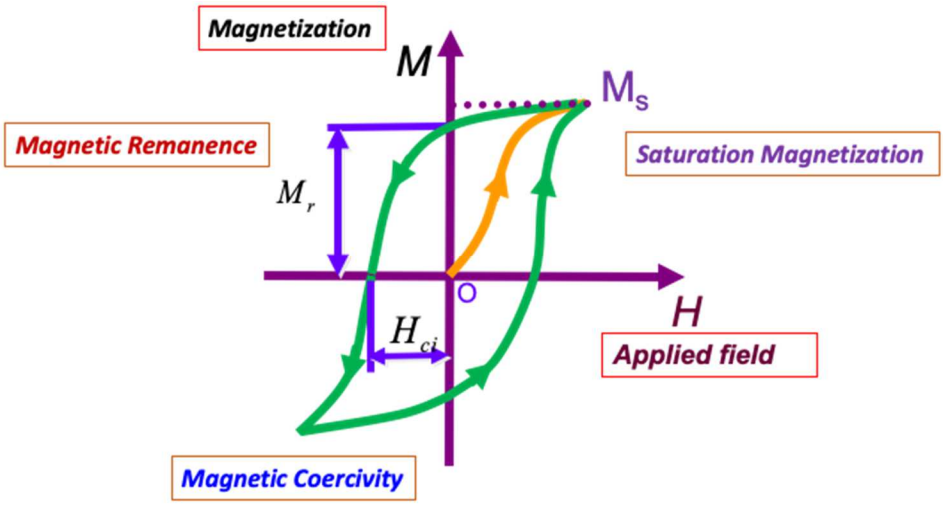

Figure 1.1 Basic magnetic properties

The magnetic properties of NPs are determined by many factors, including the chemical composition, the type and the degree of defectiveness of the crystal lattice, the particle size and shape, the morphology, the interaction of the particle with the surrounding matrix and the neighboring particles. By changing the NP size, shape, composition, and structure, magnetic characteristics of a material can be controlled based on them.

Most recently magnetic NPs have been the focus of irradiation studies for their application as a radiation sensor, detectors and monitors.[14–16] The irradiation induces defects, which are directly or indirectly connected to the atomic level changes. As a result, the electrical and magnetic properties of a magnetic NPs are sensitive under irradiation. Thus, magnetic NPs are the best choice to study the irradiation induced effects at the atomic level for their application as a radiation sensing device, which helps to understand the interfacial behavior and nanoscale interactions under the extreme conditions. The previous results have shown that magnetic NPs are very promising to monitor the radiation fluxes in the nuclear reactors. However, there are lack of knowledge about the response of

the magnetic NPs at high-temperature to monitor the fluxes at the high temperature core of nuclear reactors. This research specifically provides the detailed assessment of interfaces between particles, clusters, crystallites sizes, and particle matrices for Fe-based magnetic NPs at high-temperature. This assessment will be helpful in the future for designing advanced nanodetectors. Applications of such detection and monitoring devices could reduce threats to national security as well as provide integrated health monitoring for next generation nuclear reactors.

1.4. Research Scope

As discussed earlier, there are big safety issues and compatible material challenges in the nuclear power operations. Thus, it is very important to test reactor fuels, structural materials, and radiation sensing material to see their compatibility for their application in nuclear plants to avoid undesirable incidents to happen. This research mainly focuses on the study of Fe-based magnetic nanoparticles at high-temperature for their application as a radiation sensing material in high-temperature core of the nuclear reactor. This research is based on the hypothesis that, "Fe-based magnetic nanoparticles could help us to understand the temperature induced modifications in nanomaterials in a better way or stable materials for nuclear energy applications at high temperature."

The main goal of this research is to understand the temperature induced structural and magnetic property changes, and to develop a fundamental understanding of temperature induced modification in the properties of the granular magnetic films. This research work has been carried out through the following objectives:

- To test the response of Fe-based magnetic nanoparticle at high temperature in the different medium.
- To understand temperature induced nanostructure evolution mechanisms, evolution kinetics, and nanostructure-property relationships.

- To assess the stability and sensitivity of nanomaterials to heat for designing sensors and monitors for safe, and secure nuclear operation.

The results obtained from this study could be useful in the future to generate data for scientific assessments in prediction of the material performance in high temperature environments in the core of the nuclear reactor. The prior work in this area has observed significant challenges associated with extreme local heating of the sensing material, such as actinide-bearing oxide coated films, including melting and potentially vaporization, which add risk to the deployment of such films in fission chamber.[17] The Fe-based magnetic nanomaterials chosen in this research avoid such challenges due to the absence of fissionable material.

1.5. References

(1) Wolfram, C.; Shelef, O.; Gertler, P. How Will Energy Demand Develop in the Developing World? *J. Econ. Perspect.* **2012**, *26* (1), 119–137.

(2) Kharecha, P. A.; Hansen, J. E. Prevented Mortality and Greenhouse Gas Emissions from Historical and Projected Nuclear Power. *Environ. Sci. Technol.* **2013**, *47* (9), 4889–4895.

(3) Holm, D.; Arch, D. Renewable Energy Future for the Developing World. *Int Cong Renew Energy 2006 Proc ICORE-2006 Feb* **2006**, 8–11.

(4) *Energy for the Future: Renewable Sources of Energy*; com(97)599; European Commission, 1997.

(5) Ferguson, C. D.; Marburger, L. E.; Farmer, J. D.; Makhijani, A. A US Nuclear Future? **2010**, *467*, 391–393. https://doi.org/10.1038/467391a.

(6) Guérin, Y.; Was, G. S.; Zinkle, S. J. Materials Challenges for Advanced Nuclear Energy Systems. *MRS Bull.* **2009**, *34* (1), 10–19. https://doi.org/10.1017/S0883769400100028.

(7) Ferguson, C. D. Do Not Phase out Nuclear Power–yet: Fission Power Must Remain a Crucial Part of the Energy Mix until Renewable Energy Technologies Can Be Scaled Up. *Nature* **2011**, *471* (7339), 411–412.

(8) Markandya, A.; Wilkinson, P. Electricity Generation and Health. *The Lancet* **2007**, *370* (9591), 979–990.

(9) O'BRIEN, J. N. International Auspices for the Storage of Spent Nuclear Fuel as a Nonproliferation Measure. *Nat. Resour. J.* **1981**, *21* (4), 857–894.

(10) Nikitin, M. B. D. *Managing the Nuclear Fuel Cycle: Policy Implications of Expanding Global Access to Nuclear Power*; DIANE Publishing, 2009.

(11) Diercks, D. R. Analysis of Failed Nuclear Plant Components. *J. Mater. Eng. Perform.* **1993**, *2* (6), 799–806.

(12) Sovacool, B. The Accidental Century: Prominent Energy Accidents in the Last Hundred Years. *Explor. Prod. Oil Gas Rev.* **2009**, *7* (2), 132–137.

(13) *US Department of Energy Nuclear Energy Research and Development Roadmap - Report to Congress.*; Office of Nuclear Energy, 2010.

(14) Khanal, L. R.; Williams, T.; Qiang, Y. High-Temperature Investigation on Morphology, Phase and Size of Iron/Iron-Oxide Core-Shell Nanoclusters for Radiation Nanodetector. *J. Phys. Appl. Phys.* **2018**. https://doi.org/10.1088/1361-6463/aac47e.

(15) Jiang, W.; McCloy, J. S.; Lea, A. S.; Sundararajan, J. A.; Yao, Q.; Qiang, Y. Magnetization and Susceptibility of Ion-Irradiated Granular Magnetite Films. *Phys. Rev. B* **2011**, *83* (13), 134435.

(16) Sundararajan, J. A.; Kaur, M.; Jiang, W.; McCloy, J. S.; Qiang, Y. Oxide Shell Reduction and Magnetic Property Changes in Core-Shell Fe Nanoclusters under Ion Irradiation. *J. Appl. Phys.* **2014**, *115* (17), 17B507.

(17) Imel, G. R.; Poenitz, W. P.; Snyder, A. M. Measurement of Fission Fragment Induced Fluorescence in Xenon. *Nucl. Instrum. Methods Phys. Res. Sect. B Beam Interact. Mater. At.* **1995**, *103* (1), 1–14. https://doi.org/10.1016/0168-583X(95)00564-1.

Chapter 2: Literature Review on Radiation Nanodetectors and Monitors

Khanal, L. R.; Sundararajan, J. A.; Qiang, Y. Advanced Nanomaterials for Nuclear Energy and Nanotechnology. *Energy Technology*, 1901070. https://doi.org/10.1002/ente.201901070.

2.1. Introduction

Radiation is a process by which energy produced in the form of waves or particles by a body propagates through space or through a material medium, essentially to be absorbed by another body. Radiation interacts with matter following the fundamental interactions of our nature, primarily through the electromagnetic (for charged particles and photons) and strong (for hadrons) interactions. Radiation can be broadly classified into two types: ionizing radiation and non-ionizing radiation. In ionizing radiation, the energy carriers interact with a physical medium to produce ion pairs, for example, α, β, X, γ-radiation, neutron, proton, pion, muon, etc. These ion pairs are invisible to humans such that their detection requires a suitable monitoring instrument. Although neutrons are neutral particles, they do not ionize directly. Instead, they produce ions through secondary mechanisms. In non-ionizing radiation, the energy carriers do not produce ion pairs in a physical medium, i.e. soft ultra-violet, infra-red, visible light, microwave, radio-frequency, etc. Ionization can be caused only through charged particles through Columbic interactions (Electromagnetic Interaction). Neutrons are harder than charged particles to detect directly. Furthermore, their paths of motion are not affected much by electric and magnetic fields. Hence, neutrons produce ions through secondary mechanisms, which are then detected. Neutrons react with matter through

I. Elastic scattering producing a recoiling nucleus
II. Inelastic scattering producing an excited nucleus, or absorption with transmutation of the resulting nucleus.

Most detection approaches rely on detecting the various reaction products. Inelastic scattering includes the absorptive reactions and activation processes. Low energy neutrons (thermal neutrons)

are typically detected indirectly through absorptive reactions. Ideal absorber materials used have high cross sections for absorption of neutrons and include helium-3, lithium-6, boron-10, and uranium-235. These react by emission of high energy ionized particles, the ionization track of which can be detected by various methods. In activation processes, neutrons may be detected when they react with absorbers in a radiative capture, spallation or similar reaction, producing reaction products that then decay at some later time, releasing beta particles or gammas which are then detected. In elastic scattering reactions, neutrons transfer energy to the nucleus of material, creating ions, which are then detected.

Nano-technology enabled sensors and/or in-service monitors can directly monitor for radiation, temperature, pressure, in situ diagnostics of material properties and mechanical response, corrosion, neutron flux, stress/strain or even chemistry with little effect on system performance with significantly reduced size and weight and increased sensitivity, performance, and functionality. Nanotechnology-based detectors can discriminate between neutron and gamma radiation and/or have enhanced sensitivity for the detection of fissile materials with very low neutron activation fluxes.

J. W. Murphy *et al*.[1] investigated the optimal thickness of a semiconductor diode for thin-film solid state thermal neutron detectors. They investigated a coplanar diode/converter geometry to determine the minimum semiconductor thickness needed to achieve maximum neutron detection efficiency. They kept the semiconductor thickness to a minimum, and gamma rejection as high as possible. In this way, detector performance is optimized for different thin-film semiconductor materials. Based on their simulations, they were able to provide a range of diode thicknesses and materials to design an optimal neutron. Diamond and ZnO renders[1] are the greatest stopping power for charged particles, typically requiring only half the thickness of Si to achieve maximum intrinsic thermal neutron detection efficiency. They found that Si possesses the best gamma rejection capability for a given thickness, even greater than that of diamond.

E. Tupitsyn *et al*.[2] reported the use of single crystals of semiconductor-grade lithium indium selenide ($LiInSe_2$) for detecting neutron irradiation. Nuclear radiation devices were fabricated, and alpha particle detection was observed. This suggests that this material could be a candidate for neutron detection application. The crystal showed a high bulk resistivity suitable for nuclear radiation detection. Photocurrent is well pronounced at 445 nm and suggests an ideal generation rate and mobility of the charge carriers. The response showed by the $LiInSe_2$ crystal to alpha particle radiation makes them potential candidate for neutron detection. In depth study for the improvement of crystal quality and defect structure may improve alpha particle detection significantly.

2.2. Electrical Conductivity for Radiation Sensing

Jiang *et al*,[3] in 2014, reported an in-situ study on the structural evolution in Fe-based nanocluster films under Si^{2+} and He^{+} ion irradiation using an advanced helium ion microscope. The films consist of loosely interconnected crystalline nanoclusters of magnetite or iron-magnetite (Fe-Fe_3O_4) core-shells synthesized by the state-of-the-art cluster deposition technique.[4,5] The nanostructure is observed to undergo a dramatic change under ion-beam irradiation, featuring grain growth, phase transition, particle aggregation, and formation of a nanowire-like network and nano-pores. Major structural evolution is discovered to be activated by elastic nuclear collisions, while both electronic and thermal processes may play some roles once the evolution starts. The electrical resistance of the Fe-Fe_3O_4 films measured *in situ* by Van-der Pauw four probe method exhibits a super-exponential decay with radiation dose as shown in Figure 2.1. It was reported that the very sensitive electrical resistance under ion irradiation is the result of the significant change in the nanostructures and morphologies of the film. Further, we performed high temperature testing on the iron/iron-oxide core-shell nanoclusters prepared in a similar method to simulate the high-temperature core of the reactor plant and observed stable core-shell structure of the nanoclusters in vacuum environment accompanied by the particle size growth.[6] However, the nanoclusters lost their core-shell structure in the argon and oxygen environments due to the transport of the Fe-core and the oxygen

interstitial based on the Cabrera-Mott model.[7–9] Since the core of the nuclear reactor is a vacuum, the report suggests that the material possesses an intrinsic merit for development of an advanced online monitor for neutron radiation with high-sensitivity detection in- and out-core of the reactor plant, and long-term applicability, which enhances safety measures in many nuclear operations.

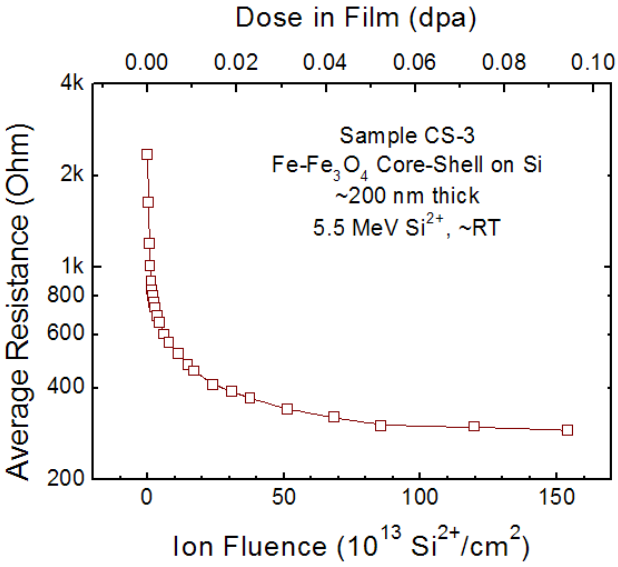

Figure 2.1 Electrical resistance of a Fe-Fe_3O_4 core-shell nanocluster film on surface oxidized Si measured in situ using Van der Pauw method as a function of ion fluence during 5.5 MeV Si^{2+} ion irradiation at nominal RT. A super exponential decay behavior of the resistance is observed[3]

2.3. Magnetic Properties of Nanomaterials for Radiation Sensing

Detecting radiation based on magnetic properties has gained more attention recently and it could be a good non-destructive testing technique. Recent research in the field of radiation-induced magnetic property changes on nanomaterials has produced fruitful results for the scientific community. The results and data vary based on the type of irradiation and type of materials irradiated. Most prominently, the exposure to heavy ion irradiation, like that from Helium ions, Silicon ions and Argon ions on a variety of targets ranging from nanocomposites to granular films, has helped us to understand the underlying truths behind irradiation-induced property changes in nanomaterials to

some extent. Among these results, some of the most notable changes in nanomaterials due to irradiation are enhancement of ferromagnetic behavior, enhanced magnetization, enhanced anisotropy, grain size growth, domain growth, oxide layer thickening, alteration of electronic configuration, migration of defect, and changes in crystal structure. This section presents a brief review of articles, which deal with these astonishing changes in magnetic properties of nanomaterials due to radiation exposure.

2.3.1. Barkhausen Noise

The Barkhausen effect, discovered by German physicist Heinrich Barkhausen in 1919, is the noise in the magnetic output of a ferromagnet when the magnetizing force applied to the magnet is changed. It is a series of sudden changes in the size and orientation of ferromagnetic domains, or microscopic clusters of aligned atomic magnets (spins), that occurs during a continuous process of magnetization or demagnetization. It confirms the existence of ferromagnetic domains, which previously had been postulated theoretically.

D. G. Park *et al.*[10] reported that the coercive force of B-H hysteresis loop showed a moderate change up to a neutron dose of 10^{14} n/cm^2 and increased by 15.4% for a 10^{16} n/cm^2 dose sample when compared with unirradiated one, associated with the domain wall motion obstructed by increased defects. However, the amplitude of Barkhausen noise reflecting the wall motion decreased slowly up to 10^{14} n/cm^2 irradiation, accompanied by a rapid decrease of 37.5% at 10^{16} n/cm^2. This suggests that the Barkhausen noise is more responsive to the damage of neutron irradiation than conventional magnetic properties, such as maximum induction, coercive force and remanence.

2.3.2. Enhancement of Ferromagnetism

W. Jiang *et al.*[11] reported that the Fe_3O_4 nanocluster granular films, which were initially superparamagnetic, became ferromagnetic following Si^{2+} ion irradiation of fluence 10^{16} ions/cm^2. It was reported that a significant increase in the grain size and a dramatic change in the nanostructure were observed. These films represent a new class of semi-disordered magnetite materials for study,

which could lead to important applications of this type of materials in various areas, including radiation detection and monitoring. Ašmontas *et al*.[12] reported the use of semiconductor nanostructures for microwave and terahertz radiation. They investigated the properties of the planar diodes fabricated on the base of selectively doped AlGaAs/GaAs structures. It was inferred that homogeneous distribution of impurities doped in the AlGaAs layer can be used to detect microwave radiation in wide frequency range and by fine tuning the doping, the voltage sensitivity of the planar diode could be modulated to almost 10 times.

The transition from diamagnetic or paramagnetic state to ferromagnetic state due to irradiation is one of the most fascinating behaviors in nanostructured materials. Although irradiation is well known to cause various undesirable changes in magnetic nanostructures, radiation-induced ferromagnetic behavior is an interesting phenomenon, which opens a new door for many applications. P. Esquinazi *et al.*[13] in their article "Induced magnetic ordering by proton irradiation in graphite" reported the enhancement of ferromagnetic behavior in micro-sized Highly-Ordered Pyrolytic Graphite (HOPG) upon proton irradiation on different spots of the sample with incident energy 2.25 MeV, with a radiation dose of 0.99 pC/μm^2 to 0.3 nC/μm^2 and a charge of 2.93 μC to 600 μC. Figure 12 (a) shows the hysteresis loop measured between +10 KOe to -10 KOe at room temperature for increased irradiation.

It was observed that the ferromagnetic behavior and magnetization not only increased with increasing irradiation-enhanced magnetic ordering, but also decreased over prolonged irradiation exposure because of magnetic disordering. This suggests that prolonged irradiation can decrease ferromagnetic behavior and magnetization. Although the number of points is too small to deduce a relationship between saturation moment (m_s) and implanted charge (C_t), the available results indicate a linear relationship of the type $m_s \alpha (C_t)^{1/2}$. No significant changes in ferromagnetic loops were inferred when the hysteresis loops were measured at different temperatures (5 K, 300 K and 380 K),

which conveys the fact that the Curie temperature of the irradiated sample should be high above 400 K.

S. Talapatra *et al,*[14] in 2005, reported the enhancement of ferromagnetic behavior due to the irradiation of N and C ions in nano-sized diamonds (ND). ^{15}N and ^{12}C ions with implant energy of 100 KeV were irradiated on ND particles at difference doses ranging from 10^{12} to 5×10^{16} ions/cm^2, as a result of which the N and C ions were implanted in the ND matrix, which was the ultimate cause for the enhanced ferromagnetic behavior in the pristine ND sample, which is diamagnetic by nature.

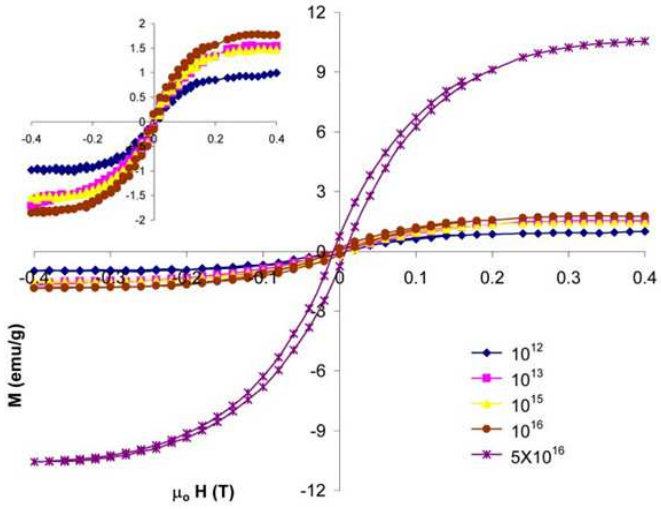

Figure 2.2 Hysteresis loops of ^{15}N implanted nano diamonds irradiated at different fluence. The subset shows the ferromagnetic behavior of sample at low dose of irradiation. [14]

Figure 2.2. shows the hysteresis loop from the ^{15}N implanted NDs for various doses. Though at lower doses the increase in the magnetic saturation is not very pronounced, the data shows evidence that all the implanted samples exhibit ferromagnetic behavior. The subset in Figure 2.2. shows the established ferromagnetic behavior at low dose radiation. It was found that a higher value of the saturation magnetization is inferred under ^{15}N irradiation than the ^{12}C irradiation, which could be due to the extensive defect generation, due to the formation of C-N bond and interaction between them.

This sort of enhanced ferromagnetic behavior was also observed in a recent investigation by Sundararajan *et al*.[15] Core-shell (CS) Fe-Fe_3O_4/Fe_3N nanocluster films were prepared using a nanocluster deposition system and the grazing incidence X-ray diffraction (GIXRD) confirmed the presence of Fe_3O_4 phase in the shell of unirradiated CS film with iron nitride phase undetected due to its amorphous state or small size. Hysteresis loops of the CS Fe-Fe_3O_4/Fe_3N NC film, unirradiated (as-prepared) and irradiated to 10^{15} and 10^{16} ions/cm^2 are shown in Figure 2.3. The CS Fe-Fe_3O_4/Fe_3N film has a relatively high saturation magnetization (M_S) of 50 emu/g due to the Fe core, a coercivity (H_C) of 220 Oe and a remanence of 5 emu/g. The CS Fe-Fe film retained its Fe core and its ferromagnetic properties even after irradiation up to 10^{15} ions/cm^2 and 10^{16} ion/cm^2. At the fluence of 10^{15} ions/cm^2, the formation of anti-ferromagnetic FeO causes the M_S to drop but not that much because of the simultaneous crystallization of ferromagnetic Fe_3N. Prolonged irradiation up to 10^{16} ions/cm^2 led to grain grown and aggregation of particles contributing to the increase of M_S and H_C. In addition to that, the formation of Fe_4N phase at 10^{16} ion/cm^2 stands as the major reason behind the increase of M_S, since Fe_4N compound naturally has a very high saturation magnetization (184 emu/g) close to that of Fe.

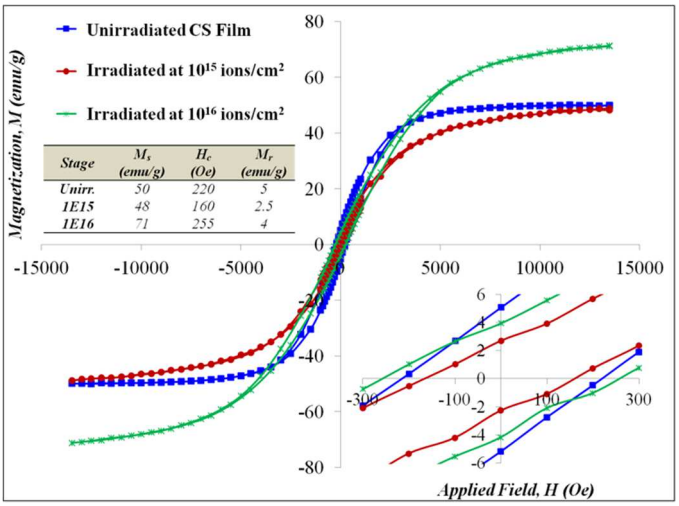

Figure 2.3 Magnetic hysteresis loops for the core-shell Fe-Fe_3O_4/Fe_3N NC film, unirradiated (as-prepared) and irradiated to 10^{15} and 10^{16} ions/cm^2. The inset shows a magnified view near zero fields.[15]

Although in this CS nanoparticle film, a reduction of Fe_3O_4 to FeO and crystallization of iron nitride or growth of Fe_3N occur after 5.5 MeV Si^{2+} ion irradiation with retention of ferromagnetic nature, similar reduction behavior was not observed in other films of Fe_3O_4, FeO+Fe_3N or Fe_3O_4+FeO+Fe_3N. The reduction is attributed to the presence of the nanocrystalline Fe core that possibly serves as a catalyst. The core-shell Fe-Fe_3O_4/Fe_3N film retained its Fe core and its ferromagnetic nature even after irradiation. Helium Ion Microscopy (HIM) study shows cluster aggregation in the films, resulting in surface smoothening and material densification. This study helps in understanding the actual mechanisms and the contributing factors for the radiation-induces magnetic property changes in nanomaterials.

2.3.3. Impact on size, shape and anisotropy

It is interesting to see that irradiation exposure not only alters the magnetic behavior of the samples but also has a huge impact on the size, shape and anisotropy of the nanoparticle under irradiation. Particle size and shape plays a vital role in elaborating the coercivity, anisotropy and magnetic interactions. In 2004, C.D. Orleans *et al.*[16] reported particle size growth and prolate

deformation in Co nanoparticles implanted in SiO_2 matrix due to the irradiation of 160 KeV Iodine (^{127}I) ions to a fluence ranging from 10^{11} to 10^{14} ions/cm^2. When irradiated with ^{127}I ions and fluence from 10^{11} to 10^{13} ions/cm^2, the Co nanoparticles showed an increase in coercivity (i.e. increase in particle size) with no change in anisotropy with respect to parallel and perpendicular axes (i.e. no deformation or change of particle shape). The TEM images obtained supported this fact for an increase in particle size with no deformation with increasing radiation fluence. But radiation fluence beyond 10^{13} ions/cm^2 caused the particles to deform and produce a prolate shape by elongating in the direction parallel to the incident beam, thereby showing anisotropic behavior with respect to parallel and perpendicular axes, which was confirmed from the TEM images.

As stated in the literature, the reason for this size growth and elongation is due to the two main processes of 'Fragmentation' and 'Deformation'. The fragmentation process is influenced by 'Ostwald Ripening', in which the nanoparticle aggregates break and recombine with neighboring aggregates to form larger nanoparticles. The deformation process is influenced by the elongation of nanoparticles along the irradiating ion track after reaching a critical radius in the nanoparticles. This behavior calls for an intuitive assumption that particle size growth is not always the case with increasing radiation, but there exists a critical size limit beyond which the particles stop growing and begin to deform with no change in volume, showing anisotropic behavior in the nanoparticles. The deformation process was believed to have been created by the localized temperature increase and localized melting due to a thermal spike, which happened rapidly, on the order of pico (10^{-12}) and nano (10^{-9}) seconds. This sort of induced anisotropic behavior due to irradiation was also reported by J.P. Nozieres *et al*[17] in 1998 when YCo_2 targets were irradiated with Uranium (U) ions with stopping power (55 KeV/nm) at a total fluence of 10^{12} ions/cm^2. The hard axis anisotropy was found to double the times of easy axis anisotropy after irradiation. Though there are many other contributing factors to the enhancement of anisotropy in nanostructures, increase in particle size and shape has been proven to be a prime factor to enhance anisotropy. The research by W. Jiang *et. al.*[11] also deals with the

increase in particle size and increase in domain wall size due to irradiation in magnetite granular films. On the contrary, irradiation exposure was found to reduce particle size as reported by L.G Jacobsohn *et al.*[18] and J. Ferre *et al.* They quoted the decrease in coercivity as evidence for this behavior and reported that reduced particle size was due to the process of 'Inverse Ostwald Ripening'. However, more work is needed to investigate this effect.

2.3.4. Enhancement of Magnetization

Though enhancement of saturation magnetization (M_s) in nanostructures goes along with enhancement of ferromagnetism, increase in saturation magnetization is a unique behavior because it deals more specifically with magnetic moments due to magnetic ordering and magnetic nanoparticle interaction. In confirmation of the above-mentioned fact, the ferromagnetic samples when exposed to irradiation have been found to show improvement in magnetization. Surprisingly, as discussed earlier, even diamagnetic and paramagnetic samples, after gaining ferromagnetic behavior due to primary irradiation, continued to show improvement in saturation magnetization due to secondary irradiation until they reached a certain critical level. P. K. Kulriya *et al*[20] reported the enhanced magnetic saturation of Pd nanoparticles embedded in a carbon matrix when irradiated by Au ions with an energy of 120 MeV at fluence of 5×10^{13} ions/cm^2. A large enhancement of about 20 times in the saturation magnetization was observed in the irradiated sample in comparison to the pristine sample when the hysteresis loops were measured in a Super Conducting Quantum Interference Device (SQUID) magnetometer.

A detailed study with X-ray Magnetic Circular Dichroism (XMCD) in the irradiated samples revealed that the increase in lattice strain, increase in defect density, modification in lattice structure due to large electronic energy loss, and ionization of atoms due to inelastic collision between incident ions and electrons were the main reasons behind the fascinating Ms increase in the irradiated samples. In 2010, C. Gavade *et al.*[21] experienced the enhancement of magnetization when NiO embedded in

Polymethyl Methacrylate (PMMA) matrices were irradiated with 50 MeV Li^{+3} ions at a fluence of 5×10^{12} ions/cm^2. The Field Cooled and Zero Field Cooled (FC-ZFC) measurements carried out in the temperature range 10 K - 320 K at 0.05 T applied field for pristine and irradiated sample showed 25% increase in magnetization. The creation of free radicals was reported to be the reason behind the increase in Ms of the sample. A study conducted by the group using Fourier Transform Infrared (FTIR) spectroscopy and Atomic Force Microscope (AFM) revealed that the interaction between particles, surface roughness, and magnetic interactions played a vital role in enhancing the saturation magnetization of the sample.

2.3.5. Influence on Curie temperature

The Curie temperature (T_c) or Curie point is the temperature at which a ferromagnetic or a ferrimagnetic material becomes paramagnetic upon heating and the effect is reversible. As reported by J. Ferre *et al.*[19], radiation exposure on Pt/Co/Pt ultrathin films was proved to reduce the Curie temperature near to room temperature, which originally was above 400 K. Pt(3.4nm)/Co(0.5nm)/Pt(6.5nm) sandwiched ultrathin films exposed to 30 KeV He^+ ions with fluence between 2×10^{14} to 2×10^{16} ions/cm^2 showed a huge decrease in coercivity. The Magneto Optical Kerr Effect (MOKE) hysteresis loops on samples irradiated with 30 KeV He^+ ions at fluence 10^{16} ions/cm^2 for different temperatures showed a clear magnetic transition occurring somewhere between 322 K and 342 K.

From the shape of the curve, the remnant magnetization and the coercivity values, it becomes very clear that a ferromagnetic to paramagnetic transition occurs with respect to increase in temperature. The data point shows more specifically that the Curie temperature is exactly at 336 K even though the Curie temperature of the original sample was well above 400 K. This conveys the fact that increased radiation could bring the T_c to room temperature or even below room temperature, which is a fascinating behavior in ferromagnetic materials due to irradiation.

2.4. Oxide Layer Thickening on Nanoparticle

In many cases of radiation sensing, the sample involved ends up getting completely damaged while sacrificing the material's integrity directly or indirectly for sensing radiation. Another elegant way to sense radiation without sacrificing the overall integrity of the nanomaterials is through tracking the phase changes that occur on the oxide shells of core-shell nanoparticles. The benefit of having an oxide shell is to promote the effect of grain boundaries and interface, which naturally tends to protect the core as discussed earlier. Therefore, just tracking the changes of the oxide shell alone while most of the core remain unchanged is a unique way to sense radiation. Oxide layer thickening or continuous oxidation of the core-shell nanoparticles and pure nanoparticle under irradiation have been reported by a number of researchers. In all these cases, irrespective of the type of materials, oxide layer thickening was caused either due to the influence of temperature or due to the exposure to irradiation. Jaffari *et al.*[22] reported the continuous oxidation of $NiFe_2O_4$ nanoparticles in the atmosphere and formation of a void at the center due to temperature increase. The mechanism behind the temperature-induced oxidation was explained to be due to the Kirkendall effect.[23] Heilmann *et al*[24] reported the oxidation of indium particles embedded in a plasma-polymer thin film matrix due to electron beam irradiation. Thermal annealing of the samples was believed to be the reason behind the oxidation of In to In_2O_3. Literatures[25,26] reported that the thickening of oxide layers core-shell iron nanoparticle could be due to the electron beam radiation-induced defect mediated mass transport process. We reported the formation of voids in iron nanoparticles due to continuous oxidation and discussed in detail the structural and electronic properties of iron oxides.[27–29] Even though a huge number of observations on oxide layer thickening has been reported, the peculiar process that puzzled the scientific community for decades is the mechanism behind the thickening of the oxide layer of core-shell nanoparticles in TEM and Scanning Electron Microscopy (SEM) environments, where they are constantly exposed to electron beam (E-beam) irradiation. Detailed explanations of the mechanism of oxidation due to electron beam irradiation and its possibilities were missing from the

literature. Investigations done in our lab as a part of this research paved a way for cracking the mechanism behind oxide layer thickening. Through the investigation, it was proven that continuous growth of oxide layers in core shell nanoparticles is plausible under continuous exposure of E-beam irradiation through the defect-mediated mass transport process. Based on the experimental fact and the theory of radiation defects, we have made clear that the most dominating processes in the thickening of the oxide layer are the vacancy/void formation and atom/vacancy diffusion enhanced by localized high temperature increase. As in the case of electron beam lithography, the process of 'dissociative electron attachment' enables the breaking of chemical bonds, which in turn helps the surface oxidation of the nanoparticles. The water molecules and hydrocarbons that stick to the surface of the TEM grids also play a vital role for the availability of oxygen in a high vacuum TEM environment. The electron beam radiation on core shell nanoparticles, as in the case of TEM measurement, not only increases the oxide layer thickness but also increases the overall size of the nanoparticles, apparently resulting in property change. Depending on the intensity of the electron beam and the radiation environment, the rate of oxide layer thickening will vary and will continue to grow by undergoing the electron beam-induced defect-mediated mass transport process.

2.5. Conclusion

The creation of various novel nanostructured materials for Nuclear Nano-Technology (NNT) comes from the tremendous basic research that is an essential need for future advanced nuclear energy systems. This literature review highlights studies providing new understanding of radiation detectors and monitors from nanostructures and behaviors of nano-devices and novel nanomaterials. The new insights of nanodevices can be incorporated for designing and fabricating radiation detection and sensing devices utilizing nanotechnology. The major contribution of radiation tolerance comes from interfaces and grain boundaries in the nanomaterials. These ranges of approaches will help to understand structure-property relationships from new perspectives in nuclear radiation detections. The understanding can be incorporated in future works to design nanomaterials for radiation sensing and

detection applications in nuclear reactor plants for the safe and enhanced production of nuclear energy. Overall, we are able to conclude that nanomaterials and nanotechnologies have potential applications as radiation nanosensors for secure nuclear energy technology. Undoubtedly, they will play critical roles in future generation advanced nuclear energy systems. However, the research of nanomaterials and nanotechnologies in the field of nuclear energy has just been started. Further research and testing are still a critical need to avoid various scientific hindrances. Escalating further research work with in-depth understanding is the most we can do for now to utilize the advantages derived from the nanomaterials and nanotechnologies in the upcoming generation of nuclear reactors.

2.6. References

(1) Murphy, J. W.; Kunnen, G. R.; Mejia, I.; Quevedo-Lopez, M. A.; Allee, D.; Gnade, B. Optimizing Diode Thickness for Thin-Film Solid State Thermal Neutron Detectors. *Appl. Phys. Lett.* **2012**, *101* (14), 143506.

(2) Tupitsyn, E.; Bhattacharya, P.; Rowe, E.; Matei, L.; Groza, M.; Wiggins, B.; Burger, A.; Stowe, A. Single Crystal of LiInSe2 Semiconductor for Neutron Detector. *Appl. Phys. Lett.* **2012**, *101* (20), 202101.

(3) Jiang, W.; Sundararajan, J. A.; Varga, T.; Bowden, M. E.; Qiang, Y.; McCloy, J. S.; Henager, C.; Montgomery, R. O. In Situ Study of Nanostructure and Electrical Resistance of Nanocluster Films Irradiated with Ion Beams. *Adv. Funct. Mater.* **2014**, *24* (39), 6210–6218.

(4) Qiang, Y.; Antony, J.; Sharma, A.; Nutting, J.; Sikes, D.; Meyer, D. Iron/Iron Oxide Core-Shell Nanoclusters for Biomedical Applications. *J. Nanoparticle Res.* **2006**, *8* (3–4), 489–496. https://doi.org/10.1007/s11051-005-9011-3.

(5) Kaur, M.; McCloy, J. S.; Jiang, W.; Yao, Q.; Qiang, Y. Size Dependence of Inter- and Intracluster Interactions in Core–Shell Iron–Iron Oxide Nanoclusters. *J. Phys. Chem. C* **2012**, *116* (23), 12875–12885. https://doi.org/10.1021/jp301453w.

(6) Khanal, L. R.; Williams, T.; Qiang, Y. High-Temperature Investigation on Morphology, Phase and Size of Iron/Iron-Oxide Core-Shell Nanoclusters for Radiation Nanodetector. *J. Phys. Appl. Phys.* **2018**. https://doi.org/10.1088/1361-6463/aac47e.

(7) Linderoth, S.; Mørup, S.; Bentzon, M. D. Oxidation of Nanometer-Sized Iron Particles. *J. Mater. Sci.* **1995**, *30* (12), 3142–3148. https://doi.org/10.1007/BF01209229.

(8) Fung, K. K.; Qin, B.; Zhang, X. X. Passivation of α-Fe Nanoparticle by Epitaxial γ-Fe2O3 Shell. *Mater. Sci. Eng. A* **2000**, *286* (1), 135–138. https://doi.org/10.1016/S0921-5093(00)00717-6.

(9) Mott, N. F.; Alexandrov, A. S. *Sir Nevill Mott â 65 Years in Physics*; World Scientific Publishing Company, 1995; Vol. 12.

(10) Park, D. G.; Kim, C. G.; Kim, H. C.; Hong, J. H.; Kim, I. S. Effect of Neutron Irradiation on Magnetic Properties in the Low Alloy Ni-Mo Steel SA508-3. *J. Appl. Phys.* **1997**, *81* (8), 4125–4127.

(11) Jiang, W.; McCloy, J. S.; Lea, A. S.; Sundararajan, J. A.; Yao, Q.; Qiang, Y. Magnetization and Susceptibility of Ion-Irradiated Granular Magnetite Films. *Phys. Rev. B* **2011**, *83* (13), 134435.

(12) Asmontas, S.; Kazlauskaite, V.; Suziedelis, A.; Gradauskas, J.; Sirmulis, E.; Derkach, V. Microwave Conference, 2009; European, 2009; pp 1650–1653.

(13) Esquinazi, P.; Spemann, D.; Höhne, R.; Setzer, A.; Han, K.-H.; Butz, T. Induced Magnetic Ordering by Proton Irradiation in Graphite. *Phys. Rev. Lett.* **2003**, *91* (22), 227201.

(14) Talapatra, S.; Ganesan, P. G.; Kim, T.; Vajtai, R.; Huang, M.; Shima, M.; Ramanath, G.; Srivastava, D.; Deevi, S. C.; Ajayan, P. M. Irradiation-Induced Magnetism in Carbon Nanostructures. *Phys. Rev. Lett.* **2005**, *95* (9), 097201.

(15) Sundararajan, J. A.; Kaur, M.; Jiang, W.; McCloy, J. S.; Qiang, Y. Oxide Shell Reduction and Magnetic Property Changes in Core-Shell Fe Nanoclusters under Ion Irradiation. *J. Appl. Phys.* **2014**, *115* (17), 17B507.

(16) D'orleans, C.; Stoquert, J. P.; Estournes, C.; Grob, J. J.; Muller, D.; Guille, J. L.; Richard-Plouet, M.; Cerruti, C.; Haas, F. Elongated Co Nanoparticles Induced by Swift Heavy Ion Irradiations. *Nucl. Instrum. Methods Phys. Res. Sect. B Beam Interact. Mater. At.* **2004**, *216*, 372–378.

(17) Nozieres, J. P.; Ghidini, M.; Dempsey, N. M.; Gervais, B.; Givord, D.; Suran, G.; Coey, J. M. D. Swift Heavy Ions for Magnetic Nanostructures. *Nucl. Instrum. Methods Phys. Res. Sect. B Beam Interact. Mater. At.* **1998**, *146* (1), 250–259.

(18) Jacobsohn, L. G.; Thompson, J. D.; Wang, Y.; Misra, A.; Schulze, R. K.; Nastasi, M. Effects of Ion Irradiation on Cobalt Nanocomposite. *Nucl. Instrum. Methods Phys. Res. Sect. B Beam Interact. Mater. At.* **2006**, *250* (1), 201–205.

(19) Ferré, J.; Chappert, C.; Bernas, H.; Jamet, J.-P.; Meyer, P.; Kaitasov, O.; Lemerle, S.; Mathet, V.; Rousseaux, F.; Launois, H. Irradiation Induced Effects on Magnetic Properties of Pt/Co/Pt Ultrathin Films. *J. Magn. Magn. Mater.* **1999**, *198*, 191–193.

(20) Kulriya, P. K.; Mehta, B. R.; Avasthi, D. K.; Agarwal, D. C.; Thakur, P.; Brookes, N. B.; Chawla, A. K.; Chandra, R. Enhancement of Ferromagnetism in Pd Nanoparticle by Swift Heavy Ion Irradiation. *Appl. Phys. Lett.* **2010**, *96* (5), 053103.

(21) Gavade, C.; Singh, N. L.; Avasthi, D. K.; Banerjee, A. Effect of SHI on Dielectric and Magnetic Properties of Metal Oxide/PMMA Nanocomposites. *Nucl. Instrum. Methods Phys. Res. Sect. B Beam Interact. Mater. At.* **2010**, *268* (19), 3127–3131.

(22) Jaffari, G. H.; Ceylan, A.; Ni, C.; Shah, S. I. Enhancement of Surface Spin Disorder in Hollow NiFe 2 O 4 Nanoparticles. *J. Appl. Phys.* **2010**, *107* (1), 013910.

(23) Smigelskas, A. D.; Kirkendall, E. O. Zinc Diffusion in Alpha Brass. *Trans Aime* **1947**, *171* (1947), 130–142.

(24) Heilmann, A.; Müller, A. D.; Werner, J.; Müller, F. Electron Beam Initiated Oxidation and Coalescence of Metal Particles Embedded in a Plasma-Polymer Thin Film Matrix. *Thin Solid Films* **1995**, *270* (1–2), 351–355.

(25) Wang, C. M.; Baer, D. R.; Amonette, J. E.; Engelhard, M. H.; Antony, J. J.; Qiang, Y. Electron Beam-Induced Thickening of the Protective Oxide Layer around Fe Nanoparticles. *Ultramicroscopy* **2007**, *108* (1), 43–51.

(26) Sundararajan, J. A.; Kaur, M.; Qiang, Y. Mechanism of Electron Beam Induced Oxide Layer Thickening on Iron–Iron Oxide Core–Shell Nanoparticles. *J. Phys. Chem. C* **2015**, *119* (15), 8357–8363. https://doi.org/10.1021/acs.jpcc.5b00943.

(27) Wang, C.; Baer, D. R.; Amonette, J. E.; Engelhard, M. H.; Antony, J.; Qiang, Y. Morphology and Electronic Structure of the Oxide Shell on the Surface of Iron Nanoparticles. *J. Am. Chem. Soc.* **2009**, *131* (25), 8824–8832.

(28) Wang, C. M.; Baer, D. R.; Amonette, J. E.; Engelhard, M. H.; Qiang, Y.; Antony, J. Morphology and Oxide Shell Structure of Iron Nanoparticles Grown by Sputter-Gas-Aggregation. *Nanotechnology* **2007**, *18* (25), 255603.

(29) Wang, C. M.; Baer, D. R.; Thomas, L. E.; Amonette, J. E.; Antony, J.; Qiang, Y.; Duscher, G. Void Formation during Early Stages of Passivation: Initial Oxidation of Iron Nanoparticles at Room Temperature. *J. Appl. Phys.* **2005**, *98* (9), 094308.

Chapter 3: Synthesis and Characterization of The Granular Films

3.1. Nanocluster Deposition System

The origin of the cluster source aggregation system dates back to 1990s when Dr. H. Haberland, Dr. You Qiang and other co-workers developed the techniques of combining the magnetron sputtering with gas-aggregation to form a stable cluster beam with a high degree of ionization.[1–4] After this initial finding, the technique has been adopted in many laboratories worldwide. Dr. You Qiang, being one of the contributors for the initial design, later improved the design and established the third-generation nanocluster source-deposition system. The description of the system and cluster preparation techniques can also be found in the published literatures.[5–7]

This third-generation nanocluster source-deposition system has three main chambers: the aggregation chamber, reaction chamber and deposition chamber. Inside the aggregation chamber is the cluster source, or the sputtering gun, which works on the principle of high-pressure magnetron sputtering. On sputtering, the target present in the sputtering gun releases metal atoms, which aggregate together in chilled-water-cooled aggregation chamber, to form the nanoclusters (NCs). The reaction chamber enables NCs to react with the gases. Also, the reaction chamber is connected to the load lock chamber, which helps in loading and unloading the substrates, on which the NCs safely land. The NCs can either be collected in the load lock chamber or the deposition chamber. The advantage of the deposition chamber is that a negative voltage can be applied to the silicon substrate. This voltage accelerates the deposition of the NCs and the charged clusters can be energetically landed on the substrate and deformed to prolate shape, which in turn could exhibit anisotropic behavior.

Five different gases, namely Argon, Helium, Nitrogen, Oxygen and Hydrogen can be supplied into the aggregation and reaction chamber at a time for the benefit of sputtering and reaction with NCs. Argon, Helium, Oxygen and Nitrogen are the most commonly used gases in the cluster

source deposition system. Of these gases, Argon and Helium gases serve the purpose of sputtering and aggregation inside the aggregation chamber. Oxygen and Nitrogen can be supplied either into the aggregation chamber to form the fully oxidized or fully nitride NCs or into the reaction chamber to form the core shell NCs. The system produces high purity NCs with even size distribution, which can be controlled by the argon/helium gas ratio, pressure inside the aggregation chamber, temperature inside aggregation chamber and aggregation distance. The major factor for the preparation of high purity NCs is that all the chambers are maintained at high vacuum (10^{-7} Torr) by three Turbo Molecular Pumps-Mechanical pump systems, which constantly create a vacuum, and the gases utilized for sputtering and reactions have ultra-high purity (99.995%). Every chamber is equipped with two pressure gauges, namely low vacuum pressure gauges and high vacuum pressure gauges, which accurately read the pressure inside the chambers. The gas flow rates into the chambers are controlled by an MKS mass flow controller, which can control the flow from 1 sccm to 1000 sccm for Helium and Argon gases. For the Oxygen and Nitrogen gas flow, an MKS mass flow controller was used to control the flow from 1 to 200 sccm. A schematic representation of the third generation NC deposition system is shown in Figure 2.1.

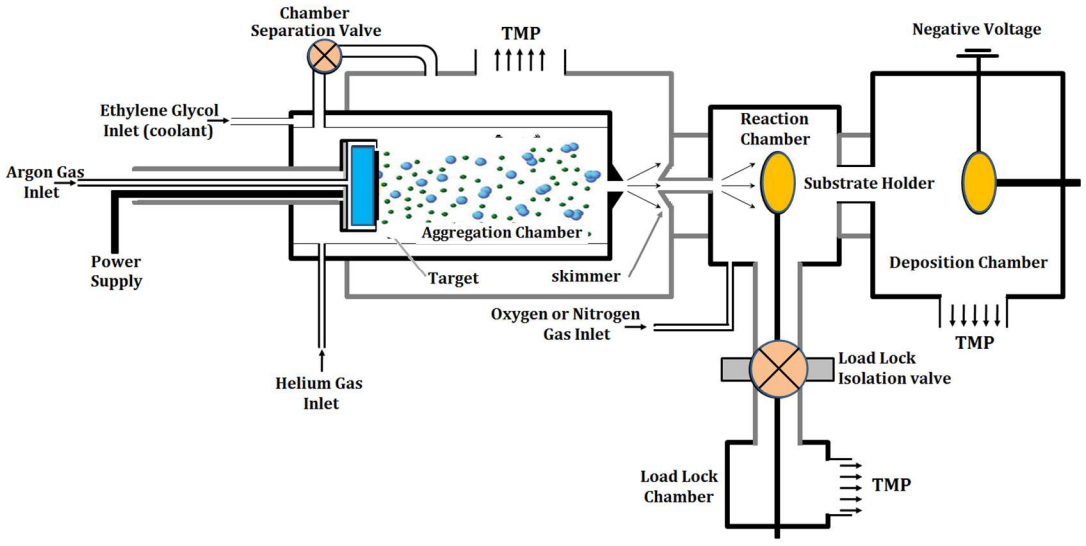

Figure 3.1 Schematic representation of the third-generation nanocluster deposition system.

As shown in the Fig. 3.1, the sputtering gun is located on the inside of the aggregation chamber. Metallic targets of 3 inches in diameter (76.2 cm) and ~0.3 cm thick with high purity of 5N (99.999%) sit on the circular edge of the gun surface under which two concentric magnets of opposite poles are placed in order to help to direct the path of sputtering. The Argon gas is supplied through the gun into the aggregation chamber. The Helium gas is supplied through an opening at the bottom of the aggregation chamber, which embraces the inside surface layer of the aggregation chamber. The system is cooled by chilled water (5 °C) and Ethylene Glycol cooler (-7 °C), which prevents overheating of the gun and chamber during sputtering. Each target has a lifetime of around 4 hrs, with good sputtering rate productivity up to 2 hrs. Also, the aggregation chamber is connected with a big Turbo Molecular Pump, which constantly creates high vacuum. Though the aggregation chamber and the external chamber have a valve connecting them to each other that can be opened to suck the gases from the aggregation chamber, it remains closed during sputtering in order to maintain constant pressure for cluster formation inside aggregation chamber and to create a pressure difference between inside aggregation chamber to the deposition chamber. The pressure difference causes the clusters to travel across the chambers and be deposited in a substrate in the deposition chamber. There is a small opening at the end of the aggregation chamber that can be varied in diameter to increase and decrease the pressure inside the aggregation chamber. Changing the diameter influences on the cluster size. When the pressure is high, it enables more clusters to aggregate, to form bigger size cluster. Also, there is a skimmer located just before the reaction chamber, which helps to filter out the smaller clusters and focuses the larger clusters towards the substrate.

The reaction chamber can either be used for the supplying gas to react with the clusters or can be used to collect the clusters in the substrate. The load lock chamber connected to the reaction chamber can be isolated with a valve, which serves the purpose of loading and unloading the samples. The load lock chamber is also connected with a TMP backed up with a mechanical pump. As mentioned earlier, the deposition chamber and the reaction chamber serve the purpose of collecting

the clusters. There is no difference in the clusters collected in either of the chambers, except for a negative voltage that can be applied to the substrate in the deposition chamber. This negative voltage accelerates the travelling clusters from the aggregation chamber, which gets deposited to the substrate at high energy, thus deforming the cluster shape from spherical shape to elliptical or prolate shape (football shape) and enhancing anisotropic behavior in the deposited clusters. The TMP located at the deposition chamber helps to create vacuum in both the reaction and deposition chambers.

3.2. Working Principle

The cluster source has a DC magnetron sputtering gun with a high purity target sitting on the end to which high power (up to 250 W of DC power) is supplied. When the noble gas Argon is supplied to the aggregation chamber and comes into the vicinity of the electric field generated by the gun, it gets ionized. The ionized Ar gases are attracted to the target by the DC bias while the permanent magnet beneath the target surface creates a magnetic field that guides the ions, by Lorentz force, to hit the target with a huge impact. This impact is capable of ejecting the target atoms from the surface, thus the process called sputtering occurs. The highly energetic Ar^+ impact continues as the new neutral Ar atoms come in and the sputtering process continues to eject huge number of target atoms. As these atoms travel along the aggregation chamber, they aggregate with the influence of pressure, temperature, impact of Helium atoms and the distance travelled in the aggregation chamber. The Helium atoms helps in the formation of mono dispersed (uniform cluster size) NCs, because the energy is transferred from hot metal atoms to the cold Helium gas, which enables the smooth and uniform growth of clusters. Hence, one of the main factors influencing the cluster growth is the Argon to Helium ratio, the factor which has the greatest influence over the cluster size. The higher the ratio, the greater is the cluster size and the smaller is the mono dispersion. The lower the ratio, the smaller is the cluster size and the greater is the size distribution. The other factors influencing the cluster size are the power supplied, the aggregation chamber temperature, aggregation distance and

the pressure maintained inside the aggregation chamber. The working pressure maintained in the aggregation chamber is normally 1 torr and the pressure at the deposition chamber is 10^{-4} torr. This pressure difference causes the clusters to travel the distance into deposition chamber and become deposited onto the substrate, forming a thin granular film. The thickness of granular film is dependent on the deposition time and varies from nano meter to micrometer based on the duration of deposition. The thickness is almost constant throughout the layer.

3.3. Synthesis of Granular Films

The gas-phase clusters to be deposited on a silicon substrate were generated in a magnetron plasma gas aggregation cluster source. The magnetron discharge was operated in a chili water cooled aggregation tube. A stream of pure argon gas was introduced through a ring structure close to the surface of an iron target with 99.9% purity to maintain the discharge. Other stream of Helium was fed as a buffer gas through a gas inlet near the magnetron discharge head. Clusters were formed from the atoms sputtered from the target. During this process, clusters in the discharge-generated plasma acquired high kinetic energies and collided with the neutrals in the gas, causing the formation of very reactive species. The clusters were swept by the gas stream out of the aggregation tube into vacuum through a nozzle. Then they continued to pass through a skimmer into a comparatively high vacuum deposition chamber. To form a core-shell structure, a small amount of oxygen was introduced into the deposition chamber for controlled oxidation of cluster. Before depositing on the substrate, the cluster transfers into core-shell like structure and avoid the further oxidation after exposing to environment. A deposition rate of 1 Å/ s, was obtained with a discharge power of 200 W. The details of sputtering conditions are discussed in further chapters as per the requirement of cluster type, size, and material.

In this research, granular films of Fe based NPs were created on a silicon substrate of size 1cm × 1 cm size silicon substrate with uniform thickness. In this case, the target was mounted on the sputtering gun inside the aggregation chamber as cathode. The Fe atoms are allowed to sputter using

200 W DC power source. To obtain a fully oxidized Fe NP granular films, oxygen gas was introduced into the aggregation chamber to enable instance oxidation of Fe atoms. The oxidized Fe NPs were then aggregated together through low temperature (~ -7 °C to) form fully oxidized iron nanocluster (magnetite) and are deposited on to the silicon substrate. However, to obtain core-shell NP films were created by allowing wither the oxygen gas and/or the nitrogen gas to react with Fe nanoclusters in the reaction chamber.

3.4. Synthesis of Ellipsoidal Granular Films

The nanocomposite Fe/Fe_3O_4 cluster films were synthesized at room temperature, by obliquely impacting the energetic Fe/Fe_3O_4 nanoclusters onto the (110) Si substrates, using a combination of magnetron sputtering and gas-aggregation techniques as explained in the above section. The monodispersed Fe nanoclusters firstly congregated in an aggregation chamber from the Fe atoms, which were sputtered from a 3-inch Fe target with a power of 200 W and collided with a flow of Ar and He gas atoms. Meanwhile, the aggregation chamber was cooled down to -7 ^oC by the chilled water. With residing in the plasma with a high density of ions and electrons, ∼30% and ∼40% of the Fe nanoclusters were positively and negatively charged, respectively. Then the Fe nanocluster ions were driven by the differential pumping to pass through a reaction chamber, where a flow of 10 sccm O_2 was introduced to oxidize the surface layer of the nanoclusters. Finally, the negatively ionized Fe/Fe_3O_4 core-shell nanoclusteres were accelerated by an electric field to impinge onto the tilted Si substrate, to which potentials from 0 to 10 kV were applied. The substrate was held approximately 30^o with respect to the incident clusters beam. The positive bias voltage was selected to prevent the implantation of rare gas ions into the nanocomposites and repel the positively charged nanoclusters, with the neutral ones softly landing on the substrate holder. Before the nanocomposites deposition, all the chambers were evacuated to background pressures better than 1×10^{-7} Torr.

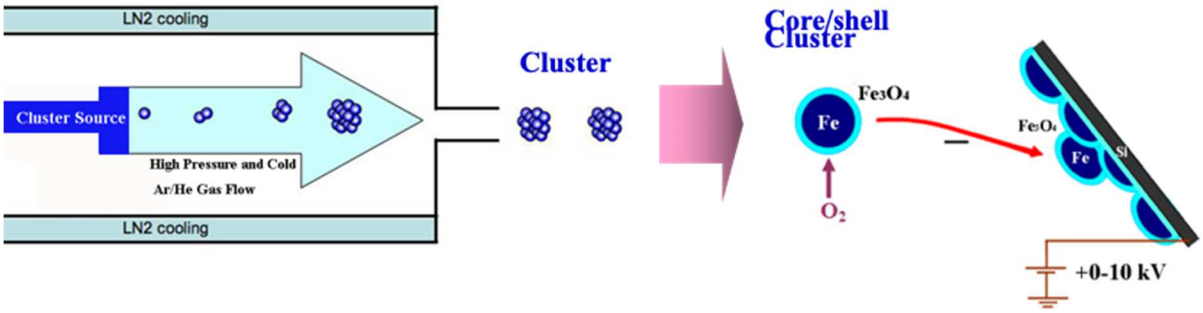

Figure 3.2 Schematic of synthesis of ellipsoidal nanocomposite

3.5. Heat-Treatment of Granular Films

The granular films synthesized on the silicon substrates by using nanocluster deposition system were then heat treated at different temperature using tube furnace (Figure 4.2). The granular films were heat-treated in different environments based on the requirement of this project and the detail of the heat-treatment conditions like temperature, environments and rate of the heating are discussed in respective chapters.

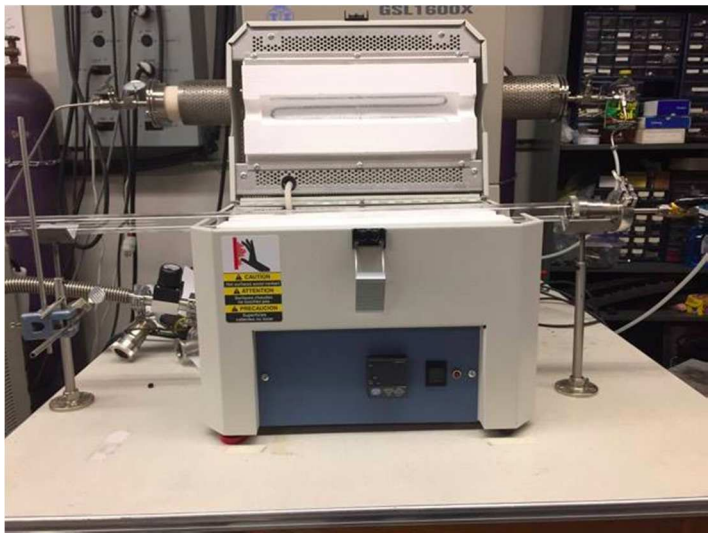

Figure 3.3 Photograph of the tube furnace used for the heat-treatment of granular films

3.6. Characterization of Granular Films

Characterizations were conducted on the granular films pre- and post-heat treatment in order to understand the temperature-induced structural evolution mechanism, morphology, phase, shape and size, and structure-property relationships. The characterizations mainly focused on magnetic properties, surface property, structural analysis, elemental analysis and cluster size features. Some of the tools used for the characterization purposes are X-ray Diffraction (XRD), which provides the information regarding phase and average crystallite size of the films, Vibrating Sample Magnetometer (VSM) to measure the magnetic properties, and Energy Dispersive X-ray Spectroscopy (EDS), which provides the elemental information of the granular films. These characterization techniques are discussed in detail in the following sections.

3.6.1. X-Ray Diffraction (XRD)

X-ray diffraction techniques (XRD) utilized the dual wave/particle nature of X-rays to understand information about the phase and structure of crystalline materials. A primary use of the techniques is the identification and characterization of compounds based on their diffraction pattern. The dominant effect that occurs when an incident beam of monochromatic x-rays interacts with a target material is scattering of those X-rays from atoms within the target material. The scattering is elastic scattering of x-rays from the electron clouds of the individual atoms in the system. In a crystalline material, the scattered X-rays undergo constructive and destructive interreference. This is the process of diffraction. The diffraction of X-rays by crystal is described by Bragg's law, $2d_{hkl}sin\theta = n\lambda$, where d_{hkl} is the interplanar spacing of the (hkl) planes, θ is the angle of incidence, n is an integer, and λ is the wavelength of the incident X-ray in our experiments. The directions of possible diffractions depend on the kind and arrangement of atoms in the crystal structure. The measurements are based on observing the scattered intensity of an X-ray beam hitting a sample as function of incident and scattered angle, polarization and wavelength or energy (Figure 4.1). The

XRD measurement yields the atomic structure of materials and it is a non-destructive analytical technique, which reveals information about the crystallographic structure, chemical composition, and physical properties of materials and thin films.[8–10] In this research, the XRD measurement were carried out using Siemens D5000 Powder X-ray Diffractometer with Solex solid-state detection system and CuKα line (1.54 Å). The symmetric scan ranged from 2θ = 5° - 90° with a step size of 0.05° and a dwell time of 5s at each step was employed to study the crystallographic phase.

X-ray peak broadening also provides a quick estimate of the average crystallite size in polycrystalline materials and powders. The cluster size D can be deduced from the XRD line broadening according to the Scherrer formula:

$$D = \frac{0.9\lambda}{B\ cos\theta} \tag{4.1}$$

where B is line broading or the full width half magnitude (FWHM) in radian, θ is the XRD peak position.

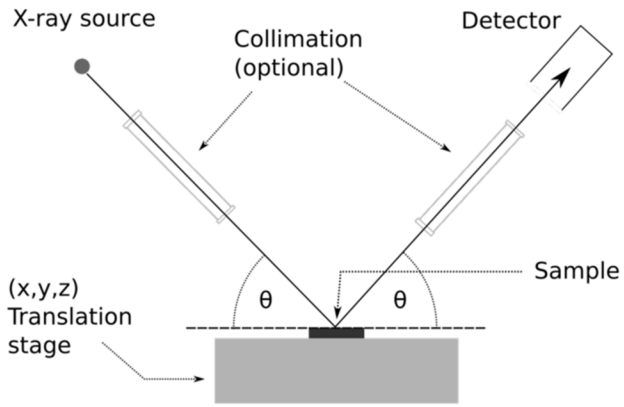

Figure 3.4 Schematic of X-ray Diffractometer

3.6.2. Scanning Electron Microscope

A scanning electron microscope (SEM) is a type of electron microscope that produces images of a sample by scanning it with a focused beam of electrons. The electrons interact with atoms in the

sample, producing various signals that can be detected and that contain information about the sample's surface topography and composition. The electron beam is generally scanned in a raster-scan pattern, and the beam's position is combined with the detected signal to produce an image. SEM can achieve resolution better than 1 nanometer. Specimens can be observed in high vacuum, in low vacuum, in wet conditions (in environmental SEM), and at a wide range of cryogenic or elevated temperatures. The schematic of SEM is shown in Figure 4.4. The most common mode of detection is by secondary electrons emitted by atoms excited by the electron beam. On a flat surface, the plume of secondary electrons is mostly contained by the sample, but on a tilted surface, the plume is partially exposed, and more electrons are emitted. By scanning the sample and detecting the secondary electrons, an image displaying the topography of the surface is created.

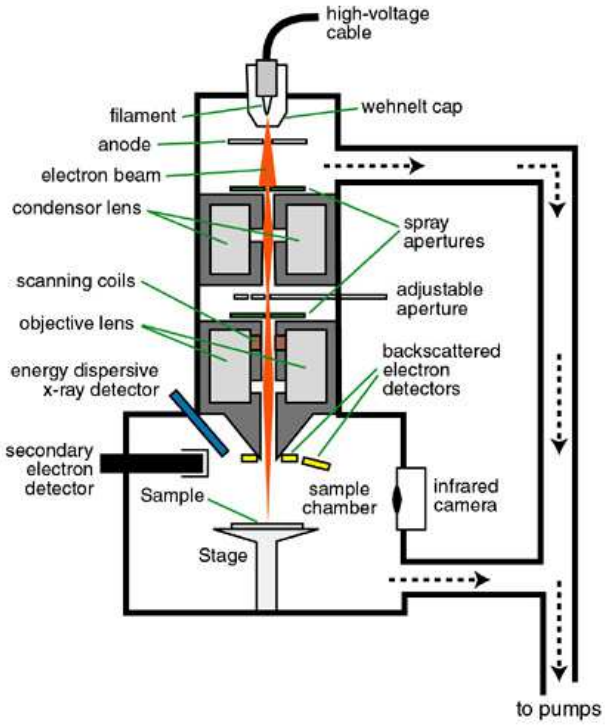

Figure 3.5 Schematic of Scanning Electron Microscope

3.6.3. Transmission Electron Microscope

Transmission electron microscope (TEM) is analogous to an optical microscopy: the photons are replaced by high energy electrons and the glass lenses by electromagnetic lenses as shown in Figure 4.6. In TEM microscopy technique an electron beam is transmitted through an ultra-thin electron-transparent sample, interacting with the sample and forming an image detected by a sensor such as a CCD camera and an enlarged image is formed using a set of magnetic lenses. The highly energetic incident electrons interact with the atoms in the sample producing characteristic radiation and particles providing information for materials characterization. Information is obtained from both deflected and non-deflected transmitted electrons. Backscattered and secondary electrons, and emitted photons. According to Rayleigh's criterion, the resolution W of the optical system is given by the following equation: $W = 0.6\lambda/NA$, where NA is the numerical aperture and λ is the wavelength. Therefore, the much smaller wavelength of electrons allows a resolution of about 0.2 nm to be achieved. The particle shape, size distribution, faceting and crystallinity can be obtained using TEM. Here, electron microscopy experiments were conducted on a JEOL 1200 TEM, operating at 120 kV. The samples were prepared by drying the solvent of the MNPs' dispersion onto a 200 mesh copper grid with a carbon coated Formvar film.

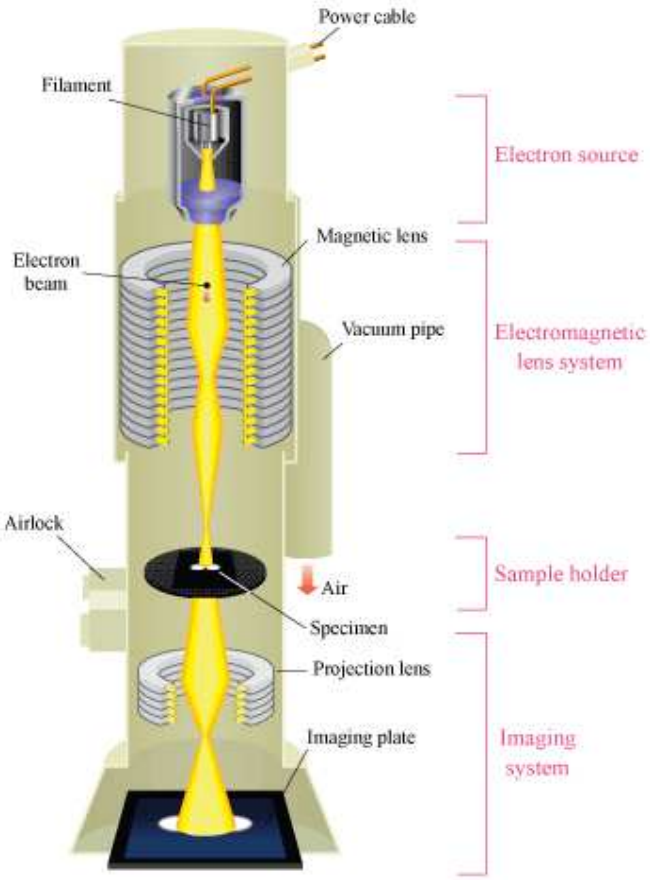

Figure 3.6 Schematic of Transmission Electron Microscope

3.6.4. Energy Dispersive X-Ray Spectroscopy

Energy-Dispersive X-ray Spectroscopy (EDX or EDS) is also called energy dispersive X-ray analysis (EDXA). EDX is a standard procedure for identifying and quantifying elemental composition of specimen areas as small as a few cubic micrometers. The characteristic X-rays are produced when a material is bombarded with electrons in an electron beam instrument, such as transmission electron microscopy (TEM) or scanning electron microscope (TEM). A brief description of the generation of characteristic X-rays is as follows. First the incoming electrons from TEM or SEM knock inner shell electrons out of atoms in the sample. In order to return the atom to its normal state, an electron from an outer atomic shell drops into the vacancy in the inner shell. This drop results in the loss of a

specific amount of energy, namely, the difference in energy between the vacant shell and the shell contributing the electron. The energy is given up in the form of electromagnetic radiation x-rays. Since energy levels in all elements are different, element-specific or characteristic, x-rays are generated. The emitted x-rays are indicative of the element that produced them. The EDX x-ray detector measures the number of emitted x-rays versus their energy. The energy of the x-ray is characteristic of the element from which the x-ray was emitted. A spectrum of the energy versus relative counts of the detected x-rays is obtained and evaluated for qualitative and quantitative determinations of the elements present in the sampled volume.

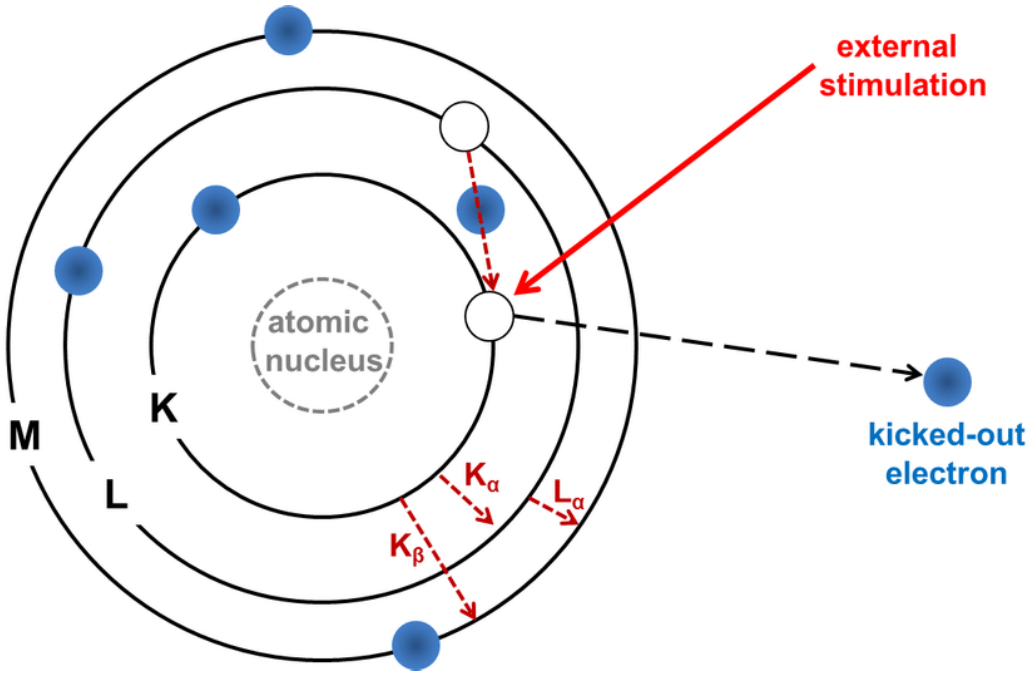

Figure 3.7 Schematic showing the principle of EDX

3.6.5. Vibrating Sample Magnetometer (VSM)

Magentic properties were characterized using a DMS 1660 VSM where each pre-weighted sample is placed inside an external magnetic field to get magnetized at room temperature. A hysteresis loop was acquired by applying a scanning magnetic field of 13500 Oe to -13500 Oe. The

vibrating sample magnetometer (VSM) was developed in 1956 by S Foner and Van Oosterhart. In a VSM a sample is vibrated in the vicinity of a set of pick-up coils. According to Faraday's laws of magnetic induction, the flux change caused by the moving magnetic sample causes an induction voltage across the terminals of the pickup coils which is proportional to the magnetization of the sample V(t) = Cd(fi)/dt, where fi(t) represents the changing flux in the pick-up coils caused by the moving magnetic sample. With the calibration, this voltage is proportional to the magnetic moment of the sample. A brief description of VSM is given as follows. The pick-up coils are situated between the pole pieces around the sample (Figure 4.8). Both the signals produced by the permanent magnet vibrating in the pick-up coils and the signal induced in the sample pick-up coils are fed directly into a lock-in amplifier. The permanent magnet signal is used as the reference signal input. The system is calibrated using a single crystal nickel disc whose saturation magnetization is well documented.

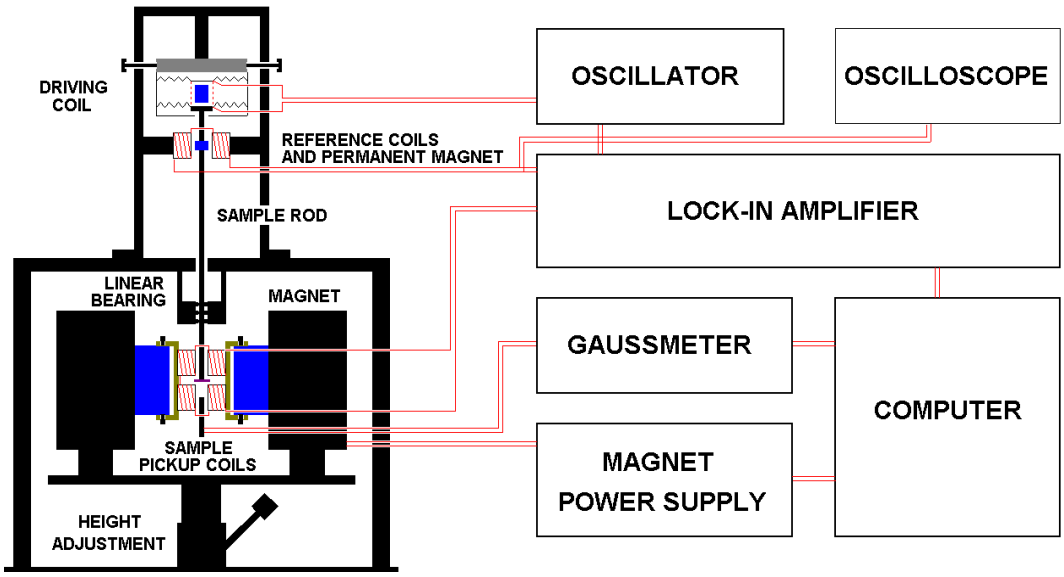

Figure 3.8 Schematic of Vibrating Sample Magnetometer

If a material is placed within a uniform magnetic field, a magnetic moment will be induced in the sample. In a VSM, a sample is positioned within suitable placed sample, coils, and is made to undergo sinusoidal motion, i.e., mechanically vibrated. The resulting magnetic flux changes induce a

voltage in the sample coils that is proportional to the magnetic moment of the sample. The applied filed may be produced by an electromagnet or superconducting coils.

3.6.6. Atomic Force Microscopy

An atomic force microscopy (AFM) is a type of scanning probe microscopy that forms image of surfaces using a physical probe that scans the specimen. The AFM uses a cantilever with a very sharp tip to scan over a sample surface. As the tip approaches the surface, the close range, attractive for**ce** between the surface and the tip cause the cantilever to deflect towards the surface. However, as the cantilever is brought even closer to the surface, such that the tip makes contact with it, increasingly repulsive force takes over and causes the cantilever to deflect away from the surface.

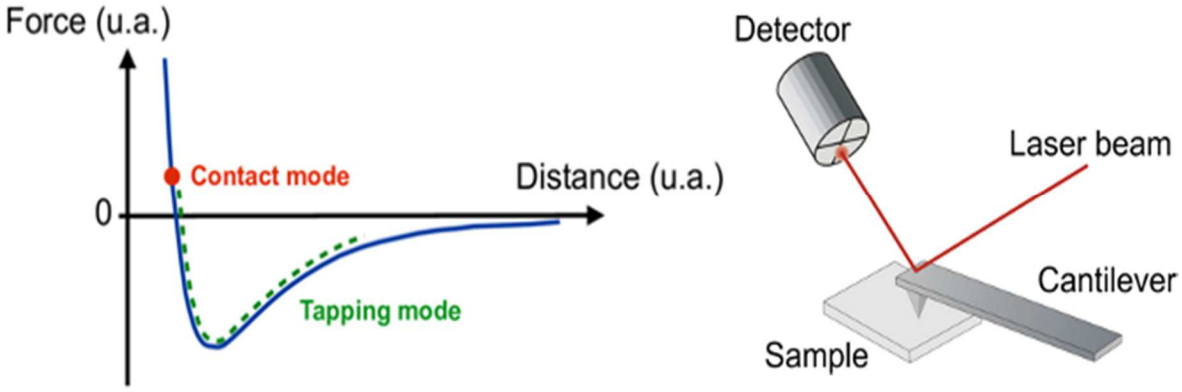

Figure 3.9. (Left) Force-distance curve for AFM, and (Right) block diagram of AFM showing beam deflection and detection.

A laser beam is used to detect cantilever deflection towards or away from the surface. By reflecting an incident beam off the flat top of the cantilever, any cantilever deflect will cause slight change in the direction of the reflected beam (see Figure 3). A position sensitive photodiode (PSPD) can be used to track these changes. Thus, if an AFM tips passes over a raised surface feature, the resulting cantilever deflection (and the subsequent change in the direction of reflected beam) is recorded by the PSPD.

3.7. References

(1) Haberland, H.; Moseler, M.; Qiang, Y.; Rattunde, O.; Reiners, T.; Thurner, Y. Energetic Cluster Impact (ECI): A New Method for Thin-Film Formation. *Surf. Rev. Lett.* **1996**, *3* (01), 887–890.

(2) Haberland, H.; Mall, M.; Moseler, M.; Qiang, Y.; Reiners, T.; Thurner, Y. Filling of Micron□sized Contact Holes with Copper by Energetic Cluster Impact. *J. Vac. Sci. Technol. A* **1994**, *12* (5), 2925–2930. https://doi.org/10.1116/1.578967.

(3) Haberland, H.; Karrais, M.; Mall, M.; Thurner, Y. Thin Films from Energetic Cluster Impact: A Feasibility Study. *J. Vac. Sci. Technol. Vac. Surf. Films* **1992**, *10* (5), 3266–3271.

(4) De Heer, W. A. The Physics of Simple Metal Clusters: Experimental Aspects and Simple Models. *Rev. Mod. Phys.* **1993**, *65* (3), 611.

(5) Qiang, Y.; Thurner, Y.; Reiners, T.; Rattunde, O.; Haberland, H. Hard Coatings (TiN, TixAl1- XN) Deposited at Room Temperature by Energetic Cluster Impact. *Surf. Coat. Technol.* **1998**, *100*, 27–32.

(6) Qiang, Y.; Antony, J.; Sharma, A.; Nutting, J.; Sikes, D.; Meyer, D. Iron/Iron Oxide Core-Shell Nanoclusters for Biomedical Applications. *J. Nanoparticle Res.* **2006**, *8* (3–4), 489–496.

(7) Antony, J.; Nutting, J.; Baer, D. R.; Meyer, D.; Sharma, A.; Qiang, Y. Size-Dependent Specific Surface Area of Nanoporous Film Assembled by Core-Shell Iron Nanoclusters. *J. Nanomater.* **2006**, *2006*.

(8) Rao, C. N. R.; Biswas, K. Characterization of Nanomaterials by Physical Methods. *Annu. Rev. Anal. Chem.* **2009**, *2*, 435–462.

(9) Kalantar-zadeh, K.; Fry, B. *Nanotechnology-Enabled Sensors*; Springer US, 2008. https://doi.org/10.1007/978-0-387-68023-1.

(10) Nanomaterials. *Wikipedia*; 2020. https://en.wikipedia.org/wiki/Nanomaterials

Chapter 4: High-Temperature Investigation on Morphology, Phase and Size of Iron/Iron-Oxide Core-Shell Nanoclusters for Radiation Nanodetector

Khanal, L. R.; Williams, T.; Qiang, Y. High-Temperature Investigation on Morphology, Phase and Size of Iron/Iron-Oxide Core–Shell Nanoclusters for Radiation Nanodetector. *J. Phys. D: Appl. Phys.* **2018**, *51* (25), 255302. https://doi.org/10.1088/1361-6463/aac47e.

4.1. Abstract:

Iron/iron-oxide (Fe-Fe_3O_4) core-shell nanoclusters (NCs) synthesized by cluster deposition technique were subjected to study the high temperature structural and morphological behavior. Annealing effects have been investigated up to 800 °C in vacuum, oxygen and argon environments. The ~18 nm average size of the as prepared NCs increases slowly on temperature up to 500 °C in all the three environments. The size increases abruptly in argon environment but slow in vacuum and oxygen when annealed at 800 °C. The x-ray diffraction (XRD) studies have shown that the iron core remains in the core-shell NCs only when they were annealed in the vacuum. A dramatic change in the surface morphology, an island like structure and/or a network like pattern, was observed at the elevated temperature. The as prepared and annealed samples were analyzed using XRD, scanning electron microscopy and imageJ software for a close inspection of the temperature aroused properties. This work presents the temperature induced size growth mechanism, oxidation kinetics and phase transformation of the NCs accompanied by cluster aggregation, particle coalescence, and diffusion.

4.2. Introduction

In the recent years, numerous studies have been conducted to investigate the nanoparticle (nanoclusters called in this paper) behaviors, such as magnetic, electrical, mechanical, structural properties for obtaining novel functional nanomaterials. Nanostructured materials have shown improved properties over bulk materials, allowing them to be used extensively in the various field.[1–4] Magnetic nanoparticles have already been discovered for their applications in biomedicine, magnetic

resonant imaging, data storage, magnetic separation, waste water treatment, nuclear waste treatment.[5–11] Recently, nuclear scientists have drawn their interests to apply the magnetic nanoparticles for nuclear radiation sensing and monitoring systems to be used in the high-temperature core of the upcoming generation IV nuclear reactor for enhanced performance and safety. It was previously reported that the iron/iron-oxide (Fe-Fe_3O_4) core-shell nanoclusters (NCs) with Fe_3O_4 as shell and Fe as core have very sensitive changes of electrical conductivity under ion irradiation even at extremely low dose ion flux regime with the minimal effect of the temperature up to 200 °C.[12] Figure 4.1 illustrates the normalized in-situ electrical resistance measurement of the NCs with the Si^{2+} ion fluence at room temperature and 200 °C measured by Van der-Pauw four-probe method. Since the commercial detectors available in the market have poor sensitivity at low dose fluxes and also cannot retain their properties at high temperature even at the working flux regime, this opens the new area of research for the Fe based nanoclusters to serve as a radiation nanodetector. However, it requires further investigation on the properties of the NCs at high temperature and under neutron irradiation as well since the core of the reactor has two parameters that may affect the magnetic and electrical properties of the NCs: heat (up to 500 °C) and radiation.

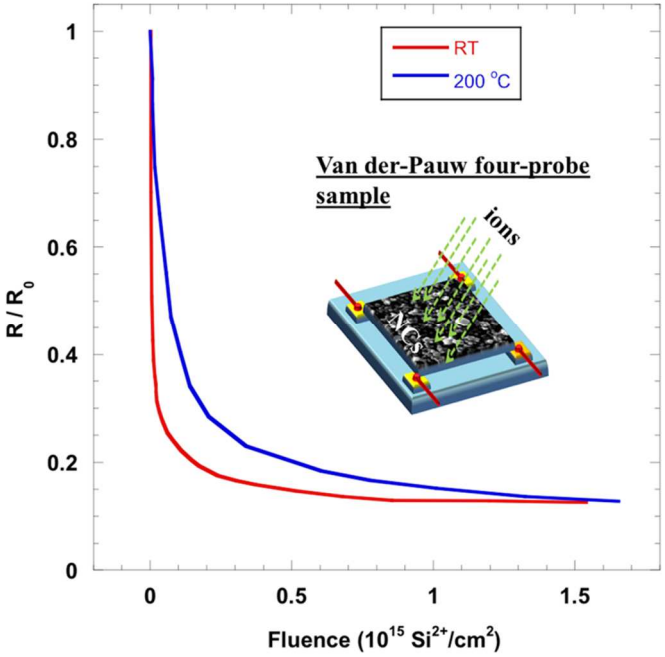

Figure 4.1. In-situ electrical resistance (normalized) of a Fe-Fe_3O_4 NCs under Si^{2+} ion irradiation at room temperature (RT) and 200 °C by Van der-Pauw four-probe methods[12]

Recently, there have been several reports on the magnetic, electrical conductivity, and structural study of Fe-Fe_3O_4 core-shell NCs in relation to the size of the particles and/or ion irradiation[12–16] but there are lack of knowledge on the high-temperature effects. Our previous report has shown that the change in electrical conductivity of the NCs is the result of change in the microstructure and grain size under ion irradiation.[12] Thus, for the intended application, mechanism of the change in surface morphology, nanostructure evolution, and size distribution of the NCs at high-temperature should be understood.

In this study, we present the high temperature annealing effects on the size, surface morphology and phase of the NCs. The Fe NCs for the investigation were prepared by nanocluster deposition system that combines magnetron sputtering with gas condensation technique. An oxide shell of Fe_3O_4 was obtained by controlled oxidation before collecting on the surface of Si-substrates. The NCs were then annealed at different temperature up to 800 °C in three different environments:

oxygen (O_2), argon (Ar), and vacuum (Vac.). Surface morphology, nanostructure, phase transformation and size distribution of the NCs are reported along with the close examination of the relationship between the size growth mechanism and nanostructural evolution of the NCs at the elevated temperature.

4.3. Experimental Details

The Fe-Fe_3O_4 core-shell NCs for this study were prepared by the state-of-the-art cluster deposition system. The detail description of the fabrication of the NCs by this method is described in previous papers[11,13] and briefly summarized here as well. Fe nanoclusters were obtained from a Fe-target as cathode mounted on a sputtering gun inside the aggregation chamber. The DC power (200 W) applied to the gun allowed the Ar gas in the aggregation chamber to be ionized. The energetic Ar^+ ions knocked out the Fe-atoms from the target. The Fe-atoms were then slowed down due to three-body collisions between Fe, Argon (Ar) and Helium (He) in the aggregation chamber. Due to a low temperature (-7 °C) maintained in the aggregation chamber, the Fe-atoms aggregated together, and the pure Fe NCs were formed. The pressure difference allows the NCs to travel towards the reaction chamber where the zero-valent iron (Fe^0) reacts with a small amount of oxygen (~3 sccm) at room temperature. The oxygen oxidized the outer layer of the iron clusters and a core-shell like structure with Fe as a core and iron oxide (Fe_3O_4) as a shell is formed. The evidences of core-shell structure of the obtained NCs were presented in our previous works via electron energy loss spectroscopy (EELS) mapping and transmission electron microscopy images (TEM).[13,15,17] It was also reported that the thickness of the oxide layer formed on the surface of the Fe NC ranges from 2 to 3 nm.[13] The core-shell Fe-Fe_3O_4 NCs were then gently deposited with thermal energy on the surfaces of 10 mm × 10 mm Si-substrates in the deposition chamber in the form of NC granular films with a thickness about 1 μm as shown in the Fig. 2 (a2). The as-prepared granular films on the Si substrates were then annealed in a Lindberg mini furnace at 100 °C, 300 °C, 500 °C, and 800 °C in Vac., Ar, and O_2. The NCs

heated up at the rate of 25 °C/min, remain 1 hour at maximum temperature, and then allowed to cool down to room temperature naturally. The cooling time period however was slower in Vac. (~ by 1 hour more) than in the gaseous medium to cool down themselves from 800 °C. The purpose of selection of vacuum is to simulate the temperature environment in the core of the nuclear reactor, O_2 is to study behavior in air or in an open environment, and inert Ar gas is for the possible protective environment for the NCs at high temperature. The phase transformation and crystal structure, surface morphology and size distribution of the NC films were studied pre- and post-annealing by using Siemens D5000 Powder X-ray Diffractometer with Solex solid-state detection system and CuKα line (1.54 Å), JEOL JSM scanning electron microscope (SEM) and JEOL JEM 2010 TEM, and ImageJ software, respectively.

4.4. Result and Discussions

The SEM images are shown in Figure 4.2. (a1) and (a2) are the top and cross-sectional views of the as prepared NC films at room temperature. The SEM images (b, c and d) are for the annealed NCs in Vac., Ar, and O_2, respectively. The numbers 1-4 in b, c, &d represent the annealing temperatures 100 °C, 300 °C, 500 °C, and 800 °C, respectively. No significant change in surface morphologies has been observed when the NCs were annealed at 100 °C and 300 °C in all the three environments as depicted in Figures 2b-d with numbers 1 & 2. When the NCs were annealed at 500 °C, a small change in morphology has been observed in all three environments. The nanostructures of the loosely aggregated as prepared NCs have been found to change significantly with the concurrent formation of a network like structure accompanied by nano-pores when annealed at 800 °C in O_2 as shown in Figure 4.2 (d4). When the NC was annealed in Ar at 800 °C, a continuous film like morphology along with the nano-pores of average size ~200 nm has been found as depicted in Figure 4.2 (c4). The NCs when annealed at 800 °C in Vac., the particles aggregated together, and island-like structures have been observed as shown in Figure 4.2 (b4).

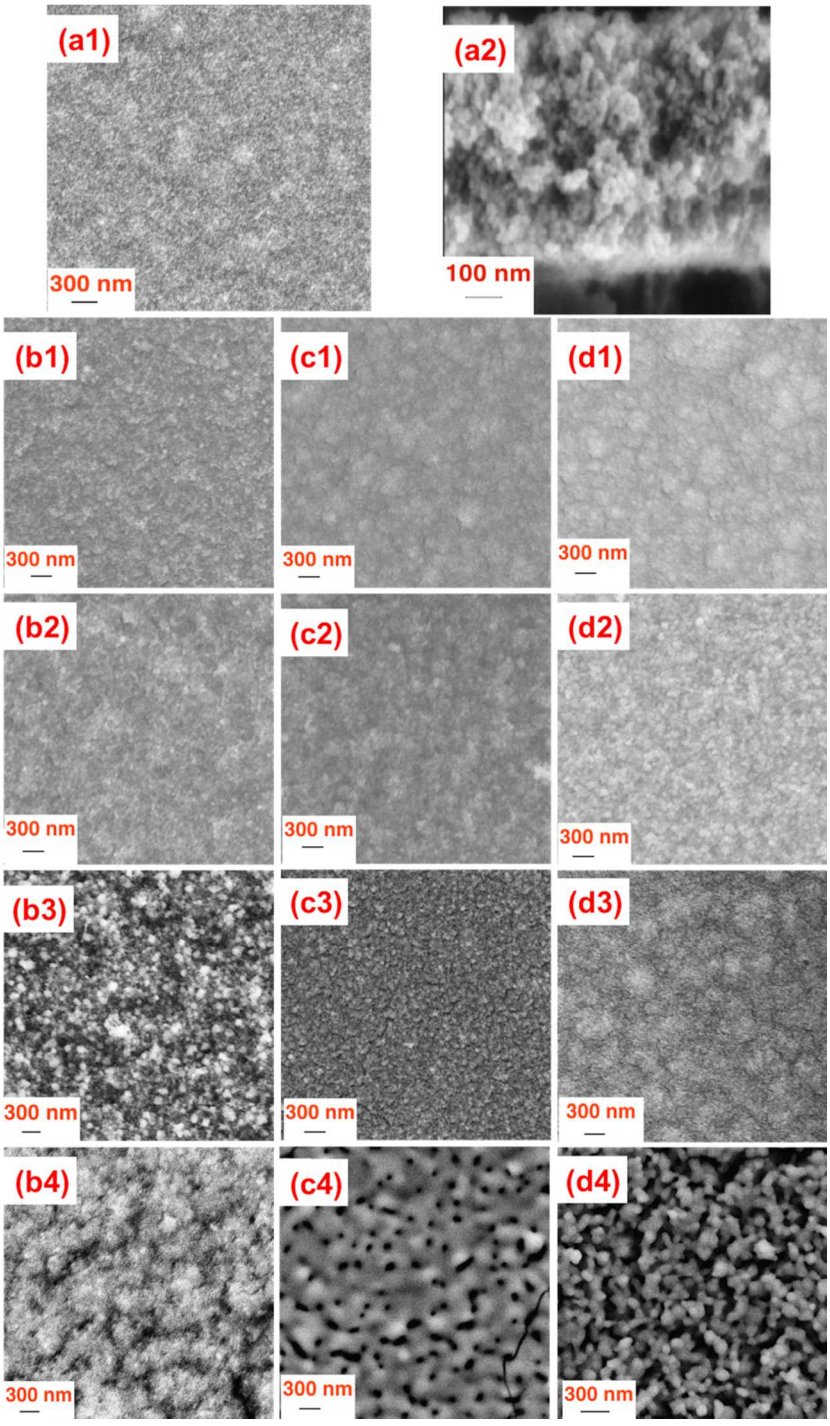

Figure 4.2 SEM images of the NCs before annealing (a1-top view & a2-cross sectional view) and after annealing (b-Vac., c- Ar & d-O_2 environments). The points 1-4 in b, c, d represent the annealing temperatures 100 °C, 300°C, 500 °C and 800 °C respectively.

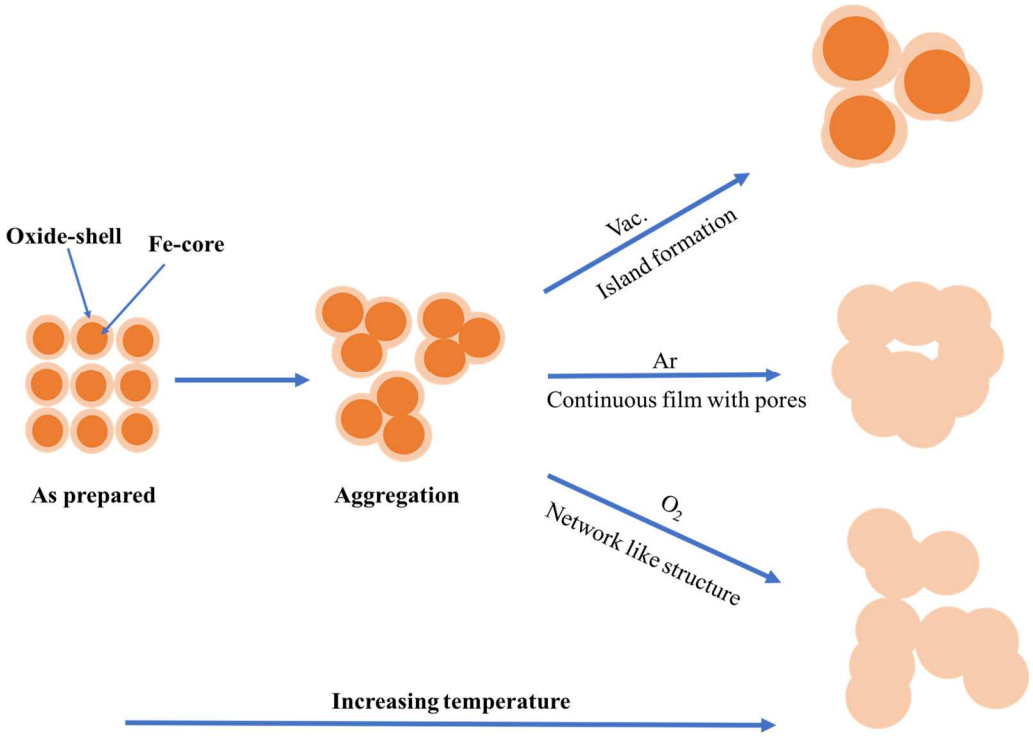

Figure 4.3 Schematic illustration of the particle coalescence and size growth mechanism in three different environments with increasing the temperature.

The mechanism of the island-like structure formation and dramatic change in the morphology at 800 °C accompanied by a network like structures is the result of the agglomeration and the coalescence of the particles at high-temperature. The schematic representation of the process is shown in Figure 4.3. It is plausible that the increasing temperature promotes particles aggregation, which leads to form the island-like structures. With the increasing temperature and/or annealing time the particles get high energy, which allows the particles to come closer to each other and merge together to give rise to a larger particle. The smaller particles with a larger surface to volume ratio are more likely to dissolve into larger particles on increasing temperature, which results the larger one getting bigger and smaller one getting smaller and eventually disappears. The larger particles get interconnected to each other resulting in a nanowire-like network accompanied by nano-pores as

depicted in Figure 4.2 (d4). Continuous film along with the nano-sized pores has also been observed in Ar because of the coalescence of the particles in the proximities leaving the larger space behind. The SEM images (b4), (c4) and (d4) in Figure 4.2 provide evidences for the dramatic change in morphology in the gaseous environments than in the vacuum. The convective transfer of heat to the NCs by heavy gas molecules (Ar) at the elevated temperature could have played a key role in the significant change in the morphology of the granular films.

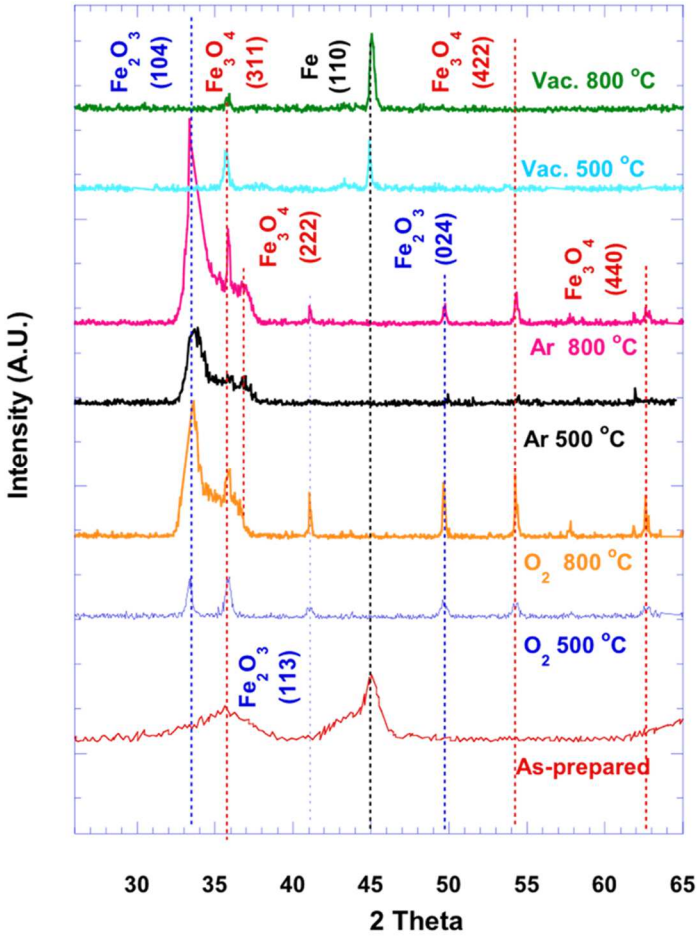

Figure 4.4 X-ray diffraction results for the NCs before and after annealing at different conditions.

Figure 4.4 shows the XRD results of the NCs pre- and post-annealing in Vac., Ar, and O_2 environments at 500 °C and 800 °C while the XRD results for the temperature below 300 ^{0}C are very similar like that of as deposited samples. The XRD pattern shows the Fe in the core of the NCs

disappear completely when they are annealed at 500 °C and 800 °C in Ar and O_2 environment. However, the NCs retain the Fe core even when they are annealed at 800 °C in the vacuum and no phase transformation in the NCs was observed. An evidence of mix phase of Fe_2O_3 and Fe_3O_4 has been observed on annealing the NCs in Ar and O_2. Rioult et al[18] also presented mix phase of pure α-Fe_2O_3 corundum structure and Fe_3O_4 spinel structure on annealing pure spinel structure of Fe_3O_4. The presence of Fe_2O_3 and the loss of Fe-core in Fe-Fe_3O_4 core-shell NCs up on annealing in oxygen environment is the result of diffusion of Fe and O_2 through the oxide layer and oxidation of the Fe atoms.

The temperature-induced motion of an atom in a lattice can be understood by a microscopic description of the diffusion and can be expressed as[19]

$$D = (\frac{1}{6})\lambda^2\Gamma \tag{4.1}$$

Where $\lambda = aA$ is the jump distance (with A, diffusion mechanism constant and $a = 0.839$ for Fe_3O_4[20], lattice constant) and $\Gamma = zp_v\omega$ is the jump frequency with z, the number of nearest neighbor sites (twelve for fcc), p_v, the probability that a given neighboring site is vacant (1/12 for fcc) and ω, the frequency with which an atom jumps to a particular site. The jump frequency $\omega = \nu e^{-\Delta G_m/KT}$ with ν, Debye frequency (~10^{13} s^{-1}), G_m, Gibbs free energy, K, Boltzmann constant (8.617×10^{-5} eV/K), and T in kelvin. We know that the jumps of defects and atoms are due to the thermal vibration of very high frequency. The frequency of atom jumps is the order of magnitude ~10^8 s^{-1} at 700 °C i.e. once in every 10^5 vibrations, a thermal fluctuation is large enough for an atom to overcome the energy barrier separating it from the next stable position.[19] Hence, at 800 °C the Fe and O atoms get sufficient thermal energy to vibrate at their lattice sites and overcome the barrier to diffuse. Metal oxide being an ionic compound, the diffusion involves the transport of both the ions and the electrons.[21] The transport mechanism of metal and oxygen ions along with the electrons and holes is illustrated in the Figure 5a. The Fe ions diffuse toward the surface through the oxide layer as illustrated by schematic in Figure 5b.

The diffusion and oxidation phenomena of the Fe is based on the Cabrera-Mott model [22–24], which suggests that the phenomena is supported by the tunneling of the electron from the metal to the surface through the oxide layer and ionization of the absorbed surface oxygen inducing an electric field. The electric field promotes the outward transport of metal ions. The Fe ions reaching to the surface get oxidized thus giving rise to outward growth of oxide layer when annealed in O_2. The oxygen interstitial formed by the diffusion of the O_2 ion from the surface through the oxide layer diffuse further into the core, allowing the formation of iron oxides at the core-shell interface. The interstitial jump distance, $\lambda = aA$ (with A= 1/2 for interstitial)[19] of Fe/O can be estimated as 0.42 Å, which provides the credibility of the diffusion of the interstitials atoms through the oxide layer. The position of oxidation to take place (at the oxide layer and/or surface) depends up on the mobility of the ions. The larger value of mobility of Fe ions results the oxidation at the oxide-gas interface and the larger mobility of oxygen ions results the oxidation at the metal-oxide interface.

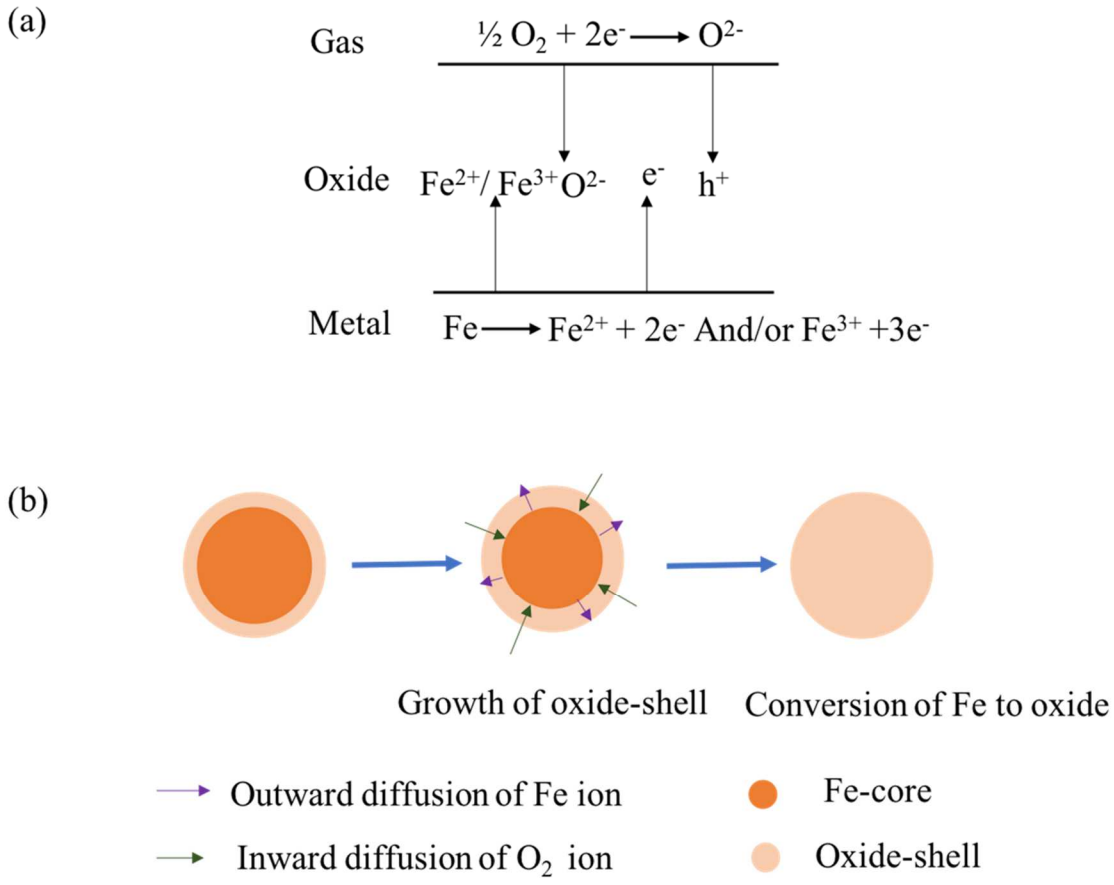

Figure 4.5 Schematic representation of (a) transport mechanism of ions and electrons through oxide layer and (b) evolution of complete oxidation of Fe in O_2 environment.

The retaining of the core-shell structure of the NCs even after annealing at high temperature in Vac. as has shown by XRD reveals an interesting point and advantage for nuclear radiation sensor. The presence of Fe even after annealing the NCs at high-temperature in vacuum is due to the reduction of the Fe_3O_4 to Fe at elevated temperature, under the lack of oxygen (~10^{-3} Torr). The reduced iron diffuses into the core and increases the Fe content in the particle. Lee et al.[25] reported the reduction of metal oxide to metal is possible during vacuum annealing with an evidence of reduction of copper-oxide to copper. In order to understand the reduction, the ratio of phase composition of Fe to Fe_3O_4 in

the as-prepared and Vac. annealed NCs are estimated from the intensities of Fe (110) and Fe_3O_4 (311) XRD peaks by using the following formula.[26,27]

$$\frac{C_\alpha}{C_\beta} = \frac{I_\alpha}{I_\beta} \quad (4.2)$$

Where C_α and C_β represent the compositions of Fe and Fe_3O_4 in the samples and I_α and I_β are the peak intensities of Fe and Fe_3O_4, respectively. The estimated ratio of the compositions of Fe and Fe_3O_4 is summarized in Table 4.1.

Table 4.1 Ratio of Fe to Fe_3O_4 composition at different conditions.

Sample	As-prepared	Vac. 500 °C	Vac. 800 °C
Ratio	1.98	1.56	6.46

The ratio of Fe to Fe_3O_4 phases in the as-prepared samples has been found to increase from 1.98 to 6.46. This indicates that the reduction of the Fe_3O_4 to Fe is plausible. The reduction is attributed by the oxygen vacancy formation at high-temperature annealing. The decrease in ratio at 500 °C than as-prepared NC suggests that the rate of growth of the oxide crystallites by coalescence of the NCs is more likely than the reduction of Fe_3O_4 to Fe. The increase in the ratio from 500 °C to 800 °C indicates that the reduction from metal oxide to metals is enhanced beyond 500 °C. The slower cooling rate and the absence of convective thermal transfer could also have played a role to some extent to protect the core-shell structure during vacuum annealing.

Gossman et al.[28] reported that the 99.95% pure Ar represents a high oxygen partial pressure of the order of 0.1 Torr. Thus, on annealing in Ar, the oxygen content is sufficient for the oxygen sensitive iron to get oxidized by transport of the ions as in O_2 impurity. In addition, as discussed earlier, the gas molecules at the elevated temperature involved for the morphology to look different, the thermal transfer by heavy gas molecules could have played a role to destroy the core-shell

structure of the NCs. In Ar, the full conversion of the metal to oxide phase could also be due to the complete destruction of the core-shell structure during annealing by diffusion or may be due to surface melting of the NCs at high-temperature and the metal gets oxidized when removing out of the heating chamber in air at room temperature. The destruction of the core-shell structure of the NCs may also be due to faster cooling rate from high-temperature to room temperature in gaseous medium when allowing them to cool naturally.

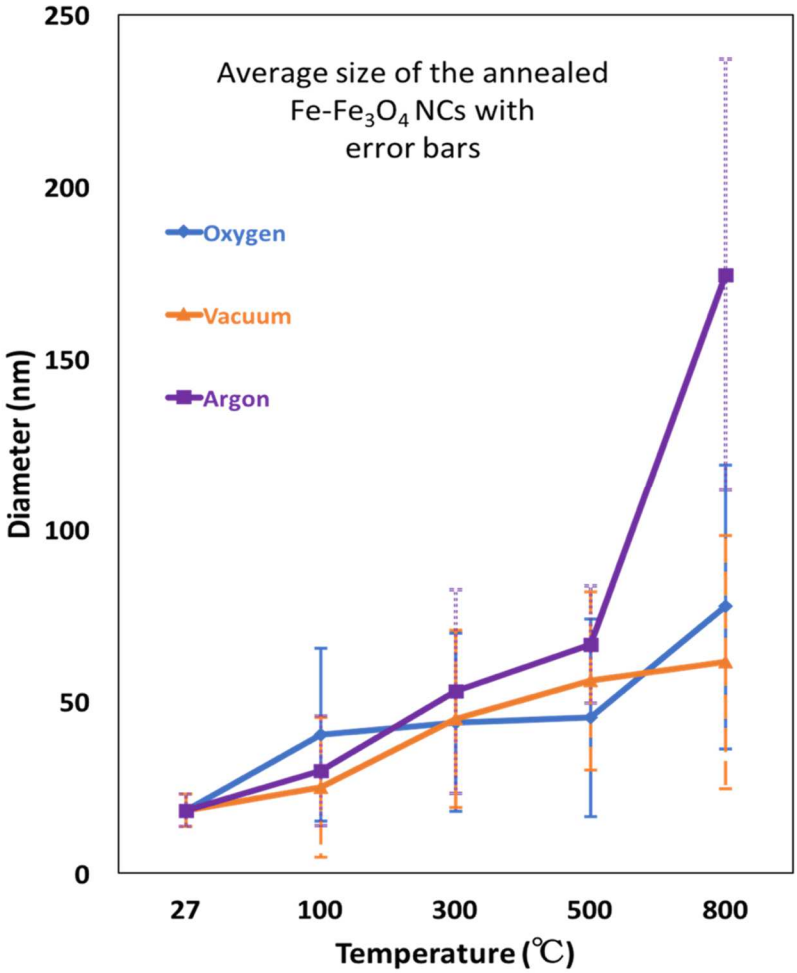

Figure 4.6 Average sizes with error bars of the NCs annealed at different conditions.

In order to study the size distribution of the NCs, ImageJ software was used to estimate the size of the pre- and post-annealed NCs at different temperatures from the SEM images. Figure 4.6

depicts the growth of the average size with the increasing temperature. The ~18 nm average size of the NCs has been found to increase slowly in all the three environments up to 500 °C. The almost constant size growth in O_2 environment from 300 °C to 500 °C may be due to the formation of voids by vacancy clustering caused by the difference in the diffusivities of Fe and oxygen ions through the oxide layer popularly known as Kirkendal voids[29,30] and the shrinkage of the voids by outward diffusion of the vacancy with increasing temperature.[31,32] Nakamura et al.[31] reported the transition temperature for the shrinkage of the voids during the oxidation of the iron nanoparticles as 400 °C, which makes our result plausible. The further increase in the size of the NCs on increasing the temperature is attributed to the cluster aggregation and coalescence of the clusters as illustrated by the schematic in Figure 4.3. At 800 °C, the average size of the particles has been found to grow slowly in Vac. and O_2 however it increases abruptly in Ar as shown in Figure 4.6. The faster cooling and convective thermal transfer by heavier Ar gas could have influenced further for the clusters aggregation resulting in larger size of the particles. The increasing size of the error bars with the rise in temperature indicates the growth is not uniform throughout the sample. During the coalescence, the larger particle is getting bigger and smaller particle is getting smaller, which makes the variation in sizes of the particle throughout the sample plausible.

The average size of Fe crystals, t, of the as prepared and vacuum annealed at 800 °C was also estimated by using the Scherrer equation[26]

$$t = \frac{C\lambda}{B\cos\theta_B} \tag{4.3}$$

Where C=0.9 is a constant, θ_B is the Bragg angle, λ is the X-ray wavelength (1.54 Å), and B is the full width at half maximum (FWHM). The average crystal size of Fe before and after annealing in Vac. were determined from the Fe (110) peak. The average ~12 nm size of the Fe core crystal has been found to increase to ~36 nm after annealing at 800 °C. The size growth of Fe crystal up on annealing at high-temperature could be the result of Ostwald ripening,[33,34] i.e. the larger crystals increase their

sizes at the expense of the surrounding smaller crystals and/or amorphous particle as described earlier in the coalescence mechanism. In addition, the reduction of the Fe_3O_4 to Fe and diffusion of Fe into the core could have played a role to overall increase in the size of the core.

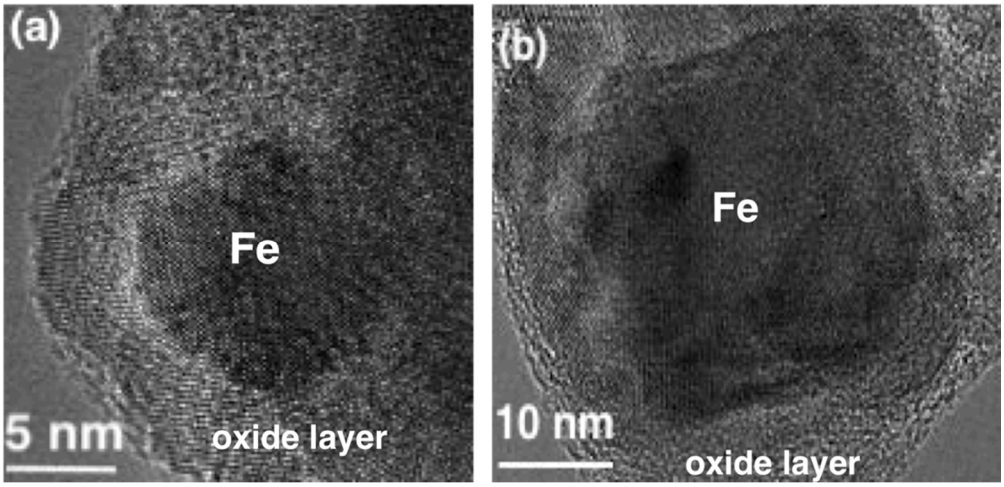

Figure 4.7 NC TEM micrographs of (a) As-prepared, and (b) annealed at 800^0C in vacuum

In addition, for the confirmation of the size and the retaining of the core-shell structure, we have studied the NCs as-prepared and annealed at 800 ^{0}C in vacuum with TEM as illustrated in Figure 7. The TEM micrograph (FIG. 7b) confirms the presence of the core-shell structure even after annealing in vacuum at 800 ^{0}C. Further, the micrograph is in well agreement with the size of the Fe core estimated from the XRD peaks.

4.5. Conclusion

Fe-Fe_3O_4 core-shell NCs prepared by state-of-the-art cluster deposition technique on annealing at high-temperature in Ar and O_2 have been observed with the presence of a new phase Fe_2O_3, loss of Fe-core, dramatic changes in the microstructures with the enhanced porosities and increase in the average particle size. In contrary, the NCs have shown very stable crystal structure with the consistent size growth and a small change in the microstructures even at 800 °C in the vacuum environment. The particle aggregation and coalescence of the particles are responsible for the size growth of the NCs at

the elevated temperature. The stability of the core-shell structure of the NCs in vacuum is very useful to design a radiation detector for the real-time monitoring of the radiation fluxes in the high-temperature core of the upcoming generation IV nuclear reactor. However, further investigations under ion and/or fast neutron irradiation at high temperature are required for the development of a radiation nanodetector.

4.6. Acknowledgments

This work was supported by U.S. Department of Energy (DOE) under Contract DE-FC07-08ID14926, by the INL-LDRD administered by CAES under the DOE Contract DE-AC07-05ID14517.

4.7. References

(1) Wu J et al. Broadband Efficiency Enhancement in Quantum Dot Solar Cells Coupled with Multispiked Plasmonic Nanostars. *Nano Energy* **2015**, *13*, 827.

(2) De Carlan Y, B. J.-L., Dubuisson P, Seran J. L, Billot P, Bougault A, Cozzika T, Doriot S, Hamon D. and Henry J. CEA Developments of New Ferritic ODS Alloys for Nuclear Applications. *J. Nucl. Mater.* **2009**, *386*, 430.

(3) Luchini A et al. Smart Hydrogel Particles: Biomarker Harvesting: One-Step Affinity Purification, Size Exclusion, and Protection against Degradation. *Nano Lett.* **2008**, *8*, 350.

(4) Klueh R L, M. P. J., Kim I. S, Heatherly L, Hoelzer D. T, Hashimoto N, Kenik E. A. and Miyahara K. Tensile and Creep Properties of an Oxide Dispersion-Strengthened Ferritic Steel. *J. Nucl. Mater.* **2002**, *307–11*, 773.

(5) Zhang X X, W. G. H., Huang S, Dai L, Gao R. and Wang Z. L. Magnetic Properties of Fe Nanoparticles Trapped at the Tips of the Aligned Carbon Nanotubes. *J. Magn. Magn. Mater.* **2001**, *231*, 9.

(6) Hu S, L. Y., McCloy J, Montgomery R. and Henager C. Magnetic Hardening from the Suppression of Domain Walls by Nonmagnetic Particles. *IEEE Magn. Lett.* **2013**, *4*, 3500104.

(7) Hu J, C. G. and L. I. M. Removal and Recovery of Cr (VI) from Wastewater by Maghemite Nanoparticles. *Water Res.* **2005**, *39*, 4528.

(8) Hu J, C. G. and L. I. M. Selective Removal of Heavy Metals from Industrial Wastewater Using Maghemite Nanoparticle: Performance and Mechanisms. *J. Environ. Eng.* **2006**, *132*, 709.

(9) Kaur M, Z. H., Martin L, Todd T. and Qiang Y. Conjugates of Magnetic Nanoparticle Actinide Specific Chelator for Radioactive Waste Separation. *Environ. Sci. Technol.* **2013**, *47*, 11942.

(10) Kaur M, J. A., Tian G, Jiang W, Rao L, Paszczynski A. and Qiang Y. Separation Nanotechnology of Diethylenetriaminepentaacetic Acid Bonded Magnetic Nanoparticles for Spent Nuclear Fuel. *Nano Energy* **2013**, *2*, 124.

(11) Qiang Y, A. J., Sharma A, Nutting J, Sikes D. and Meyer D. Iron/Iron Oxide Core–Shell Nanoclusters for Biomedical Applications. *J. Nanoparticle Res.* **2006**, *8*, 489.

(12) Jiang W, S. J. A., Varga T, Bowden M. E, Qiang Y, McCloy J. S, Henager C. and Montgomery R. O. In Situ Study of Nanostructure and Electrical Resistance of Nanocluster Films Irradiated with Ion Beams. *Adv. Funct. Mater.* **2014**, *24*, 6210.

(13) Kaur M, M. J. S., Jiang W, Yao Q. and Qiang Y. Size Dependence of Inter-and Intracluster Interactions in Core–Shell Iron–Iron Oxide Nanoclusters. *J. Phys. Chem.* **2012**, *116*, 12875.

(14) Kaur M, Q. Y., Jiang W, Pearce C. and McCloy J. S. Magnetization Measurements and XMCD Studies on Ion Irradiated Iron Oxide and Core–Shell Iron/Iron-Oxide Nanomaterials. *IEEE Trans. Magn.* **2014**, *50*, 1.

(15) Kaur M, M. J. S. and Q. Y. Exchange Bias in Core–Shell Iron–Iron Oxide Nanoclusters. *J. Appl. Phys.* **2013**, *113*.

(16) Kaur M, M. J. S., Kukkadapu R. K, Pearce C. I, Tuček J, Bowden M, Engelhard M. H, Arenholz E. and Qiang Y. Tetragonal like Phase in Core–Shell Iron Iron-Oxide Nanoclusters. *J. Phys. Chem.* **2017**, *121*, 11794.

(17) Sundararajan J A, K. M. and Q. Y. Mechanism of Electron Beam Induced Oxide Layer Thickening on Iron–Iron Oxide Core–Shell Nanoparticles. *J. Phys. Chem.* **2015**, *119*, 8357.

(18) Rioult M, S. D., Fonda E, Barbier A. and Magnan H. Oxygen Vacancies Engineering of Iron Oxides Films for Solar Water Splitting. *J. Phys. Chem.* **2016**, *120*, 7482.

(19) Was G S. *Fundamentals of Radiation Materials Science: Metals and Alloys* **2016**.

(20) Cornell R M and Schwertmann U. *The Iron Oxides: Structure, Properties, Reactions, Occurrences and Uses* **2003**.

(21) Atkinson A. Transport Processes during the Growth of Oxide Films at Elevated Temperature. *Rev. Mod. Phys.* **1985**, *57*, 437.

(22) Cabrera N and Mott N F. Theory of the Oxidation of Metals. *Sir Nevill Mott ? 65 Years in Physics* **1995**, 185.

(23) Fung K K, Q. B. and Z. X. X. Passivation of α-Fe Nanoparticle by Epitaxial γ-Fe2O3 Shell. *Mater. Sci. Eng.* **2000**, *286*, 135.

(24) Linderoth S, M. S. and B. M. D. Oxidation of Nanometer-Sized Iron Particles. *J. Mater. Sci.* **1995**, *30*, 3142.

(25) Lee S Y, M. N., Nguyen N, Sun Y. M. and White J. M. Copper Oxide Reduction through Vacuum Annealing. *Appl. Surf. Sci.* **2003**, *206*, 102.

(26) Cullity B D and Weymouth J W. Elements of X-Ray Diffraction. *Am. J. Phys.* **1957**, *25*, 394.

(27) Kole A K and Kumbhakar P. Cubic-to-Hexagonal Phase Transition and Optical Properties of Chemically Synthesized ZnS Nanocrystals. *Results Phys.* **2012**, *2*, 150.

(28) Gossmann H-J, R. C. S., Unterwald F. C, Boone T, Mogi T. K, Thompson M. O. and Luftman H. S. Behavior of Intrinsic Si Point Defects during Annealing in Vacuum. *Appl. Phys. Lett.* **1995**, *67*, 1558.

(29) Smigelskas A D and Kirkendall E O. Zinc Diffusion in Alpha Brass. *Trans. AIME* **1947**, *171*, 130.

(30) Nakajima H. The Discovery and Acceptance of the Kirkendall Effect: The Result of a Short Research Career. *JOM J. Miner. Met. Mater. Soc.* **1997**, *49*, 15.

(31) Nakamura R, M. G., Tsuchiya H, Fujimoto S. and Nakajima H. Transition in the Nanoporous Structure of Iron Oxides during the Oxidation of Iron Nanoparticles and Nanowires. *Acta Mater.* **2009**, *57*, 4261.

(32) Jaffari G H, C. A., Ni C. and Shah S. I. Enhancement of Surface Spin Disorder in Hollow NiFe2O4 Nanoparticles. *J. Appl. Phys.* **2010**, *107*.

(33) Marqusee J A and Ross J. Theory of Ostwald Ripening: Competitive Growth and Its Dependence on Volume Fraction. *J. Chem. Phys.* **1984**, *80*, 536.

(34) Ratke L and Voorhees P W. *Growth and Coarsening: Ostwald Ripening in Material Processing* **2013**.

Chapter 5: Relationship between Nanostructure-Magnetic Property Induced by Temperature for Iron Oxide Nanoparticles in Vacuum, Ar and O_2 Environments

Khanal, L. R.; Ahmadzadeh, M.; McCloy, J. S.; Qiang, Y. Relationship between Nanostructure-Magnetic Property Induced by Temperature for Iron Oxide Nanoparticles in Vacuum, Ar and O_2 Environments. *Journal of Magnetism and Magnetic Materials* **2020**, *498*, 166158.

5.1. Abstract

It is known that superparamagnetic magnetite (Fe_3O_4) nanoparticles (NPs) become ferromagnetic under Si^{2+} ion irradiation due to particle size growth and microstructure evolution; it has been proposed that this feature could be used for in situ high temperature (up to 500°C) radiation monitoring in the core of nuclear reactors. Herein, magnetite NPs synthesized by a nanocluster deposition system are heated to 800°C in three different environments (argon, oxygen and vacuum), and nanostructure-magnetic property correlations are investigated by vibrating sample magnetometry, scanning electron microscopy, and X-ray diffraction. Magnetization of the NPs is increased due to the sintering and overall size growth by the agglomeration of the particles, while the morphology remains nearly unchanged up to 800°C, with the one anomaly that zerovalent Fe appeared due to the reduction of the Fe_3O_4 at 800°C in vacuum. In argon and oxygen at high-temperature, antiferromagnetic hematite is created, which causes a reduction of the magnetization, and abrupt growth of particle size above 500°C.

5.2. Introduction

Magnetic nanomaterials have obtained tremendous attention over the past few decades because of their interesting properties. Magnetic nanoparticles (NPs) have been promisingly used in biomedical applications[1–3], magnetic recording media[4,5], wastewater treatment[6,7], nuclear waste treatment[8,9] and catalytic applications.[10,11] Our previous studies reported that the core-shell Fe-Fe_3O_4 NP is a promising material for radiation sensing, as it demonstrates sensitive electrical conductivity

changes under ion irradiation.[12] Further, the stable nanostructure and phase of the core-shell NP at high-temperature in vacuum suggests it could be used in nuclear reactor cores (up to 500°C) as a sensing material.[13] In a separate study, a superparamagnetic porous granular film of magnetite (Fe_3O_4) with 3 nm nanocluster size showed ferromagnetic behavior due to the dramatic change in microstructure after ion irradiation at room temperature.[14] These studies together suggested that magnetite granular films could be promising materials for radiation monitoring or advanced data storage in extreme environments, such as high temperature or pressure. The high temperature and pressure may give rise to change in bond lengths, angles, and coordination number at surfaces and interfaces of nanostructures, which can cause a significant alteration of magnetic properties of these materials.[15–17] Thus, understanding the temperature-induced nanostructure-magnetic property relationship of granular films is very important for controlled tuning of magnetic behaviors and tailoring the advanced devices that need to perform in extreme conditions.

Herein, we report the response of fully oxidized Fe_3O_4 NPs to temperature in the presence of different atmospheres, argon (Ar), oxygen (O_2) and vacuum (Vac.). The model porous granular Fe_3O_4 films for this study are prepared by a cluster deposition system that combines magnetron sputtering with a gas condensation technique through controlled oxidation of zerovalent iron NPs.

5.3. Experimental Details

The Fe_3O_4 NPs were prepared by a custom nanocluster deposition system. The detailed description of the fabrication of granular films by this method was described in previous papers[13,14,18] and briefly summarized here as well. Fe NPs were obtained from a Fe-target cathode mounted on a sputtering gun inside the aggregation chamber. The DC power (200 W) applied to the gun allowed the argon (Ar) gas in the aggregation chamber to be ionized. The energetic Ar^+ ions knocked out the Fe-atoms from the surface of the target. The iron atoms were allowed to fully oxidize by injecting oxygen gas (~3 standard cubic centimeters per minute) into the aggregation chamber to obtain Fe_3O_4 NPs. The

NPs were collected through low temperature (-7°C) condensation in the aggregation chamber. The pressure difference of 10^{-3} Torr between the aggregation chamber and the deposition chamber allows the NPs to travel towards the deposition chamber, where the NPs are collected on the surfaces of 10 mm × 10 mm Si (100) substrate at room temperature (RT) in the form of granular films.

The as-prepared granular films on the Si substrates were heat-treated in a Lindberg mini furnace at maximum temperatures of 100°C, 300°C, 500°C, or 800°C, in Vac., Ar, or O_2. The NPs were heated at the 25°C/min, held for 1 hour at the maximum temperature, and then allowed to cool down naturally to RT with the furnace turned off. The cooling time period from 800°C was slower in Vac. (by ~ 1 hour) than in the gaseous media (Ar or O_2). Vac. was tested to simulate the environment in the core of the nuclear reactor; O_2 was tested to study behavior in air or in an open environment. Inert Ar gas was tested as a possible protective environment for the NPs at high temperature.

The phase transformation and crystal structure, surface morphology, and size of the NPs, were studied pre- and post- heat-treatment, respectively, by an X-ray Diffractometer (XRD, Siemens D5000) with Solex solid-state detection system and CuKα line (1.54 Å), and a JEOL JSM scanning electron microscope (SEM) and ImageJ software. The investigation of the magnetic properties before and after heat treatment were observed by a vibrating sample magnetometer (VSM, PMC3900, Lakeshore Cryotronics, Westerville, OH) with maximum external applied field of ±15 kOe and field increment of 50 Oe. The sample surface was held parallel to the applied magnetic field during the measurement.

5.4. Results and Discussion

5.4.1. High-Temperature Study of Structure, Morphology and Particle Size of Fe_3O_4 NPs

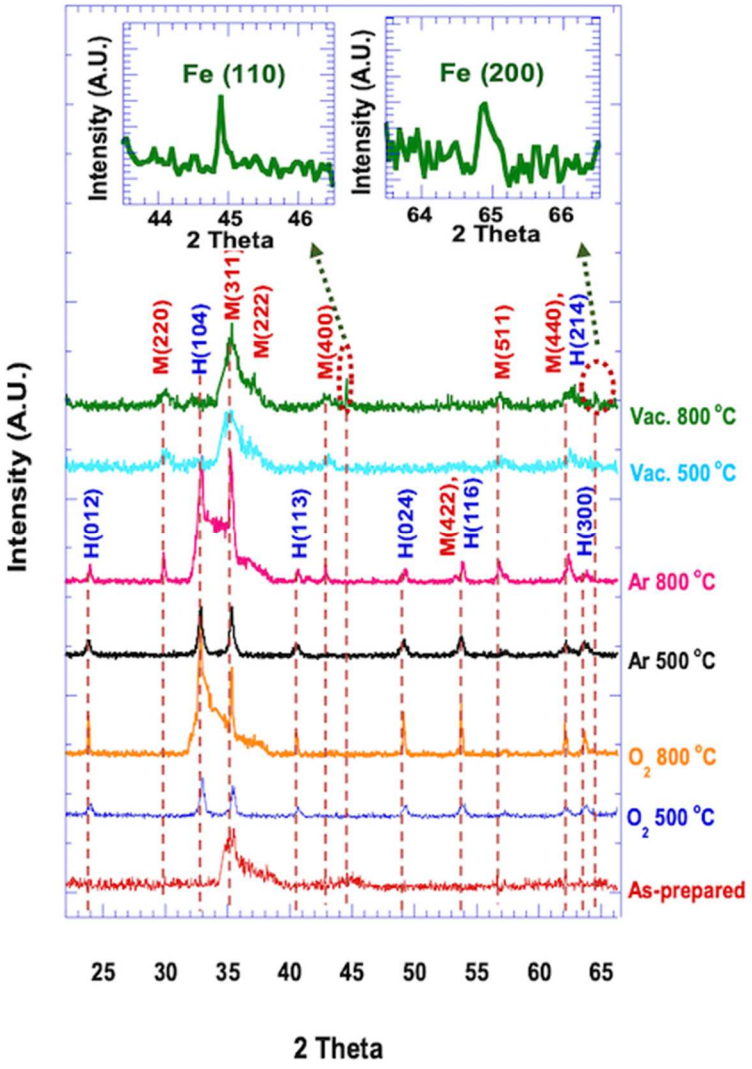

Figure 5.1 X-ray diffraction results for the NPs before and after heat-treatment under different conditions. M and H are Magnetite and/or Maghemite, and Hematite phases, respectively.

X-ray Diffraction (XRD).

Figure 5.1 shows the XRD spectra of the NPs as-prepared and heat-treated at different conditions. The XRD patterns of the as-prepared NPs show an oxide of iron that can be identified as one or more of the following: spinel structure, i.e., magnetite (Fe_3O_4) or maghemite (γ-Fe_2O_3); and corundum structure hematite (α-Fe_2O_3). Since the XRD peak of the Fe_3O_4 (311), γ-Fe_2O_3 (311) and α-

Fe_2O_3 (110) are very close to each other, it is very difficult to distinguish these phases from the XRD based on this peak alone.[19]

The EDS spectrum shown in Figure 5.2 confirms that the as-prepared sample is composed only of the iron and oxygen. The silicon and carbon peaks in the image belong to the substrate and the carbon tape (used to stick the sample), respectively. Table 5.1 shows the atomic percentage of Fe and O in the as-prepared and heat-treated samples obtained from EDS, compared with that of the ideal Fe_3O_4 and Fe_2O_3. The atomic percentage of the Fe (43.2%) and oxygen (56.8%) in the as-prepared samples are close to the compositions of the ideal Fe_3O_4. Overall, the XRD and EDS data suggests that the as-prepared film is a typical inverse spinel magnetite. A similar previous work on the iron-oxide NPs also confirms the presence of a single-phase cubic magnetite in the as-prepared granular film.[14]

On heat treatment of the NPs at 100°C and 300°C, no new phases are detected by XRD, regardless of heating environment (spectra not shown here). However, heat treatment at 500°C and 800°C create new peaks corresponding to magnetite/maghemite and/or hematite phases. As discussed earlier, since the peaks Fe_3O_4 (311), γ-Fe_2O_3 (311) and α-Fe_2O_3 (110) are very close to each other, it is difficult to distinguish the exact phase from the peak at 2-theta = ~35°. The EDS data from Table 5.1 shows that the oxygen composition in the as-prepared NPs increases from 56.8% to 67.5% in O_2 and 62.7% in Ar at 800°C, which confirms the oxidation of the Fe_3O_4 at 800°C. Thus, the reflections M (311)/H (110), M (440)/H (214) and M (422)/H (115) at 800°C in Ar and O_2, as depicted in XRD spectra, are most likely α-Fe_2O_3.

The mechanism of the distortion of the original inverse spinel phase and appearance of the corundum structure is followed by the migration of the iron ions to the surface and subsequent oxidation.[20,21] The high temperature oxidation in Ar is due to the small traces of oxygen impurities present in the ultra-high pure Ar gas as reported in previous work [13]. Several other reports indicate that oxidation of the very reactive iron-based NP during heat treatment in Ar at high temperature is

possible.[22,23] α-Fe_2O_3 is the most stable oxide, while Fe_3O_4 and γ-Fe_2O_3 are unstable beyond 350°C in ambient air environments.[24,25] Thus, the presence of the α-Fe_2O_3 peaks on XRD pattern, for samples treated at 800°C in O_2 and Ar, is plausible.

Fe_3O_4 oxidizes to α-Fe_2O_3 via metastable γ-Fe_2O_3 .[26] The M (511), M (400), and M (220) peaks have also been observed in Ar-800 (refers to Ar environment at 800°C) samples. These peaks cannot be Fe_3O_4 per the oxygen percentage from EDS data. The peaks must correspond to metastable γ-Fe_2O_3 formed during the oxidation process, which are not changed completely to α-Fe_2O_3 in the very low oxygen concentration environment. Oxidation of Fe_3O_4 progress increases with oxygen concentration.[27] The absence of these peaks for samples treated in Ar $\leq$ 500°C is possibly due to smaller crystallite size, which could not be detected by XRD due to excessive broadening. The presence of these peaks in Ar-800 sample is due to the increase in crystallite size, such as is achieved through Ostwald ripening,[28,29] where the crystallites increase their size at the expense of surrounding smaller crystallites and/or amorphous particles.

The atomic percentage of oxygen in the Ar-500 sample (58.07 atomic%) is just slightly above that of the as-prepared sample as given by EDS in Table 5.1. Owing to very little change in atomic percentage of O in EDS data, most of the peaks in Ar-500 in XRD indicate Fe_3O_4 and/or γ-Fe_2O_3. It is likely that XRD peaks at 2-theta = ~35° and ~ 54°, which are close to all three iron oxide phases (Fe_3O_4, γ-Fe_2O_3 and α-Fe_2O_3) correspond to Fe_3O_4 and/or γ-Fe_2O_3. The slight increase in the oxygen percentage as given by EDS also indicates that the Fe_3O_4 should have started oxidizing at 500°C in Ar, and the presence of few α-Fe_2O_3 peaks are reasonable. At lower temperatures (100°C and 300°C) in Ar, the oxidation might have not been activated due to low oxygen concentration.

The presence of α-Fe_2O_3 peaks and no additional Fe_3O_4 peaks in O_2 samples treated at 500°C and 800°C indicate the complete conversion of the Fe_3O_4 to α-Fe_2O_3 due to oxidation. The EDS data in

Table 5.1 for oxygen treated samples at 500°C and 800°C shows the atomic percentage of oxygen in the sample is more than that of the as-prepared sample. The atomic percentage of the oxygen at 500°C becomes closer to that of the ideal Fe_2O_3, and even more at 800°C, thus confirming the complete oxidation of the Fe_3O_4 NPs at 500°C. Lehlooh et al. provided evidence for the complete conversion of Fe_3O_4 to α-Fe_2O_3 at 550°C in ambient air atmosphere.[26] However, our work shows the complete conversion of Fe_3O_4 to α-Fe_2O_3 at 500°C; this is plausible because of the oxygen-rich atmosphere in our case. The oxidation of Fe_3O_4 in O_2 may have started at room temperature, but the process is slow[27] and cannot lead to complete oxidation to α-Fe_2O_3 without elevated temperature. A previous work showed that when Fe_3O_4 fine particles were heated in air at different temperatures up to 300°C, samples progressively transformed to γ-Fe_2O_3.[26] Thus, the absence of new XRD peaks for samples treated at 100°C and 300°C could be due to the indistinguishable signature of the conversion of the Fe_3O_4 to γ-Fe_2O_3 by XRD.

After heat treating in vacuum at 500°C, the NPs present a few additional peaks {M (220), M (400), M (511) and M (440)} not present in as-prepared NPs. These peaks may correspond to either Fe_3O_4 or γ-Fe_2O_3. However, Table 5.1 shows that the atomic percentage of oxygen decreases slightly from that of the as-prepared NPs. This indicates that the peaks do not correspond to γ-Fe_2O_3. The smaller oxygen percentage is due to reduction of the Fe_3O_4 to metallic Fe at 500°C in Vac. However, we are not able to see any Fe peaks in XRD for these samples. The reduction could have just started at 500°C, and the Fe crystallites are not large enough to be detected by XRD. Literature has reported that the reduction of metal oxide to metal is possible during vacuum heat treatment, with an evidence of reduction of copper-oxide to copper.[30,31] The EDS data in Table 5.1 shows that the atomic percentage of the Fe at Vac. 800°C increases and that of the oxygen decreases significantly. This confirms the reduction of the Fe_3O_4 is significant at 800°C. XRD shows new Fe (110) and Fe (200) peaks at 2-theta

= 45° and 65°, which appears because of the reduction of Fe_3O_4 to Fe. The average size of the Fe crystallites is estimated by using the Scherer equation,[32] and found to be ~ 6 nm.

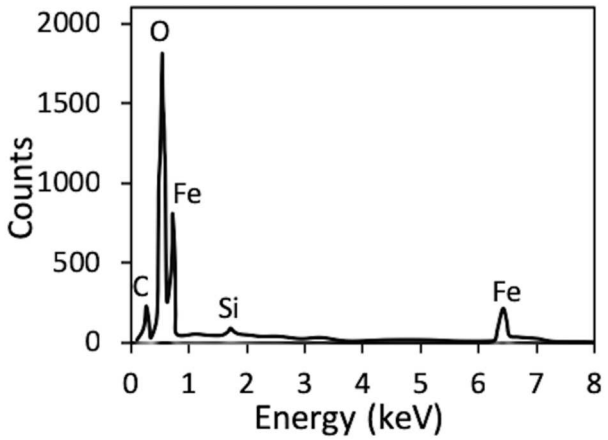

Figure 5.2 EDS spectrum of as prepared NPs

Table 5.1 Data (atomic percentage) extracted from the EDS analysis of the iron oxide NPs at different conditions

Element	Ideal		As-prepared	Vac.		O_2		Ar	
	Fe_3O_4	Fe_2O_3		500°C	800°C	500°C	800°C	500°C	800°C
O (%)	57.14	60	56.8	55.44	46.4	60.8	67.5	58.07	62.7
Fe (%)	42.86	40	43.2	44.56	53.6	39.2	32.5	41.93	37.3

Scanning Electron Microscopy (SEM)

The SEM images of the magnetite NPs as prepared (a) and after annealing in Vac. (b1-b3), O_2 (c1-c3), and Ar (d1-d3) environments are shown in the inset of Figure 5.3. The numbers 1-3 in b, c, and d represent the annealed magnetite NPs at 300°C, 500°C, and 800°C, respectively. No significant changes in surface morphologies have been observed when the NPs were heat treated up to 500°C in

any of the three environments. However, the nanostructures of the loosely aggregated as-prepared NPs have been found to change dramatically on heat treatment at 800°C in Ar environment, as shown in Figure 5.3 (inset d3). When the NPs were heat treated in O_2 at 800°C, the morphology changes significantly, with the concurrent formation of a nanowire-like network pattern as shown in Figure 5.3 (inset c3). It is plausible that the increasing temperature promotes particle convergence. With further increase in the temperature and/or heat treatment time, the particles acquire high thermal energy, which allows them to further approach and interconnect to give rise to a network-like structure as shown in Figure 5.3 (inset c3), or completely coalesce to give rise to larger particles (inset d3). The smaller particles with larger surface to volume ratio are more likely to combine into a larger particle on increasing temperature, which results in the larger particles getting larger, and smaller ones getting smaller and eventually disappearing. When the NPs are annealed at 800°C in Vac., the morphology does not show noticeable change, as depicted in Figure 5.3 (inset b3). The difference in the morphologies at 800°C in Vac. and gaseous mediums is possibly due to the slower cooling rate in Vac. The huge alteration of the morphology in the Ar environment could be due to the heat transfer to the NPs by heavy mass Ar gas molecules at elevated temperatures.

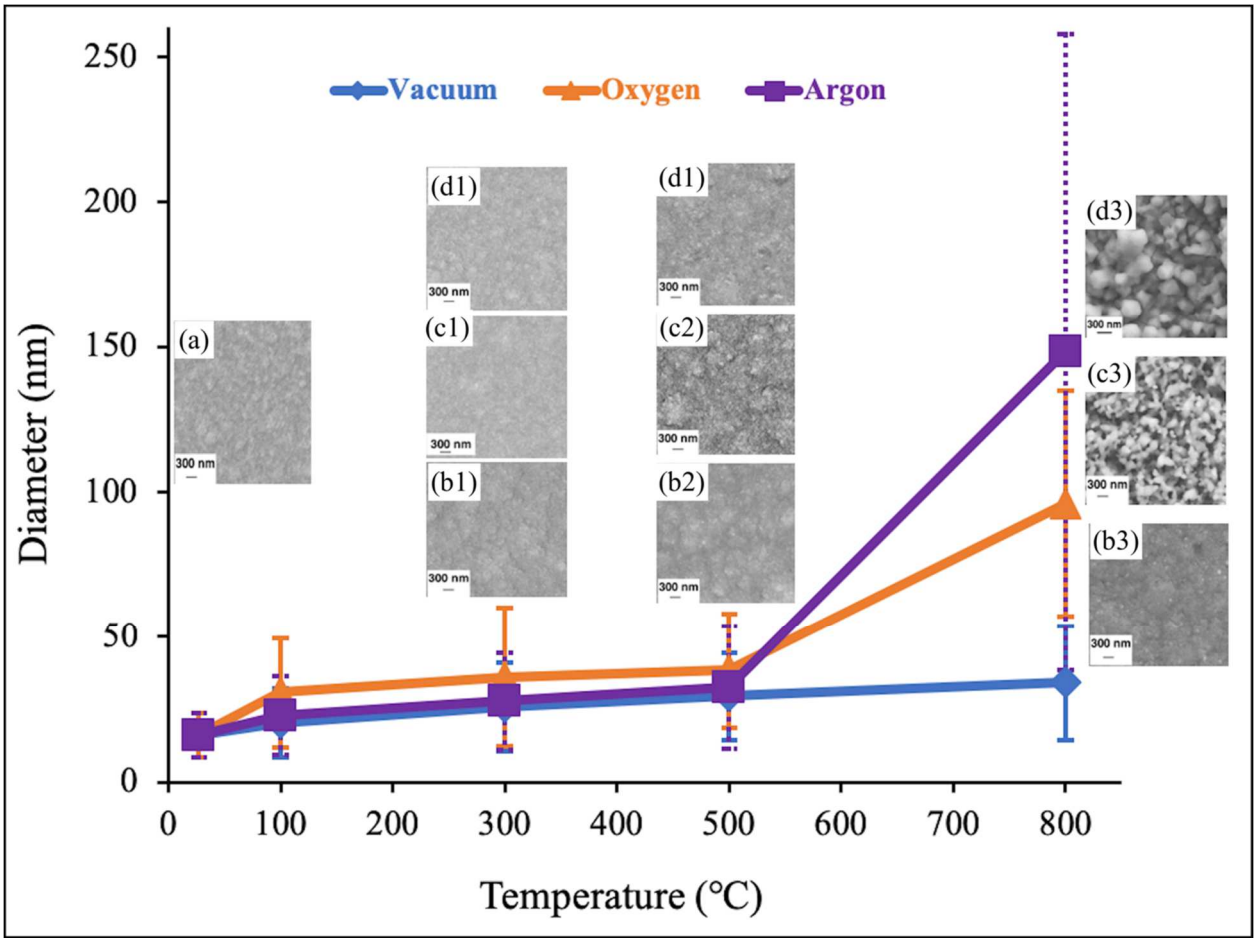

Figure 5.3 Average particle size with error bars of the NPs annealed at different conditions. The insets are the SEM images of the iron oxide NPs as-prepared (a) and annealed in Vacuum (b1-b3), Oxygen (c1-c3), and Argon (d1-d3) environments. The numbers 1-3 are annealed NPs at 300, 500 and 800 °C respectively.

In order to study the size distribution of the NPs, ImageJ software was used to estimate the cluster size of the pre- and post- treated NPs at from the SEM images. Figure 5.3 depicts the growth of the average size with the increasing temperature. The ~16 nm average size of the NP has been found to increase slowly in all the three environments up to 500°C. The particle size then increases dramatically at 800°C to 96 nm (O_2) or 148 nm (Ar). However, the trend of the slow growth in particle size remains consistent up to 800°C in Vac. and the size becomes 34 nm at 800°C.

The particle size growth with the temperature can be explained by (1) phase distortion of the original inverse spinel and migration of iron ions to the surface and subsequent oxidation,[20,21] and (2) coalescence of the NPs with increasing the temperature and/or heating time. Heat-treated samples thus have a large size distribution as represented by the increasing size of the error bars with the increasing temperature. The particle growth in Vac. must be only due to the coalescence of the particle up to 800°C. However, the particle size growth in O_2 is due to both mechanisms, oxidation and coalescence. For the particle size growth up to 500°C in Ar, coalescence would have played a more significant role than oxidation, since the oxidation in Ar has been just started from 500°C as discussed previously. The particle size growth in O_2, since the beginning, is more than that of the other two environments up to 500°C because the oxidation of the Fe_3O_4 starts from RT in oxygen rich environments. The growths are similar in Ar and Vac. because the growth is mostly by coalescence of the particles in both cases. However, the particle size at 500°C in Ar is larger, since the oxidation has started at this temperature in Ar. The abrupt increase in the particle size beyond 500°C in Ar and O_2 is because the oxidation mechanism is more prominent at this temperature in both environments. The thermal transformation by heavier Ar gas molecules could have influenced further for the clusters aggregation resulting in larger size of the particles than that in O_2 at 800°C. The increasing size of the error bars (large size distribution) with the rise in temperature indicates the growth is not uniform throughout the sample. During the coalescence, the larger particles are getting bigger and the smaller particles are getting smaller, which results in a larger variation in sizes of the particles for the sample processed at higher temperatures.

5.4.2. Magnetic Study from Vibrating Sample Magnetometer

Coercivity, Remanence and Magnetization

Figure 5.5-5.7 show magnetization (M) versus magnetic field (H), i.e. hysteresis loop, measurements performed on the pre- and post-heat-treated granular films at different temperatures in

three different environments. The hysteresis loop of the as-prepared granular film, included in all the figures as a reference, shows almost superparamagnetic behavior with small values of magnetic remanence (~1 emu/g) and coercivity (10 Oe). At maximum applied field of ±15 kOe, the samples acquire maximum magnetization and all of them are nearly saturated, as shown in Figure 5.5(a). The magnetization increases in Vac. from ~27 emu/g at RT to ~65 emu/g at 800°C. It can also be seen that the magnetic remanence increases from 1 to 7 emu/g (as represented in Figure 5.4), and coercivity from 10 to 75 Oe (as shown in figure 5.5 (b)). The overall increase in magnetization of the annealed NPs in Vac. is followed by the sintering and particle size growth from 16 nm to 34 nm due to coalescence of the NPs at elevated temperature. Also, as discussed earlier and represented in Table 5.1 and Figure 5.1, the NPs at high temperature (≥ 500°C) reduce to Fe in Vac. Since Fe has a greater magnetization, the larger value of the magnetization at higher temperature in Vac. is also due to the presence of the Fe crystallites in the film by reduction.

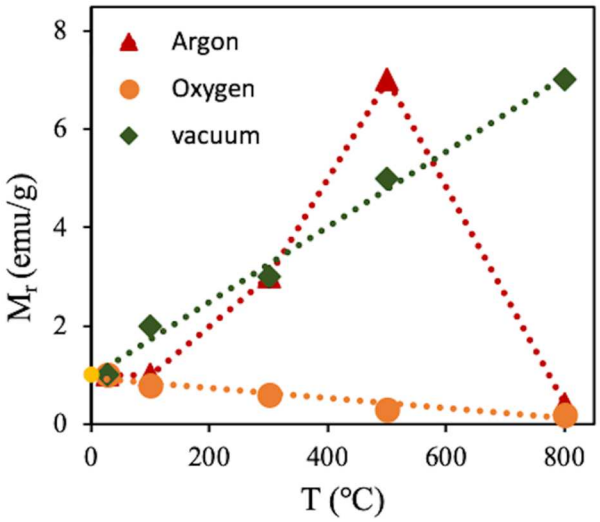

Figure 5.4 Magnetic remanence of the NPs annealed at different conditions

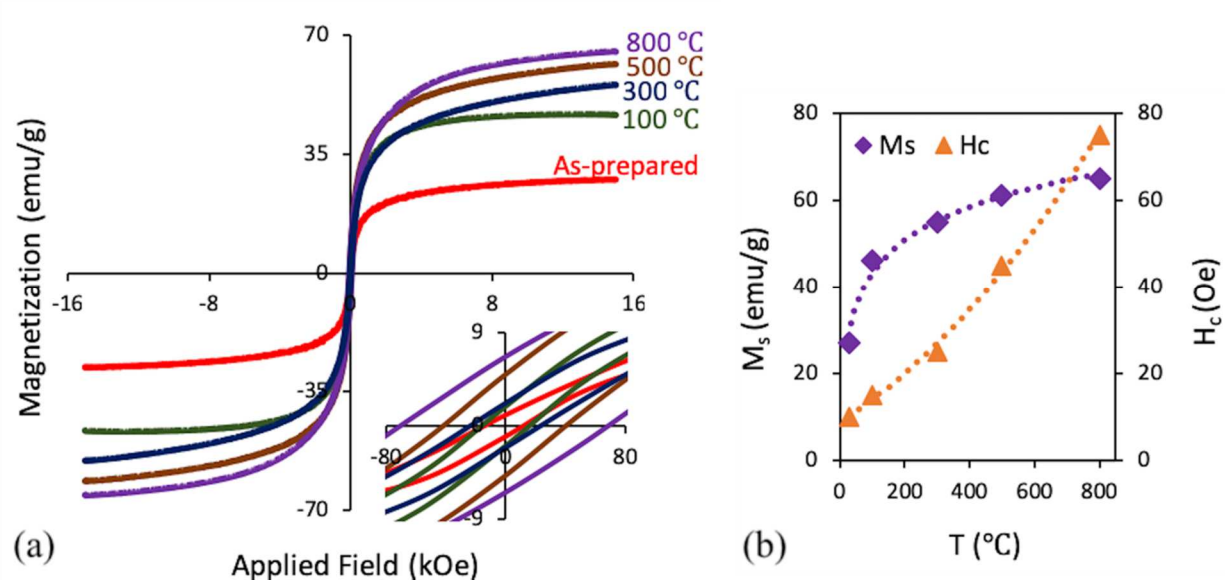

Figure 5.5 (a) Hysteresis curve and (b) saturation magnetization vs. temperature of the annealed magnetite samples at different temperature in vac. atmosphere

The hysteresis loops of the films before and after heat treatment in Ar are shown in Figure 5.6. The saturation magnetization first increases slowly up to 300°C from 27 to 44 emu/g. However, interestingly, the saturation magnetization decreases to 33 emu/g at 500°C and finally drops to 0.5 emu/g at 800°C. The increase in magnetization of the film up to 300°C is due to the sintering and particle size growth due to the coalescence of the NPs as in Vac. As seen from the EDS data in Table 5.1 and XRD in Figure 5.1, the Fe_3O_4 NPs start oxidizing at 500°C and α-Fe_2O_3 appears. α-Fe_2O_3 has canted antiferromagnetic behavior at room temperature with maximum magnetization ~0.4 emu/g, whereas Fe_3O_4 and γ-Fe_2O_3 are ferrimagnetic with saturation magnetization ~90 and ~80 emu/g, respectively.[24] Thus, the decrease in saturation magnetization in Ar from 500°C is due to the slight oxidation of the Fe_3O_4 to α-Fe_2O_3 as given by EDS and XRD as discussed in the previous section. At 800°C in Ar, Fe_3O_4 is almost completely oxidized to α-Fe_2O_3 and nearly saturated to the value close to the maximum magnetization of a bulk α-Fe_2O_3. The larger value (~1300 Oe) of the coercivity at 800°C is due to the conversion of the Fe_3O_4 to α-Fe_2O_3, since α-Fe_2O_3 has a very high coercivity (~ 1000 -

5500 Oe).[33,34] The magnetic remanence for samples treated in Ar, however, increases up to 500°C to 7 emu/g, unlike magnetic saturation, then drops to 0.4 emu/g at 800°C, as shown in Figure 5.4.

The wasp-waisted (or constricted near zero field) hysteresis loop in Ar-800 (shown in top-left inset image in Figure 5.6 (a)) may be the result of (i) larger variation in the size distribution of the NPs at high temperature, as indicated by the larger error bars in Figure 5.3, arising from inhomogeneous particle growth and/ or sintering,[35,36] and (ii) the presence of mixed phases of antiferromagnetic α-Fe_2O_3 and a small component of ferrimagnetic Fe_3O_4/γ-Fe_2O_3, as indicated by XRD in Figure 5.1. Such a mixture with contrasting coercivities result in a combination of the magnetic parameters and tendency toward one or another constituent, producing distinctive wasp-waisted shapes.[37,38] More contrast in the coercivities would result in the more wasp-waistedness.

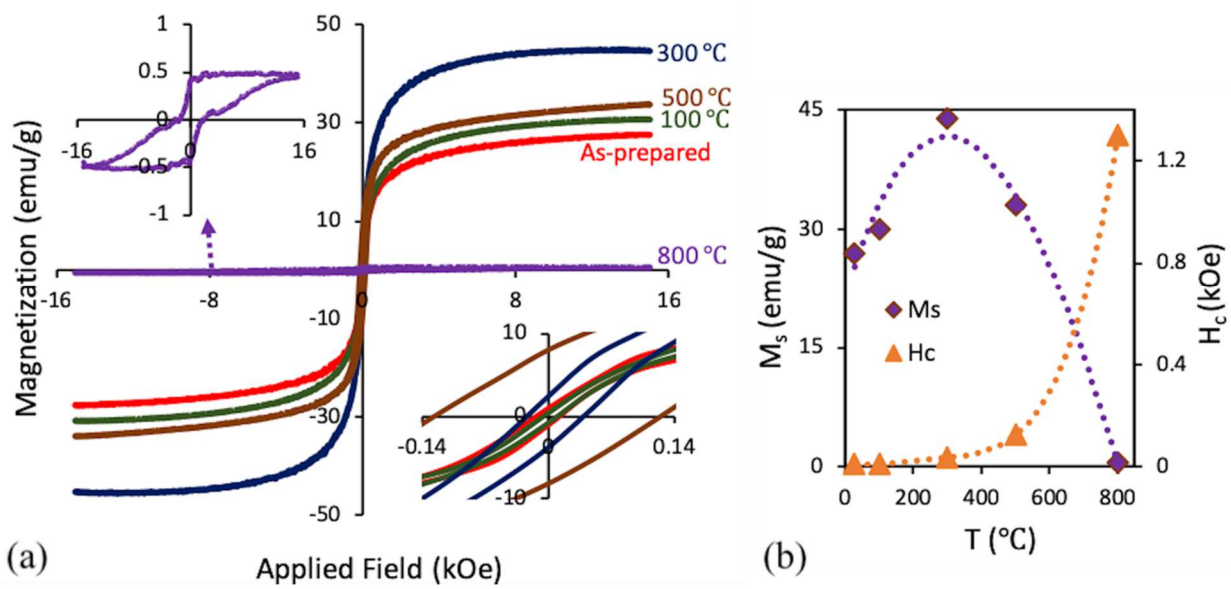

Figure 5.6 (a) Hysteresis curve and (b) saturation magnetization vs. temperature of the annealed magnetite samples at different temperature in Ar atmosphere. Lines in (b) are guides to the eye only.

Figure 5.7 shows the hysteresis curve of the NPs as-prepared and heat-treated in oxygen. As seen in Figure 5.7(b), the saturation magnetization decreases exponentially with increasing

temperature and approaches the saturation magnetization of the bulk α-Fe_2O_3. As discussed in the previous section, the decrease in the saturation magnetization is due to the oxidation of the Fe_3O_4 to α-Fe_2O_3. The remanence of the NPs also decreases gradually (shown in Figure 5.4), however, the coercivity increases with the increase in heat treatment temperature, as shown in Figure 5.7 (b). The decrease in remanence is also due to the oxidation of the NPs. The increase in coercivity with heat treatment temperature could have been caused by the oxidation of the NPs and the particle size growth at high temperature. The result is consistent with the result obtained by Krajewski et al.,[34] who reported that oxidizing Fe NPs at high-temperature causes the Fe NPs to gradually lose their remanence and gain coercivity due to the presence of the α-Fe_2O_3 NPs. They claimed that thermally-treated Fe NPs at high-temperature sinter and results in the formation of the larger particles composed of smaller particles as well. Consequently, the numerous defects, dislocations, and strains between the NPs are introduced to the obtained α-Fe_2O_3 aggregates, which in turn caused the enhancement of the coercivity. There are various other studies that support the notion that particle size growth enhances the coercivities of the α-Fe_2O_3.[39–41] The smooth hysteresis curve (unlike the wasp-waisted in Ar 800°C) even treated as high as 800°C in oxygen (as shown by top-left inset in figure 5.7(a)), is reasonable due to the presence of single phase α-Fe_2O_3 as supported by XRD in Figure 5.1.

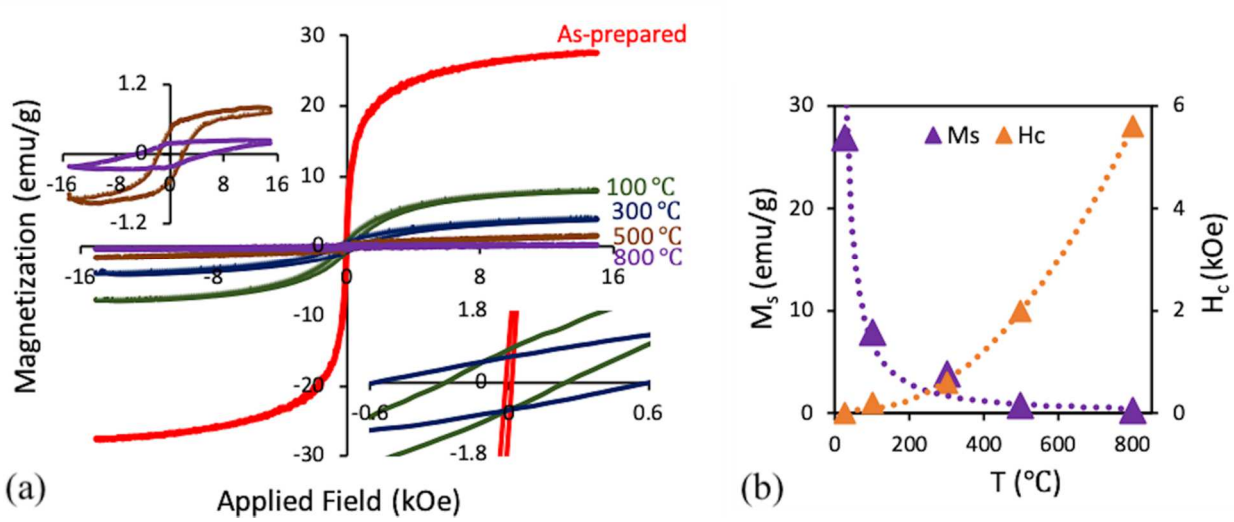

Figure 5.7 (a) Hysteresis curve and (b) saturation magnetization vs. temperature of the annealed magnetite samples at different temperature in oxygen atmosphere.

Maximum Energy Product

The energy product of a magnet is associated with H_c and M_r/M_s and influences the shape of the demagnetization curve (flux density (B) vs H curve), essentially a measure of squareness of the hysteresis loop. The demagnetization curve generally implies the effect of exposure of low or high temperatures and /or magnetic fields.[42] The effect is irreversible, i.e. the magnetization will not return to the original state even when the temperature or magnetic field return to the initial state. The energy product depends on the total area enclosed by the hysteresis loop and is affected by the change in H_c and M_r/M_s.

In order to understand the largest possible magnetic energy that can be achieved in the NPs considering an idealized rectangular M(H) hysteresis loop, we estimated the possible ideal maximum energy product, $|B.H|_{max}$, of the Fe_3O_4 NPs as-prepared and annealed in Ar, O_2 and Vac. at different temperature using the following equations.[43,44] First, the energy product is:

$$|B \cdot H| = -\mu_0 (M_s + H) \cdot H$$

(5.1).

Next, differentiating equation (1) with respect to H and equating to zero gives $H = -M_s/2t$, Maximum energy product is found by substituting $H = -M_s/2$, then,

$$|B \cdot H|_{max} = -\mu_0 (M_s - M_s/2) \cdot (-M_s/2) = (1/4)\mu_0 M_s^2$$

(5.2).

The change in $|B \cdot H|_{max}$ with temperature in different environments is represented in Figure 5.8. It has been found that $|B \cdot H|_{max}$ increases from 6 kJ/m^3 to 36 kJ/m^3 when temperature increases from RT to 800°C in Vac. The magnetite NPs at higher temperature become denser and improve magnetic orientations. However, in Ar environments the maximum energy product increases until 300°C to a value of 16.5 kJ/m^3 and then starts decreasing to 0.002 kJ/m^3 at 800 °C. The increase in the first part is due to the increase in average particle size by sintering the NPs, and then the decrease in energy product is due to the gradual oxidation of the Fe_3O_4 at higher temperature. The significant drop in the value of the maximum energy product in O_2 is due to the oxidation of the Fe_3O_4, which starts from RT. The larger value of H_C (5600 Oe) and M_r/M_s (0.67) at 800°C in O_2 environment further indicates α-Fe_2O_3, which is a canted antiferromagnet, a weakly magnetic, but hard (high coercivity) magnet material.

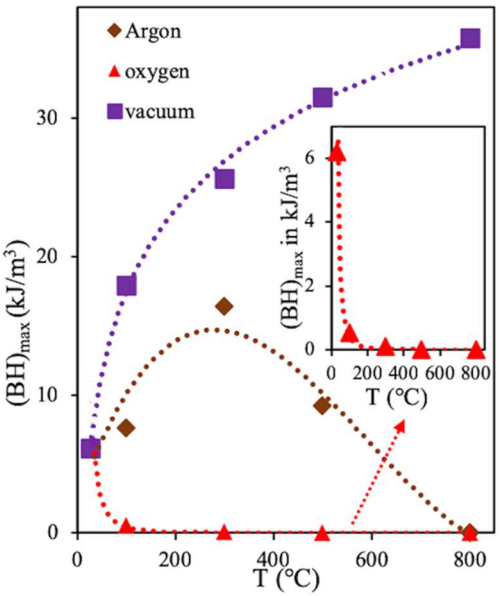

Figure 5.8 Maximum energy product, $(BH)_{max}$, vs. temperature of the annealed magnetite NPs at different conditions.

5.5. Conclusion

Fe_3O_4 NPs synthesized by a cluster deposition technique followed by heat treatment at high-temperature have been observed to oxidize completely (when treated in O_2) or almost completely (when treated in Ar), which results in a significant decrease in the saturation magnetization. The oxidation in Ar starts at temperatures higher than 300°C, but in oxygen the oxidation starts when heating even at room temperature. There is dramatic change in the surface morphology and abrupt increase in the particle size due to coalescence and oxidation of the NPs at 800°C.

However, when the NPs are annealed in vacuum, stable surface morphologies have been observed even at high-temperature. The saturation magnetization increases from 27 emu/g to 65 emu/g followed by the gradual growth of the particles due to coalescence and sintering at higher temperature. The NPs in vacuum at temperatures 500°C and above, interestingly, start to reduce due to the oxygen-deficient environment, an effect that becomes significant at 800°C. Since the core of a nuclear reactor is vacuum, the evidence of a stable nanostructure with enhanced magnetization at the elevated

temperature in vacuum strengthens the possibility for suitability of these magnetite NPs as in-situ radiation sensor materials for next generation nuclear reactor, as well as for advanced data storage nanomaterials in harsh environments.

5.6. Acknowledgement

This work was supported by U.S. Department of Energy (DOE) under Contract DE-FC07-08ID14926, by the INL-LDRD administered by CAES under the DOE Contract DE-AC07-05ID14517.

5.7. References

(1) Qiang, Y.; Antony, J.; Sharma, A.; Nutting, J.; Sikes, D.; Meyer, D. Iron/Iron Oxide Core-Shell Nanoclusters for Biomedical Applications. J. Nanoparticle Res. **2006**, 8 (3), 489–496. https://doi.org/10.1007/s11051-005-9011-3.

(2) Laurent, S.; Dutz, S.; Häfeli, U. O.; Mahmoudi, M. Magnetic Fluid Hyperthermia: Focus on Superparamagnetic Iron Oxide Nanoparticles. Adv. Colloid Interface Sci. **2011**, 166 (1), 8–23. https://doi.org/10.1016/j.cis.2011.04.003.

(3) Bautista, M. C.; Bomati-Miguel, O.; Zhao, X.; Morales, M. P.; González-Carreño, T.; Alejo, R. P. de; Ruiz-Cabello, J.; S Veintemillas-Verdaguer. Comparative Study of Ferrofluids Based on Dextran-Coated Iron Oxide and Metal Nanoparticles for Contrast Agents in Magnetic Resonance Imaging. Nanotechnology **2004**, 15 (4), S154. https://doi.org/10.1088/0957-4484/15/4/008.

(4) Zhang, X. X.; Wen, G. H.; Huang, S.; Dai, L.; Gao, R.; Wang, Z. L. Magnetic Properties of Fe Nanoparticles Trapped at the Tips of the Aligned Carbon Nanotubes. J. Magn. Magn. Mater. **2001**, 231 (1), 9–12. https://doi.org/10.1016/S0304-8853(01)00134-2.

(5) Scott, J. H. J.; Majetich, S. A. Morphology, Structure, and Growth of Nanoparticles Produced in a Carbon Arc. Phys. Rev. B **1995**, 52 (17), 12564–12571. https://doi.org/10.1103/PhysRevB.52.12564.

(6) Hu, J.; Chen, G.; Lo, I. M. Removal and Recovery of Cr (VI) from Wastewater by Maghemite Nanoparticles. Water Res. **2005**, 39 (18), 4528–4536.

(7) Hu J, C. G. and L. I. M. Selective Removal of Heavy Metals from Industrial Wastewater Using Maghemite Nanoparticle: Performance and Mechanisms. J Env. Eng **2006**, 132, 709.

(8) Kaur M, Z. H., Martin L, Todd T. and Qiang Y. Conjugates of Magnetic Nanoparticle Actinide Specific Chelator for Radioactive Waste Separation. Env. Sci Technol **2013**, 47, 11942.

(9) Kaur M, J. A., Tian G, Jiang W, Rao L, Paszczynski A. and Qiang Y. Separation Nanotechnology of Diethylenetriaminepentaacetic Acid Bonded Magnetic Nanoparticles for Spent Nuclear Fuel. Nano Energy **2013**, 2, 124.

(10) LAAN, G. P. V. D.; BEENACKERS, A. A. C. M. Kinetics and Selectivity of the Fischer–Tropsch Synthesis: A Literature Review. Catal. Rev. **1999**, 41 (3–4), 255–318. https://doi.org/10.1081/CR-100101170.

(11) Suslick, K. S.; Hyeon, T.; Fang, M. Nanostructured Materials Generated by High-Intensity Ultrasound: Sonochemical Synthesis and Catalytic Studies. Chem. Mater. **1996**, 8 (8), 2172–2179. https://doi.org/10.1021/cm960056l.

(12) Jiang, W.; Sundararajan, J. A.; Varga, T.; Bowden, M. E.; Qiang, Y.; McCloy, J. S.; Henager, Charles. H.; Montgomery, R. O. In Situ Study of Nanostructure and Electrical Resistance of Nanocluster Films Irradiated with Ion Beams. Adv. Funct. Mater. **2014**, 24 (39), 6210–6218. https://doi.org/10.1002/adfm.201400553.

(13) Khanal, L. R.; Williams, T.; Qiang, Y. High-Temperature Investigation on Morphology, Phase and Size of Iron/Iron-Oxide Core-Shell Nanoclusters for Radiation Nanodetector. J. Phys. Appl. Phys. **2018**. https://doi.org/10.1088/1361-6463/aac47e.

(14) Jiang, W.; McCloy, J. S.; Lea, A. S.; Sundararajan, J. A.; Yao, Q.; Qiang, Y. Magnetization and Susceptibility of Ion-Irradiated Granular Magnetite Films. Phys. Rev. B **2011**, 83 (13), 134435.

(15) Allongue, P.; Maroun, F. Electrodeposited Magnetic Layers in the Ultrathin Limit. MRS Bull. **2010**, 35 (10), 761–770. https://doi.org/10.1557/mrs2010.505.

(16) Rusponi, S.; Cren, T.; Weiss, N.; Epple, M.; Buluschek, P.; Claude, L.; Brune, H. The Remarkable Difference between Surface and Step Atoms in the Magnetic Anisotropy of Two-Dimensional Nanostructures. Nat. Mater. **2003**, 2 (8), 546–551. https://doi.org/10.1038/nmat930.

(17) Meyerheim, H. L.; Sander, D.; Popescu, R.; Kirschner, J.; Robach, O.; Ferrer, S. Spin Reorientation and Structural Relaxation of Atomic Layers: Pushing the Limits of Accuracy. Phys. Rev. Lett. **2004**, 93 (15), 156105. https://doi.org/10.1103/PhysRevLett.93.156105.

(18) Kaur, M.; McCloy, J. S.; Jiang, W.; Yao, Q.; Qiang, Y. Size Dependence of Inter- and Intracluster Interactions in Core–Shell Iron–Iron Oxide Nanoclusters. J. Phys. Chem. C **2012**, 116 (23), 12875–12885. https://doi.org/10.1021/jp301453w.

(19) Wang, C. M.; Baer, D. R.; Amonette, J. E.; Engelhard, M. H.; Qiang, Y.; Antony, J. Morphology and Oxide Shell Structure of Iron Nanoparticles Grown by Sputter-Gas-Aggregation. Nanotechnology **2007**, 18 (25), 255603. https://doi.org/10.1088/0957-4484/18/25/255603.

(20) P. Schwaminger, S.; Bauer, D.; Fraga-García, P.; E. Wagner, F.; Berensmeier, S. Oxidation of Magnetite Nanoparticles: Impact on Surface and Crystal Properties. CrystEngComm **2017**, 19 (2), 246–255. https://doi.org/10.1039/C6CE02421A.

(21) Nie, S.; Starodub, E.; Monti, M.; Siegel, D. A.; Vergara, L.; El Gabaly, F.; Bartelt, N. C.; de la Figuera, J.; McCarty, K. F. Insight into Magnetite's Redox Catalysis from Observing Surface Morphology during Oxidation. J. Am. Chem. Soc. **2013**, 135 (27), 10091–10098. https://doi.org/10.1021/ja402599t.

(22) Krajewski, M.; Brzózka, K.; Górka, B.; Lin, W.-S.; Lin, H.-M.; Szumiata, T.; Gawroński, M.; Wasik, D. The Influence of Thermal Annealing on Structure and Oxidation of Iron Nanowires. Nukleonika **2015**, 60 (1), 87–91. https://doi.org/10.1515/nuka-2015-0004.

(23) Krajewski, M.; Brzozka, K.; S. Lin, W.; M. Lin, H.; Tokarczyk, M.; Borysiuk, J.; Kowalski, G.; Wasik, D. High Temperature Oxidation of Iron–Iron Oxide Core–Shell Nanowires Composed of Iron Nanoparticles. Phys. Chem. Chem. Phys. **2016**, 18 (5), 3900–3909. https://doi.org/10.1039/C5CP07569F.

(24) Cornell R M and Schwertmann U. Iron Oxides Struct. Prop. React. Occur. Uses **2003**.

(25) Saleem, M.; Al-Kuhaili, M. F.; Durrani, S. M. A.; Bakhtiari, I. A. Characterization of Nanocrystalline α -Fe 2 O 3 Thin Films Grown by Reactive Evaporation and Oxidation of Iron. Phys. Scr. **2012**, 85 (5), 055802. https://doi.org/10.1088/0031-8949/85/05/055802.

(26) Lehlooh, A.-F.; Mahmood, S.; Abu-Aljarayesh, I. Mössbauer and X-Ray Diffraction Studies of Heat-Treated Fe3O4 Fine Particles. J. Magn. Magn. Mater. **1994**, 136 (1), 143–148. https://doi.org/10.1016/0304-8853(94)90458-8.

(27) Liang, R.; Yang, S.; Yan, F.; He, J. Kinetics of Oxidation Reaction for Magnetite Pellets. J. Iron Steel Res. Int. **2013**, 20 (9), 16–20. https://doi.org/10.1016/S1006-706X(13)60150-8.

(28) Ratke, L.; Voorhees, P. W. Growth and Coarsening; Engineering Materials; Springer Berlin Heidelberg: Berlin, Heidelberg, 2002. https://doi.org/10.1007/978-3-662-04884-9.

(29) Marqusee, J. A.; Ross, J. Theory of Ostwald Ripening: Competitive Growth and Its Dependence on Volume Fraction. J. Chem. Phys. **1984**, 80 (1), 536–543. https://doi.org/10.1063/1.446427.

(30) Lee S Y, M. N., Nguyen N, Sun Y. M. and White J. M. Copper Oxide Reduction through Vacuum Annealing. Appl Surf Sci **2003**, 206, 102.

(31) Poulston, S.; Rowbotham, E.; Stone, P.; Parlett, P.; Bowker, M. Temperature-Programmed Desorption Studies of Methanol and Formic Acid Decomposition on Copper Oxide Surfaces. Catal. Lett. **1998**, 52 (1), 63–67. https://doi.org/10.1023/A:1019007100649.

(32) Cullity B D and Weymouth J W. Elements of X-Ray Diffraction. Am J Phys **1957**, 25, 394.

(33) Ahmadzadeh, M.; Romero, C.; McCloy, J. Magnetic Analysis of Commercial Hematite, Magnetite, and Their Mixtures. AIP Adv. **2017**, 8 (5), 056807. https://doi.org/10.1063/1.5006474.

(34) Krajewski, M.; Brzozka, K.; Tokarczyk, M.; Kowalski, G.; Lewinska, S.; Slawska-Waniewska, A.; Lin, W. S.; Lin, H. M. Impact of Thermal Oxidation on Chemical Composition and Magnetic Properties of Iron Nanoparticles. J. Magn. Magn. Mater. **2018**, 458, 346–354. https://doi.org/10.1016/j.jmmm.2018.03.047.

(35) Tomou, A.; Panagiotopoulos, I.; Gournis, D.; Kooi, B. L10 Ordering and Magnetic Interactions in FePt Nanoparticles Embedded in MgO and SiO2 Shell Matrices. J. Appl. Phys. **2007**, 102 (2), 023910. https://doi.org/10.1063/1.2752141.

(36) Klemmer, T. J.; Liu, C.; Shukla, N.; Wu, X. W.; Weller, D.; Tanase, M.; Laughlin, D. E.; Soffa, W. A. Combined Reactions Associated with L10 Ordering. J. Magn. Magn. Mater. **2003**, 266 (1), 79–87. https://doi.org/10.1016/S0304-8853(03)00458-X.

(37) Roberts, A. P.; Cui, Y.; Verosub, K. L. Wasp-Waisted Hysteresis Loops: Mineral Magnetic Characteristics and Discrimination of Components in Mixed Magnetic Systems. J. Geophys. Res. Solid Earth **1995**, 100 (B9), 17909–17924. https://doi.org/10.1029/95JB00672.

(38) Parry, L. G. Shape-Related Factors in the Magnetization of Immobilized Magnetite Particles. Phys. Earth Planet. Inter. **1980**, 22 (2), 144–154. https://doi.org/10.1016/0031-9201(80)90055-2.

(39) Bercoff, P. G.; Bertorello, H. R. Magnetic Properties of Hematite with Large Coercivity. Appl. Phys. A **2010**, 100 (4), 1019–1027. https://doi.org/10.1007/s00339-010-5983-7.

(40) Rath, C.; Sahu, K. K.; Kulkarni, S. D.; Anand, S.; Date, S. K.; Das, R. P.; Mishra, N. C. Microstructure-Dependent Coercivity in Monodispersed Hematite Particles. Appl. Phys. Lett. **1999**, 75 (26), 4171–4173. https://doi.org/10.1063/1.125572.

(41) Sahu, K. K.; Rath, C.; Mishra, N. C.; Anand, S.; Das, R. P. Microstructural and Magnetic Studies on Hydrothermally Prepared Hematite. J. Colloid Interface Sci. **1997**, 185 (2), 402–410. https://doi.org/10.1006/jcis.1996.4525.

(42) Abraime, B.; Mahmoud, A.; Boschini, F.; Ait Tamerd, M.; Benyoussef, A.; Hamedoun, M.; Xiao, Y.; El Kenz, A.; Mounkachi, O. Tunable Maximum Energy Product in CoFe2O4 Nanopowder for Permanent Magnet Application. J. Magn. Magn. Mater. **2018**, 467, 129–134. https://doi.org/10.1016/j.jmmm.2018.07.063.

(43) Coey, J. M. D. Hard Magnetic Materials: A Perspective. IEEE Trans. Magn. **2011**, 47 (12), 4671–4681. https://doi.org/10.1109/TMAG.2011.2166975.

(44) Skomski, R.; Coey, J. M. D. Magnetic Anisotropy — How Much Is Enough for a Permanent Magnet? Scr. Mater. **2016**, 112, 3–8. https://doi.org/10.1016/j.scriptamat.2015.09.021.

Project 2: Advanced Magnetic Nanomaterials for Application of Ultrahigh Frequency Electronics

Chapter 6: Soft Magnetic Films

6.1. Introduction

Materials that can be easily magnetized and demagnetized are known as soft magnetic materials. The term "soft" refers to the classification employed as a function of coercive field H_C, the magnetic field needed to demagnetize completely a ferro/ferri magnetic material. The threshold magnetic field for a magnetic material to characterize as a soft magnetic material is $H_C \leq 10\ Oe$.[1] Soft magnetic materials are used to improves and/or channel the flux produced by an electric current. Relative permeability ($\mu_r, where\ \mu_r = B/\mu_o H$) is the main parameter to determine the measure of how readily the material responds to the applied field. Other parameters of interest are the coercivity, the saturation magnetization and electrical conductivity.

Over the past several decades, soft magnetic films have been intriguing research topics for applications in magnetic devices including transformers, inductors, inductive devices, magnetic write/read head and magnetic recording media. The increasing interest on soft magnetic films include (i) higher combined induction and permeabilities, and (ii) high temperature operable magnets, as well as many non-magnetic material issues such as mechanical properties, corrosion resistance, etc. However, the primary challenge in achieving such goals include film chemistry, structure, and essentially the ability to tune microstructural features.

It is crucial that the films used in soft magnetic applications must be improved in terms of their intrinsic and extrinsic magnetic properties. Here, the intrinsic properties means microstructure insensitive properties but depend on alloy chemistry and crystal structure, such as saturation magnetization, Curie temperature (temperature above which the material lose their permanent magnetic properties), the saturation magnetic induction, magnetocrystalline anisotropy (property of a ferromagnetic material which takes more energy to magnetize in a certain direction), and the magnetostrictive coefficients (fractional change in length as the magnetization increases from zero to

its saturation value). In a broader sense, magnetic anisotropy and magnetostriction can be considered as extrinsic for a two-phase material as they depend on microstructures. Magnetocrystalline anisotropy and magnetostriction, which are determining factors in which the magnetization vector can be rotated into the direction of the applied field, are also sensitively depend on the alloy chemistry. Many important soft magnetic alloy systems have zero crossings of the magnetocrystalline anisotropy, or magnetostriction coefficients which can be utilized in the development of premiere soft magnet materials. There has been a numerous work on the variation of intrinsic magnetic properties with alloy chemistry.[1,2] However, new discoveries have been continued in this area. It can be safely stated that more wide-open area in the development of soft magnetic materials for applications is the fundamental understanding and exploitation of microstructure's influence on the extrinsic magnetic properties. Important microstructural features include grain size, shape and orientation, defect concentrations, compositional inhomogeneities, magnetic domains and domain walls. The interaction of magnetic domain walls with microstructural hindrances to their motion is of particular importance to the understanding of soft magnetic properties. The important extrinsic magnetic properties in soft magnetic materials include the magnetic permeability and the coercivity, which typically have an inverse relationship. Remnant magnetization, squareness of the hysteresis loop and magnetic anisotropy (crystalline, shape or stress related) are also important in determining magnetic softness.[3,4]

The technical properties of interest for soft magnetic materials are as follows (see figure below):

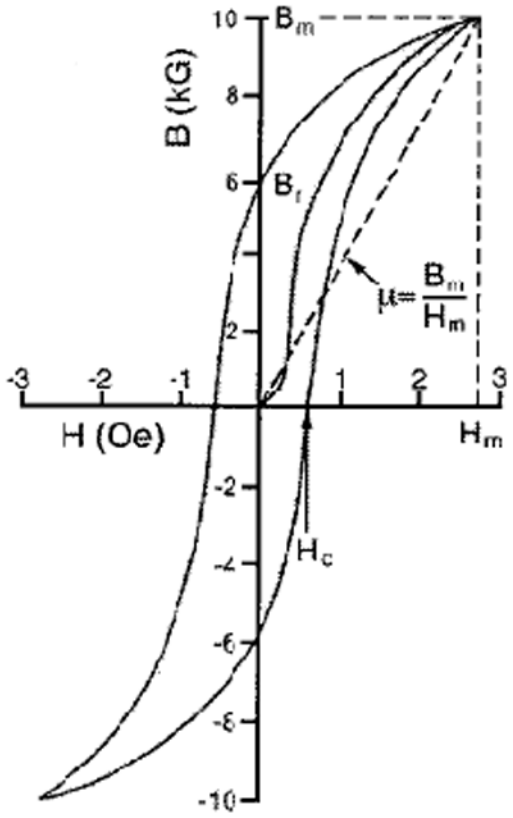

Figure 6.1 Schematic of a hysteresis curve for a soft magnetic material defining some technical magnetic parameters.

1. High permeability: Permeability, $\mu = B/H = (1 + \chi)$ is the material's parameter which determines the magnetic flux density, B, that a material possess in response of a given applied field, H. In high permeability materials, we can produce very large changes in magnetic flux density in very small fields.

2. Low hysteresis loss: Hysteresis loss is the energy consumed during the reversal of magnetization of a material between a field H and $-H$. The energy consumed in one cycle is $W_h = \oint MdB$ or the area covered by the hysteresis loop. The power loss of an AC device can be found by multiplying frequency by the hysteretic loss in one cycle. In addition, at high frequencies, eddy current losses are prominent that are determined by the material's resistivity, ρ. Magnetic hysteresis is a useful attribute

of a permanent magnet material in which we wish to store a large metastable magnetization. On the other hand, soft magnets large class of applications requires small hysteresis losses per cycle for a large class of applications. These include inductors, low and high frequency transformers, alternating current machines, motors, generators and magnetic amplifiers.

3. Large saturation and remnant magnetizations: A large saturation magnetization, M_S, and induction, B_S, are required for the soft magnetic applications.

4. Low coercivity: Coercivity is ability of a magnetic material to resist an applied magnetic field without demagnetizing. Soft magnetic films should have as low coercivity as possible to enhance magnetic switching capability and reduce the hysteresis loss.

5. High in-plane uniaxial anisotropy: Anisotropy refers to the direction dependent magnetic property of a material. Soft magnetic materials are recognized as the best material if they possess high tunable uniaxial anisotropy.

5. High Curie temperature: The ability to use soft magnetic materials at elevated temperatures is closely dependent on the Curie temperature or magnetic ordering temperature of the material.

6.2. Nanocrystalline Soft Magnetic Films

The term “nanocrystalline” refers to those films that have majority of grain sizes in the typical range from 1 to 100 nm. Recently, nanocrystalline soft magnetic films have gained tremendous attention as the benefits of these films arise from their chemical and structural variations on a nanoscale which are important for tailoring excellent magnetic properties. Generally, soft ferromagnetic properties can be enhanced by tailoring the chemistry and microstructures. Advantages in tailoring the microstructures is due to the fact that a measure of the magnetic hardness (the coercivity, H_C) is roughly inversely proportional to the grain size (D) for grain sizes lying between 100 nm –1μm (where the grain size exceeds the domain (Bloch) wall thickness,dW). In such cases, grain

boundaries obstruct the domain wall motion, which makes fine-grained materials magnetically harder than large grain one. Recent developments in the study of magnetic coercivity mechanisms have shown that for the grain size, $D < 100\ nm,\ H_C$ decreases rapidly with decreasing grain size.[5,6] This can be understood by the fact that the domain wall with thickness dW exceeds the grain size so that fluctuations in magnetic anisotropy on the grain size length scale are irrelevant to domain wall pinning. This characteristic indicates that nanocrystalline films have excellent potential as soft magnetic materials. Softness requires that nano-grains should be exchange coupled. Therefore, the processing of soft magnetic films must yield very refined microstructures in which the magnetic nanoparticles end up with exchange coupling.

Nanocrystalline soft magnetic alloy films can be described in general as $TL_{1-x}(TE,M,NM)_x$ where TL denotes a late (ferromagnetic) transition metal element, TE is an early transition metal element, M is a metalloid, and NM is a noble metal. This composition usually has $x < 0.20$ i.e. with as much late ferromagnetic transition metals (TL of Co, Ni, or Fe) as possible.[2] The remaining early transition metals (TE = Zr, Nb, Hf, Ta, etc.) and metalloids (M = B, P, Si, etc.) are added to promote glass formation in the precursor. The noble metal elements (TN = Cu, Ag, Au, etc.) serve as nucleating agents for the ferromagnetic nanocrystalline phase. These alloys may be single phase (Type I) but are generally two-phase materials with a nanocrystalline ferromagnetic phase and a residual amorphous phase at the grain boundaries (Type II). The Type II nanocrystalline alloys might have general properties (1) relatively high resistivity (50 –80 mΩ cm), (2) low magnetocrystalline anisotropy, and (3) increased mechanical strength. These properties make the nanocrystalline alloys as excellent soft magnetic films. Fe–M–B–Cu (M = Zr, Nb, Hf) nanocrystalline alloy films have all been optimized to achieve small magnetostrictive coefficients as well as large permeabilities.[7] More recently (Fe,Co)–M–B–Cu (M = Nb, Hf, or Zr) nanocrystalline alloys, called HITPERM have shown attractive magnetic field inductions (1.6–2.1 T) accompanied by high permeabilities and high Curie temperatures.[2]

6.3. Soft Magnetic Films for High Frequency Applications

Most recently, rapid improvement and miniaturization have been in progress in electronic equipment. One of the key devices for miniaturization of small-sized electronic apparatuses, such as the portable communication tools or portable audio systems, is the magnetic components**.** For that aim, development of micromagnetic devices using thin-film inductors or transformers operating at high frequency range is very important. In order to realize those improvements in magnetic devices and parts, soft magnetic films with excellent frequency characteristics are strongly required as their core materials. To produce a soft magnetic thin film with excellent response, the film must have not only high electrical resistivity, but also large saturation magnetization and appropriate in-plane uniaxial anisotropy field.

Over the past few decades, the metal/insulator nanocomposite soft magnetic films have gained considerable attention. Nanocomposite metal/insulator granular films like Fe-M-O[8,9] and Fe-M-N[10,11] (M=Al, Hf, Ta, Si etc.) have demonstrated excellent soft magnetic properties for their potential high frequency application. Soft magnetic films are critical for integration of passive components (inductors and transformers, etc.) onto silicon microchip, which is a major challenge in the urgent move towards miniaturization and improvement of next-generation microelectronic devices working in the radio frequency (RF) range.[12,13] Due to the magnetic flux amplification, chip area can be reduced by eliminating unnecessary interconnects.[12] This would allow for on-chip power conditioning and efficient power delivery in electronic systems.[13,14] For the gigahertz frequency application, soft magnetic properties include large M_S, small H_C, and high μ, to increase the magnetic reversal capacity.[15] Moreover, the electrical resistivity (ρ) should be sufficiently large to suppress eddy current loss[16], which results in the ferromagnetic resonance (FMR) to be shifted towards higher frequencies. According to the FMR theory, tunable in-plane uniaxial anisotropy (H_K) is also among the most desirable characteristics to balance the high μ, and the large FMR frequency (f_{FMR}). Moreover, it is crucial that the fabrication of such films must be compatible with Si-based integration, where a

restricted processing temperature is required to incorporate the underlying integrated circuits.[17] However, it is only when the ferromagnetic metal approaches the percolation volume fraction that the magnetic softness is obtained in these Fe-M-O and Fe-M-N soft magnetic nanocomposites, which severely deteriorates the resistivity. In particular, high-temperature magnetic post-annealing is usually necessary to induce in-plane uniaxial anisotropy in these nanocomposite films,[9] which is apparently incompatible with the Si integrated designs for high frequency applications.

Nanocomposite soft magnetic films assembled by Fe/Fe_3O_4 core-shell nanoparticles[18–22] may be the most suitable candidate for the desired high-frequency magnetic properties, via combining the high M_S[18] of Fe core with the high ρ from both the semiconductive Fe_3O_4 shell and the nanoparticle stacking. Moreover, the magnetic native Fe_3O_4 acts as a medium for exchange coupling between the Fe nanoparticles[23] and could thus strengthen the magnetic softness beyond the metal/non-magnetic insulator granular films.[24,25] For materials vulnerable to high-temperature processes, the negatively charged nanocomposite can be accelerated to energetic nanoparticle impact by applying positive bias voltage onto the substrate. As a result, the shapes of the deposited nanoparticles can be changed from original spheroids to a general ellipsoid, which is expected at room temperature to induce in-plane uniaxial anisotropy in the nanocomposites assembled by the Fe/Fe_3O_4 core-shell nanoparticles. This assessment will help us to obtain good and adjustable uniaxial anisotropy and magnetic softness with the large resistivities. The excellent anisotropy, saturation magnetization and resistivity could produce high-frequency performance in miniaturized electronic devices.

6.4. Research Scope and Limitations

Wireless communication has been rapidly progressing towards commercialization of 5G and development of 6G. Since the frequency spectrum of 5G and 6G ranges from few hundred megahertz to tens gigahertz (GHz), development of ultrahigh frequency compatible magnetic nanomaterials is critical. Further, the rise of internet of things, and demands for lighter, faster, and smarter devices that

incorporate computing, communication, and sensing functionalities in highly miniaturized packages, integration of thin film magnetic core that has high saturation magnetization, uniaxial anisotropy, and high resistivity on an electronic circuit is very important.

Owing to the increasing demands of soft magnetic nanocomposite for their potential applications as GHZ compatible materials in miniaturized electronic devices, this research mainly focuses on the development of soft magnetic nanocomposite from energetic Fe/Fe_3O_4 nanoparticle impact and investigate their structure-property relationships. The research mainly based on the hypothesis that, "Nanocomposite soft magnetic films assembled by energetic Fe/Fe_3O_4 nanoparticles impact could help us to create excellent uniaxial anisotropy, and contribute to the development of the high frequency soft magnetic materials for next generation wireless network." This project will address issues or challenges as listed below by specifically

studying the magnetic, electric and structural properties based on the nanoparticles' impact energy onto silicon subtrates.

- Research of soft magnetic nanoparticles for high frequency application is still in their infancy.
- Nanoparticles behavior under bias voltages have not been understood.
- Bringing controlled uniaxial anisotropy property is a big challenge
- Developing soft magnetic material for GHz application at room temperature is almost impossible.

The objective of this research is to understand the structural, magnetic and electrical property changes of the soft magnetic nanocomposite films with the applied bias voltages on the silicon substrate at room temperature, in general, and to develop fundamental understanding of biased voltage based modification in the properties of the soft magnetic granular films and composites of iron and iron oxides, in particular.

- To tailor in-plane uniaxial anisotropy on the soft magnetic nanocomposite films assembled by energetic Fe/Fe_3O_4 nanoparticle impact.
- To develop a fundamental understanding of the bias-voltage-based modification and the technique of bringing controlled property changes in the soft magnetic nanocomposite films.
- To study the structural, magnetic and electrical property changes in nanomaterials under different bias voltages.
- To assess the stability of nanocomposite for obtaining excellent softness for high frequency application.

The results obtained from this investigation could be useful in the future to generate data for scientific assessments in prediction of the material performance for high frequency electronics and to recommend candidate composition for development of novel multifunctional materials. This research investigates several classes of magnetic materials (spherical magnetic nanoparticles to ellipsoidal soft magnetic nanocomposite films) as a high frequency soft magnetic films and elucidates mechanism for susceptibility of bias-voltage-based property changes. This research will possibly be able to answer some of the following specific scientific questions: How do particle shapes, density, and roughness change by energetic nanoparticle impact? What are the factors affecting the change in soft magnetic properties of a nanocomposite? What makes the nanocomposite to induce in-plane uniaxial anisotropy? These questions and more will be addressed by studying in detail from the experimental data obtained using Grazing-angle Incident X-ray diffraction (GIXRD), Vibrating Sample Magnetometer (VSM), Scanning Electron Microscope (SEM), Atomic Force Microscope (AFM), Four -probe Electrical conductivity Measurement Tool, and Network Analyzer. As mentioned before this research is ultimately focused on understanding the structural changes, variation in magnetic behavior and tailoring in-plane uniaxial anisotropy based on impact energy of nanoparticles.

6.5. References

(1) Périgo, E. A.; Weidenfeller, B.; Kollár, P.; Füzer, J. Past, Present, and Future of Soft Magnetic Composites. *Applied Physics Reviews* **2018**, *5* (3), 031301. https://doi.org/10.1063/1.5027045.

(2) McHenry, M. E.; Willard, M. A.; Laughlin, D. E. Amorphous and Nanocrystalline Materials for Applications as Soft Magnets. *Progress in Materials Science* **1999**, *44* (4), 291–433. https://doi.org/10.1016/S0079-6425(99)00002-X.

(3) Bozorth, R. M. *Ferromagnetism*; The Bell Telephone Laboratories series; Van Nostrand: New York, 1951.

(4) Cullity, B. D. *Introduction to Magnetic Materials*; Addison-Wesley Pub. Co.: Reading, Mass., 1972.

(5) Herzer, G. Grain Size Dependence of Coercivity and Permeability in Nanocrystalline Ferromagnets. *IEEE Transactions on Magnetics* **1990**, *26* (5), 1397–1402.

(6) Herzer, G. Grain Structure and Magnetism of Nanocrystalline Ferromagnets. *IEEE Transactions on Magnetics* **1989**, *25* (5), 3327–3329.

(7) Makino, A.; Inoue, A.; Masumoto, T. Nanocrystalline Soft Magnetic Fe–M–B (M=Zr, Hf, Nb) Alloys Produced by Crystallization of Amorphous Phase (<I>Overview</I>). *Materials Transactions, JIM* **1995**, *36* (7), 924–938. https://doi.org/10.2320/matertrans1989.36.924.

(8) Ha, N. D.; Phan, M.-H.; Kim, C. O. Novel Nanostructure and Magnetic Properties of Co–Fe–Hf–O Films. *Nanotechnology* **2007**, *18* (15), 155705. https://doi.org/10.1088/0957-4484/18/15/155705.

(9) Hayakawa, Y.; Makino, A.; Fujimori, H.; Inoue, A. High Resistive Nanocrystalline Fe-M-O (M=Hf, Zr, Rare-Earth Metals) Soft Magnetic Films for High-Frequency Applications (Invited). *Journal of Applied Physics* **1997**, *81* (8), 3747–3752. https://doi.org/10.1063/1.365498.

(10) Liu, Z. W.; Liu, Y.; Yan, L.; Tan, C. Y.; Ong, C. K. Thickness-Dependent Properties of FeTaN Thin Films Deposited on Flexible Substrate. *Journal of Applied Physics* **2006**, *99* (4), 043903. https://doi.org/10.1063/1.2170588.

(11) Viala, B.; Minor, M. K.; Barnard, J. A. Microstructure and Magnetism in FeTaN Films Deposited in the Nanocrystalline State. *Journal of Applied Physics* **1996**, *80* (7), 3941–3956. https://doi.org/10.1063/1.363352.

(12) Korenivski, V. GHz Magnetic Film Inductors. *Journal of Magnetism and Magnetic Materials* **2000**, *215–216*, 800–806. https://doi.org/10.1016/S0304-8853(00)00292-4.

(13) Seemann, K.; Leiste, H.; Ziebert, C. Soft Magnetic FeCoTaN Film Cores for New High-Frequency CMOS Compatible Micro-Inductors. *Journal of Magnetism and Magnetic Materials* **2007**, *316* (2), e879–e882. https://doi.org/10.1016/j.jmmm.2007.03.126.

(14) Gardner, D. S.; Schrom, G.; Hazucha, P.; Paillet, F.; Karnik, T.; Borkar, S.; Saulters, J.; Owens, J.; Wetzel, J. Integrated On-Chip Inductors with Magnetic Films. In *2006 International Electron Devices Meeting*; 2006; pp 1–4. https://doi.org/10.1109/IEDM.2006.347002.

(15) Ohnuma, S.; Fujimori, H.; Masumoto, T.; Xiong, X. Y.; Ping, D. H.; Hono, K. FeCo–Zr–O Nanogranular Soft-Magnetic Thin Films with a High Magnetic Flux Density. *Appl. Phys. Lett.* **2003**, *82* (6), 946–948. https://doi.org/10.1063/1.1537456.

(16) Beach, G. S. D.; Berkowitz, A. E.; Parker, F. T.; Smith, D. J. Magnetically Soft, High-Moment, High-Resistivity Thin Films Using Discontinuous Metal/Native Oxide Multilayers. *Appl. Phys. Lett.* **2001**, *79* (2), 224–226. https://doi.org/10.1063/1.1383998.

(17) Jin, S.; Zhu, W.; van Dover, R. B.; Tiefel, T. H.; Korenivski, V.; Chen, L. H. High Frequency Properties of Fe–Cr–Ta–N Soft Magnetic Films. *Appl. Phys. Lett.* **1997**, *70* (23), 3161–3163. https://doi.org/10.1063/1.119120.

(18) Qiang, Y.; Antony, J.; Sharma, A.; Nutting, J.; Sikes, D.; Meyer, D. Iron/Iron Oxide Core-Shell Nanoclusters for Biomedical Applications. *J Nanopart Res* **2006**, *8* (3), 489–496. https://doi.org/10.1007/s11051-005-9011-3.

(19) Wang, C. M.; Baer, D. R.; Thomas, L. E.; Amonette, J. E.; Antony, J.; Qiang, Y.; Duscher, G. Void Formation during Early Stages of Passivation: Initial Oxidation of Iron Nanoparticles at Room Temperature. *Journal of Applied Physics* **2005**, *98* (9), 094308. https://doi.org/10.1063/1.2130890.

(20) Wang, C.; Baer, D. R.; Amonette, J. E.; Engelhard, M. H.; Antony, J.; Qiang, Y. Morphology and Electronic Structure of the Oxide Shell on the Surface of Iron Nanoparticles. *J. Am. Chem. Soc.* **2009**, *131* (25), 8824–8832. https://doi.org/10.1021/ja900353f.

(21) Peng, D. L.; Hihara, T.; Sumiyama, K.; Morikawa, H. Structural and Magnetic Characteristics of Monodispersed Fe and Oxide-Coated Fe Cluster Assemblies. *Journal of Applied Physics* **2002**, *92* (6), 3075–3083. https://doi.org/10.1063/1.1501754.

(22) Khanal, L. R.; Williams, T.; Qiang, Y. High-Temperature Investigation on Morphology, Phase and Size of Iron/Iron-Oxide Core–Shell Nanoclusters for Radiation Nanodetector. *J. Phys. D: Appl. Phys.* **2018**, *51* (25), 255302. https://doi.org/10.1088/1361-6463/aac47e.

(23) Herzer, G. Grain Size Dependence of Coercivity and Permeability in Nanocrystalline Ferromagnets. *IEEE Transactions on Magnetics* **1990**, *26* (5), 1397–1402. https://doi.org/10.1109/20.104389.

(24) Hayakawa, Y.; Makino, A.; Fujimori, H.; Inoue, A. High Resistive Nanocrystalline Fe-M-O (M=Hf, Zr, Rare-Earth Metals) Soft Magnetic Films for High-Frequency Applications (Invited). *Journal of Applied Physics* **1997**, *81* (8), 3747–3752. https://doi.org/10.1063/1.365498.

(25) Ha, N. D.; Phan, M.-H.; Kim, C. O. Novel Nanostructure and Magnetic Properties of Co–Fe–Hf–O Films. *Nanotechnology* **2007**, *18* (15), 155705. https://doi.org/10.1088/0957-4484/18/15/155705.

(26) Haberland, H.; Karrais, M.; Mall, M.; Thurner, Y. Thin Films from Energetic Cluster Impact: A Feasibility Study. *Journal of Vacuum Science & Technology A* **1992**, *10* (5), 3266–3271. https://doi.org/10.1116/1.577853.

(27) Moseler, M.; Rattunde, O.; Nordiek, J.; Haberland, H. On the Origin of Surface Smoothing by Energetic Cluster Impact: Molecular Dynamics Simulation and Mesoscopic Modeling. *Nuclear Instruments and Methods in Physics Research Section B: Beam Interactions with Materials and Atoms* **2000**, *164–165*, 522–536. https://doi.org/10.1016/S0168-583X(99)01081-2.

Chapter 7: Soft Magnetic Nanocomposites Assembled by Energetic Fe/Fe_3O_4 Nanoparticles at Room Temperature for 5G and 6G Wireless Communication

7.1. Abstract

A new CMOS-integration compatible soft magnet is developed by applying the energetic impact of Fe/Fe_3O_4 core-shell nanoparticles onto tilted Si substrates. At room temperature, the in-plane uniaxial anisotropy is induced and tuned, which is interpreted by the uniaxial shape anisotropy of the ellipsoidal nanoparticles and the nanoparticle assembly alignment. Meanwhile, excellent magnetic softness and large resistivity are obtained in the nanocomposites. The most desirable properties of the samples are achieved at the potential of 5 kV, with in-plane anisotropy field larger than 13.5 kOe, saturation magnetization of 183.3 emu/g and electrical resistivity of 123 μΩ·cm. This shifts the ferromagnetic resonance frequency beyond 8.5 GHz. The adjustment of the permeability spectra with the large magnetic flux is demonstrated in the Fe/Fe_3O_4 nanocomposites, which hold prospects for controllable ultrahigh-frequency applications (such as 5G and 6G wireless communication) in next-generation microelectronic devices.

7.2. Introduction

Wireless communication has been rapidly progressing towards the commercialization of 5G in 2020[1], and development of 6G in next 10 years. Since the frequency spectrum of 5G and 6G ranges from a few hundred megahertz to tens gigahertz, the development of ultrahigh frequency compatible materials is critical. Also, because of the rise of the Internet of Things (IoT), and demands for lighter, faster and smarter devices that incorporate computing, communication, and sensing functionalities in highly miniaturized packages, integration of thin film soft magnetic cores with high saturation magnetization, uniaxial anisotropy, and high resistivity on an electronic circuit is very important.[2]

Magnetic flux amplification of soft magnetic core can reduce chip area by eliminating unnecessary interconnects,[3] allowing for on-chip power conditioning and efficient power delivery in

electronic systems.[4,5] To shift the working frequency towards gigahertz, the films should possess high permeability (μ) and high ferromagnetic resonance frequency (f_{FMR}), which requires large saturation magnetization (M_S).[5–7] Further, small coercivity (H_c) and large electrical resistivity (ρ) are required to suppress magnetic hysteresis loss and eddy current loss, respectively.[8,9] The tunable in-plane uniaxial anisotropy (H_K) is necessary to balance the large f_{FMR} and the high μ, since the $H_K$increment enhances the f_{FMR} but weakens the μ.[3,10–12] Moreover, such magnetically anisotropic films must be compatible with CMOS-based integration. However, a restricted processing temperature is required to incorporate the underlying integrated circuits.[3,13] Nevertheless, few Si-process compatible soft magnets with the desired dynamic performance are readily available.[3,14] Due to small resistivity and the high-temperature annealing needed for nanocrystallization, soft magnetic films based on permalloys[15] and iron-rich Fe-Zr, Fe-Ta, Fe-Hf metal alloys.[16,17] are inappropriate for gigahertz applications. Recently, metal/insulator granular films like Fe-M-O[18–22] and Fe-M-N[23–25] (M=Al, Hf, Ta, Si etc.) have demonstrated intriguing high-frequency magnetic properties. Magnetic softness is obtained when Fe volume fractions approach the percolation, but severely deteriorates the resistivity.[8,20] In particular, high-temperature magnetic post-annealing is necessary to induce in-plane uniaxial anisotropy in these nanocomposite films,[18,26–28] which is incompatible with the Si-integrated designs.

In this work, we have developed nanocomposite soft magnetic films assembled by energetic impact of Fe/Fe_3O_4 core-shell nanoparticles[29–33] on the surface of a tilted silicon substrate at room temperature (RT). Such nanocomposite may provide the desired high-frequency magnetic properties, via combining the high M_S[29] of Fe core with the high ρ from both the semiconductive Fe_3O_4 shell and the nanoparticle stacking. The magnetic native Fe_3O_4 acts as a medium for exchange coupling between Fe nanoparticles[34] and could thus strengthen the magnetic softness beyond the metal/non-magnetic insulator granular films.[18–20,23–25] For obtaining the soft magnetic nanomaterials, materials vulnerable to high-temperature processes, a process of energetic nanoparticle impact (ENI) has been

developed that is the nanoparticles have been ionized in afterglow of discharge and then accelerated to impinge onto a tilted substrate by variable high voltage electric fields up to 10 kV.[35] Theoretical simulation has predicted that the collision can prompt a downhill mass displacement[36]. Hereby, the shapes of impact nanoparticles change from original spheroids to general hemi-ellipsoids, which is expected to induce in-plane uniaxial anisotropy in the nanocomposites. The systematic study on the nanocomposites have shown good and adjustable uniaxial anisotropy and magnetic softness with large resistivities, demonstrating excellent potential for high frequency performance in miniaturized electronic devices for 5G and 6G wireless communications.

7.3. Experimental Details

7.3.1. Sample Fabrication

The nanocomposite Fe/Fe_3O_4 nanoparticle films were synthesized at RT by energetically impacting Fe/Fe_3O_4 nanoparticles onto oblique (110) Si substrates, using a third-generation nanoparticel source that combines magnetron sputtering with gas-aggregation techniques.[29,33,35,36] The monodispersed Fe nanoparticles were firstly generated in an aggregation chamber from the Fe atoms by sputtering from a 3-inch Fe target with a power of 200 W. The atoms were then collided with a mixed flow of Ar (400 sccm) and He (90 sccm) gas atoms. Meanwhile, the aggregation chamber was cooled down to -7 ^oC by circulating ethylene glycol. Due to the high density of ions and electrons in the plasma, ～40% and ～30% of the Fe nanoparticles were negatively and positively charged, respectively.[35,37] The Fe nanoparticle ions were then driven by the differential pumping to pass through the reaction chamber, where a constant flow of 10 sccm O_2 was introduced to form Fe/Fe_3O_4 core-shell nanoparticles. The negatively charged Fe/Fe_3O_4 nanoparticles were then accelerated by an electric field to impinge onto the tilted Si substrate, to which potentials from 0 to 10 kV were applied. The substrate was held at 30^o with respect to the incident particle beam. The positive bias voltage was selected to prevent the implantation of rare gas ions (Ar^+) into the nanocomposites and repel the

positively charged nanoparticles, with the neutral ones softly landing on the substrate holder.[37] Before the nanocomposites deposition, all the chambers were evacuated to background pressures better than 1×10^{-7} Torr.

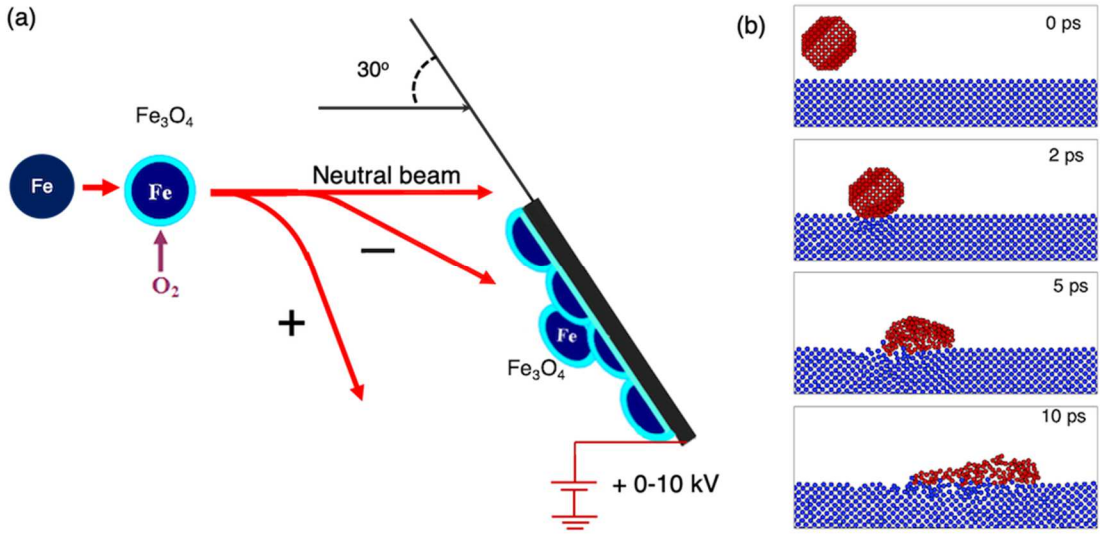

Figure 7.1(a) schematic representation of the synthesis process for the Fe/Fe_3O_4 core-shell nanoparticle-assembled nanocomposite, and (b) snapshots from molecular dynamics simulation of energetic Fe nanoparticle impact on Si, clearly showing the evolution of the hemi-ellipsoidal nanocomposite from the spherical one.

Figure 7.1(a) represents a schematic of the experiment to show the formation of the hemi-ellipsoidal nanoparticle from a spherical nanoparticle. During the aggregation process approximately 40 % and 30 % of nanoparticles pick up negative and positive charge respectively due to the electron and ions in the plasma inside the aggregation chamber.[37] The negatively charged nanoparticles are then directed towards positively biased (from 0-10 kV) substrate held at 30º with respect to the incident beam. The neutral particles are unaffected by the bias voltage and landed softly as usual on the substrate holder. The positively charged particles are repelled away from the substrate as shown in figure 7.1 (a).

7.3.2. MD Simulation

Figure 7.1(b) shows snapshots of the evolution of an elliptical particle from a molecular dynamic simulation (MD). The MD simulation has been conducted using a method similar as reported in previous literatures[36,37], which shows that the aspect ratio of Fe nanoparticles can be controlled by oblique impact of the particle. The collected nanoparticles on the surface of the substrate are general hemi-ellipsoids with semi major axes $a > b > c$. The long axis a (easy axis) are parallel to the surface of the substrate plane. The axis b is parallel to the substrate plane and perpendicular to the easy axis. The axis c (hard axis) is perpendicular to the substrate plane. As reported previously, the ration c/a and b/a are approximately 1/6 and 1/3 respectively for the case of 15 kV bias voltage.[37]

7.3.3. Structural Characterization

The crystallographic structures and crystallite size of the nanocomposites were analyzed by means of grazing-incidence x-ray diffraction (GIXRD) using the Philips X'Pert multi-purpose diffractometer (MPD), operating at 45 kV and 40 mA with a fixed Cu anode. The morphologies of the individual nanoparticles were observed, by performing atomic force microscopy (AFM) with a Veeco di CP-II system on the samples deposited on the Si wafers for 25 s.

7.3.4. Magnetic Characterization

Magnetic measurements were carried out at RT using a vibrating sample magnetometer (VSM), with the external magnetic field (H) applied from -13.5 to 13.5 kOe. The out-of-plane angular remanence (AR) was measured by rotating the sample from perpendicular to parallel with respect to the external field. Thus, the remanence (M_r) was derived with the angle between H and the normal of the film plane. For the in-plane AR measurements, the sample was rotated around the substrate normal with H parallel to the film plane. In this case, M_r was extracted as a function of the angle of H with respect to the easy-axis of the nanocomposite. Thereafter, the magnetic hysteresis loops were

measured with *H* applied along the in-plane easy axis, in-plane hard axis and the hard axis of the sample, which were determined by the angular remanence measurements.

7.3.5. Electrical Characterization

The electrical resistivities of the nanocomposite films were obtained from standard four-probe measurements at RT. The frequency dependence of permeability spectra up to 8.5 GHz were measured using an Agilent E5071C network analyzer, based on a shorted microstrip transmission-line perturbation method.[38] Before the measurement, a standard OSL (open, short, load) one-port calibration was firstly made. Then an APE (automatic port extension) function was used to extend the calibration plane to where the strip line was connected to the connector. In doing so, a short-circuited SMA (Sub Miniature version A) connector of the same type as in the test fixture was measured. The set-up is shown in Figure 7.2 below.

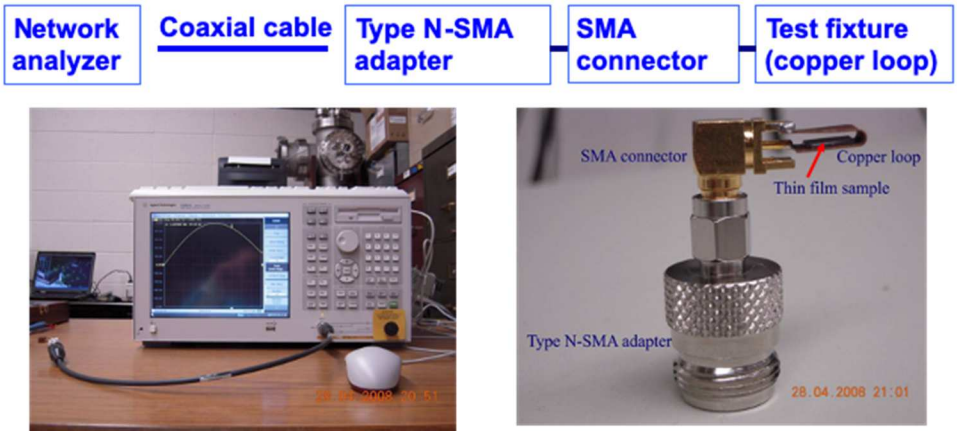

Figure 7.2 Set up for high Frequency permeability measurement using a shorted transmission-line perturbation method

7.4. Results and Discussions

7.4.1. Structural Analysis

The structure and phase of nanocomposite films prepared by oblique ECI have been studied using grazing-incidence x-ray diffraction (GIXRD). The background subtracted spectra are shown in

Figure 7.3 for various bias voltages. The diffraction pattern suggests the formation of Fe/Fe_3O_4 core-shell structures, which is consistent with previous observations.[32,34–36] Transmission electron microscopy observations are unavailable since the high energy impact damages carbon films on Cu grids. Figure 7.3 clearly shows that the proportions of the nanocomposite phases vary markedly with the applied bias voltages. Free drift nanoparticles (bias voltage = 0 V) that land softly are fully oxidized under the O_2 flow of 10 sccm, as suggested by the diffraction pattern in Figure 7.3 (a) showing emergence of a single phase of Fe_3O_4. An increase in the bias to 2.5 kV leads to the appearance of Fe (110) peak in addition to the Fe_3O_4 (311) and (440), as presented in Figure 7.3 (b). The weak peak from Fe_3O_4 (400) overlaps with the peak from Fe (110). Furthermore, the peak area ratio of Fe to Fe_3O_4 reaches maximum at the bias of 5 kV (see Figure 7.3 (c)), with the shell oxidized by exposure to atmosphere. Then the Fe/Fe_3O_4 peak area ratio slightly decreases as the potential continues to rise to 10 kV, as shown in Figure 7.3 (d). Using the "adiabatic" method, the weight fractions of Fe cores (W_{Fe}) and Fe_3O_4 shells ($W_{Fe_3O_4}$) can be calculated as

$$W_{Fe} = \frac{I_{Fe}}{I_{Fe} + \frac{I_{Fe_3O_4}}{K_{Fe}^{Fe_3O_4}}} \text{ and } W_{Fe_3O_4} = \frac{I_{Fe_3O_4}}{I_{Fe_3O_4} + I_{Fe}K_{Fe}^{Fe_3O_4}}, \tag{7.1}$$

where I_{Fe} and $I_{Fe_3O_4}$ are the strongest diffraction intensity of Fe and Fe_3O_4, respectively. $K_{Fe}^{Fe_3O_4}$ is the ratio of the RIR (reference intensity ratio) for Fe_3O_4 to Fe, which is obtained from the ICDD (International Centre for Diffraction Data) database. For a gas-phase Fe nanoparticle, the weight ratio of Fe_3O_4 to Fe is expected to decrease with the decrease of drift time (oxidation time) in the oxygen environment. The higher the bias voltage, the shorter the drift time is, and thus, the smaller fraction of Fe_3O_4 is, prior to full oxidation of the particles. The weight fraction of Fe_3O_4 ($W_{Fe_3O_4}$) decreases from 100% at 0 kV to 86% at 2.5 kV. At 5 kV, $W_{Fe_3O_4}$ reaches a minimum of 27% with the weight fraction of Fe (W_{Fe}) being a maximum of 73%. Upon elevating the potential to

10 kV, $W_{Fe_3O_4}$ rises and W_{Fe} decreases slightly to 33% and 67%, respectively. The broadening of the diffraction peaks is a result of small grain size. According to the Scherrer formula, both the average thickness of the crystalline Fe_3O_4 shells and the average size of the crystalline Fe cores for bias of 5 kV have been estimated to be 3 ± 1 nm. It should be noted that for the sample prepared at 2.5 kV, GIXRD was performed at different placement orientations (0° and 90°). The results from the two measurements are found to be identical (data not shown), indicating that the deposited film does not have a preferred structural orientation. Thus, the above estimation of the weight percentages based on the standard RIR values should be valid for these powder-like polycrystalline films.

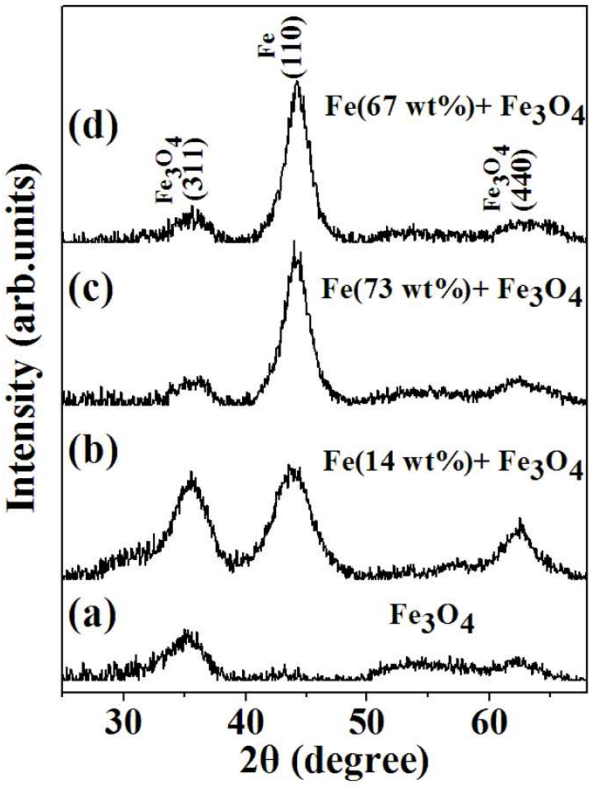

Figure 7.3 Background subtracted GIXRD patterns for the Fe/Fe_3O_4 nanocomposites prepared with the potentials of (a) 0 kV, (b) 2.5 kV, (c) 5 kV and (d) 10 kV. (a), (b) and (d) are at 10 sccm O_2 and (c) are without O_2 flow.

To assess the effects of ECI on the shapes of the Fe/Fe_3O_4 core-shell nanoparticles, two-dimensional (2D) AFM measurements are performed on selected single particle at different bias voltages, as shown in Figure 7.4. As seen in Figure 7.4 (a), the Fe_3O_4 nanoparticle is almost round on the substrate plane, implying that it retains the initial spherical shape with no potential applied.[29–32] As illustrated in Figure 7.4 (b-d), the increasing potential from 2.5 to 10 kV induces the Fe/Fe_3O_4 nanoparticles to become in-plane elliptical, indicating the induction of general hemi-ellipsoids from original spheroids by applying the potential to the tilted substrate. Moreover, height profiles are extracted from the AFM images, which show the principal axis ratios $\frac{b}{a}$ and $\frac{c}{a}$ of the hemi-ellipsoidal Fe/Fe_3O_4 nanoparticles. Here a, b, and c represent the long, intermediate and short axes of the hemi-ellipsoid, respectively. It is derived from Figure 7.4 (b-d) that $\frac{b}{a}$ is 0.85 at the potential of 2.5 kV, which declines from 0.78 to 0.72 as the potential increases from 5 to 10 kV. Meanwhile, $\frac{c}{a}$ also exhibits the monotonic reduction from 0.21 to 0.15 with the bias voltages going up from 2.5 to 10 kV. Therefore, it is obvious that enhancing the oblique bombardment of the Fe/Fe_3O_4 core-shell nanoparticles drives them to be more ellipsoidal.

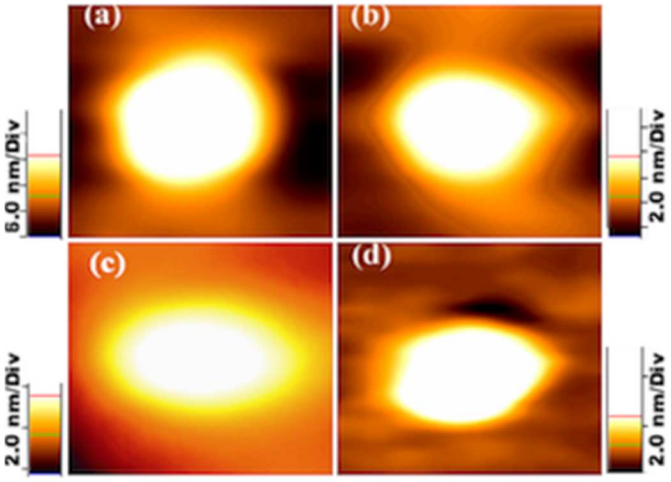

Figure 7.4 Two-dimensional AFM images of the Fe/Fe_3O_4 nanocomposites prepared at the potentials of (a) 0 kV, (b) 2.5 kV, (c) 5 kV and (d) 10 kV, with the same scan sizes of $60\ nm \times 60\ nm$.

Three-dimensional (3D) AFM observations further confirm that the Fe/Fe_3O_4 core-shell nanoparticles take on the hemi-ellipsoidal shapes by applying the potential from 0 to 10 kV to the inclined Si substrate. The morphology analysis for a typical example prepared at 5 kV is exhibited in Figure 7.5 As seen in Figure 7.5 (a), the 3D AFM image clearly shows the hemi-ellipsoidal nature of the energetically deposited nanoparticle. Both the long a and the intermediate b axes are parallel to the plane of the Si substrate, while the short c axis is perpendicular to the plane. Figure 7.5 (b) and (c) represent the nanoparticle height profiles along a and b axes respectively. It is illustrated that $a > b > c$ with $a = 30.6$ nm, $b = 23.8$ nm, and $c = 5.8$ nm. Moreover, the height plot does not appear perfectly symmetric in the a axis. This may arise from the asymmetric spreading-out of the particle collision pressure on the substrate slope direction, which asymmetrically moves the downhill mass and causes its asymmetric distribution along the a axis.[36]

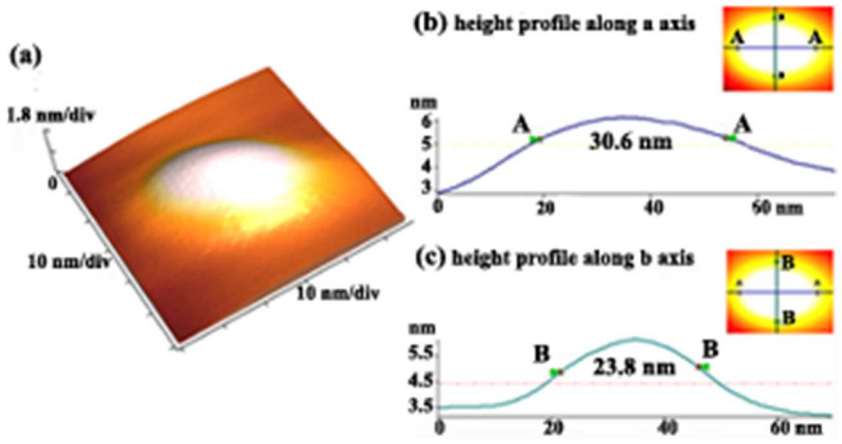

Figure 7.5(a) Three-dimensional AFM images for the Fe/Fe_3O_4 nanocomposite prepared at the potential of 5 kV, with its height profiles along (b) a axis and (c) b axis, respectively.

Energetic nanoparticle impact (ENI) also exerts pronounced effects on the morphology evolution of the Fe/Fe_3O_4 nanocomposites. This can be seen from their plane-view Sem images in the

insets of Figure 7.6. Without the applied bias voltage, the softly landed film contains inhomogenous aggregation of Fe/Fe_3O_4 nanoparticles, which porously stack on the Si substrate. As the potential rises from 2.5 to 10 kV, the Fe/Fe_3O_4 nanoparticle assemblies display increasingly dense and compact structures with improved surface smoothness. These results agree with the weakened RMS (root mean square) roughness from 20.0 to 1.4 nm with increasing the potential from 0 to 10 kV obtained from the AFM measurements. Similarly, TiN coatings deposited by ENI also exhibit the declining surface roughness.[39] It is well established by the MD simulations that ENI can supply activation energy to enhance the surface diffusion and the lateral particle expansions.[40,41] As a result, the high parts of the nanoparticles are transferred to fill the valleys, which suppresses the spatial fluctuation and thus reduces the nanocomposites surface roughness.[42] This increased packing-density by ENI tends to improve the magnetic softness and is also observed in the Fe and Fe-Co energetic nanoparticle assemblies.[25,37,43]

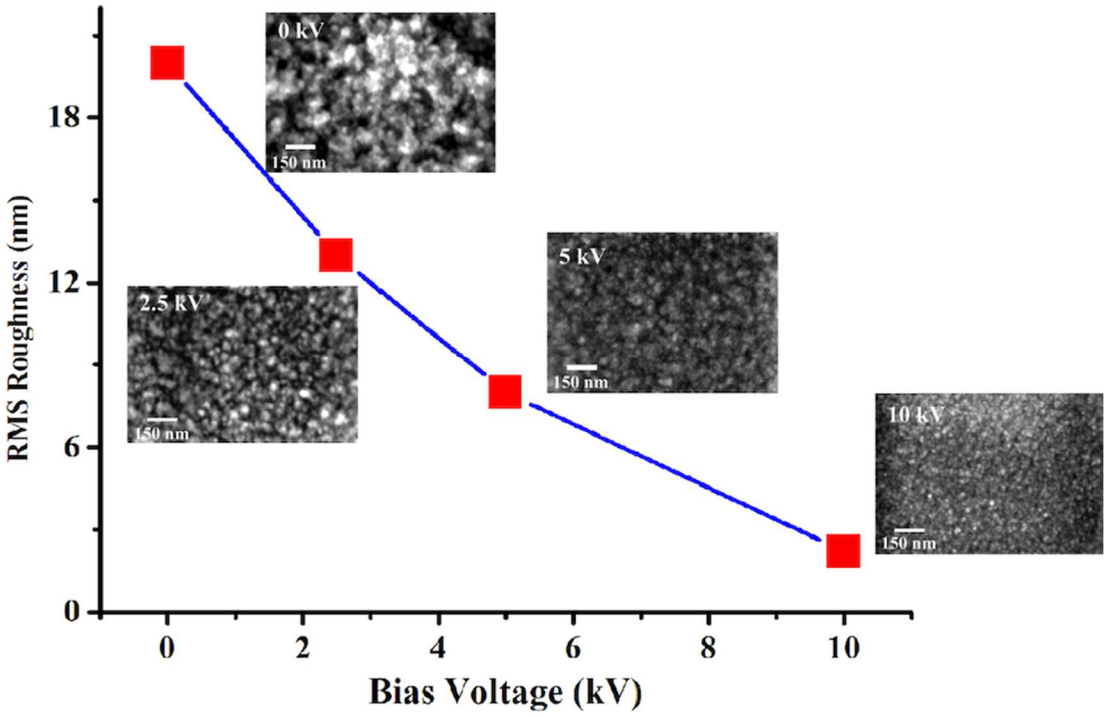

Figure 7.6 RMS (root mean square) roughness of the Fe-Fe_3O_4 nanocomposite at different bias voltages showing increased smoothness with the increasing bias voltages. The insets are scanning electron micrographs showing decreasing porosity with the increasing bias voltages.

7.4.2. Magnetic Properties

Based on the above structure characterizations, the Fe/Fe_3O_4 nanocomposite film can be regarded as an assembly of the hemi-ellipsoidal nanoparticles with the principal axes $a > b > c$, which is schematically sketched in Figure 7.7. For a general ellipsoid which is uniformly magnetized, the demagnetization energy density (E_D) is represented as[44]

$$E_D = \frac{1}{2}\mu_0 M_s^2 (N_a \cos^2\alpha_a + N_b \cos^2\alpha_b + N_c \cos^2\alpha_c), \quad 7.2)$$

where M_s is the ellipsoid's saturation magnetization and μ_0 the vacuum permeability. $\cos\alpha_a$, $\cos\alpha_b$ and $\cos\alpha_c$ are the direction cosines of M_s relative to a, b, and c axes, respectively. N_a, N_b, and N_c are the demagnetization factors for a, $b$and c axes, respectively.

Since $\cos^2\alpha_a + \cos^2\alpha_b + \cos^2\alpha_c = 1$, the demagnetization energy density (E_D) of a general ellipsoid can be calculated as[44]

$$E_D = \frac{1}{2}\mu_0 M_s^2 [(N_a - N_c)\cos^2\alpha_a + (N_b - N_c)\cos^2\alpha_b + N_c] \quad 7.3$$

The easy axis of the ellipsoid is determined by minimizing E_D with

$$\frac{\partial E_D}{\partial \alpha_a} = \frac{\partial E_D}{\partial \alpha_b} = 0 \quad 7.4$$

Solving it leads to $(\alpha_a^1, \alpha_b^1, \alpha_c^1) = (0, \frac{\pi}{2}, \frac{\pi}{2})$, $(\alpha_a^2, \alpha_b^2, \alpha_c^2) = (\frac{\pi}{2}, 0, \frac{\pi}{2})$ and $(\alpha_a^3, \alpha_b^3, \alpha_c^3) = (\frac{\pi}{2}, \frac{\pi}{2}, 0)$, which correspond to a、b and c axes, respectively. The results are then used to calculate Hesse matrix $|H_f| = AC - B^2$, where $A = \frac{\partial^2 E_D}{\partial \alpha_a^2}$, $B = \frac{\partial^2 E_D}{\partial \alpha_a \partial \alpha_b} = 0$ and

$C = \frac{\partial^2 E_D}{\partial \alpha_b^2}$. For $(\alpha_a^1, \alpha_b^1, \alpha_c^1) = (0, \frac{\pi}{2}, \frac{\pi}{2})$, $\left|H_f\right| > 0$ and $A > 0$, which suggests that E_D is minimized along the a axis. For $(\alpha_a^3, \alpha_b^3, \alpha_c^3) = (\frac{\pi}{2}, \frac{\pi}{2}, 0)$, $\left|H_f\right| > 0$ while $A < 0$, indicating the maximization of E_D in the c axis. Since $\left|H_f\right| < 0$ for $(\alpha_a^2, \alpha_b^2, \alpha_c^2) = (\frac{\pi}{2}, 0, \frac{\pi}{2})$, E_D does not reach extremum along the b axis. Accordingly, a and c axes are the only easy and hard axes of the ellipsoidal Fe/Fe_3O_4 core-shell nanoparticle with uniaxial shape anisotropy.

Consider the demagnetization energy density (E_d) of a general ellipsoid in the $a-b$ plane as

$$E_d = \frac{1}{2}\mu_0 M_s^2 (N_a \cos^2 \alpha_a + N_b \cos^2 \alpha_b) \tag{7.5}$$

The in-plane easy axis of the ellipsoid is determined by minimizing E_d with

$$\frac{\partial E_d}{\partial \alpha_a} = 0 \tag{7.6}$$

With $\cos^2 \alpha_a + \cos^2 \alpha_b = 1$, solving equation (5) leads to $(\alpha_a^1, \alpha_b^1) = (0, \frac{\pi}{2})$ and $(\alpha_a^2, \alpha_b^2) = (\frac{\pi}{2}, 0)$, which correspond to a and b axes, respectively. Since $\frac{\partial^2 E_d}{\partial \alpha_a^2} > 0$ at $(\alpha_a^1, \alpha_b^1) = (0, \frac{\pi}{2})$, E_d is minimized along a axis in the $a-b$ plane, indicating that a axis is the only in-plane easy axis. Since $\frac{\partial^2 E_d}{\partial \alpha_a^2} < 0$ at $(\alpha_a^2, \alpha_b^2) = (\frac{\pi}{2}, 0)$, E_d is maximized along b axis in $a-b$ plane, suggesting that the b axis is the only in-plane hard axis.

As discussed above, uniaxial shape anisotropy is induced in the ellipsoidal Fe/Fe_3O_4 core-shell nanoparticle. a axis is the only easy-axis of the general ellipsoid, which is perpendicular to the

hard c axis. Moreover, a axis is also the only easy-axis in the $a-b$ plane with b axis being the in-plane hard axis. When the ellipsoidal nanoparticles with uniaxial shape anisotropy are further assembled with the alignment of their a axes, the Fe/Fe_3O_4 nanocomposite film exhibits in-plane uniaxial anisotropy, as illustrated in Figure 7.7. This also results from the fact that both the easy a axes and $a-b$ planes are parallel to the Si substrate plane, as demonstrated in Figures 7.4 and 7.5.

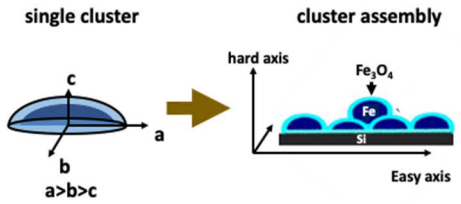

Figure 7.7 Schematic illustration of the nanocomposite assembled by the hemi-ellipsoidal Fe/Fe_3O_4 core-shell nanoparticles, based on which the in-plane uniaxial anisotropy is interpreted.

The in-plane anisotropy of the Fe/Fe_3O_4 nanocomposites can be verified by the out-of-plane angular remanence (AR), whose measurement apparatus is schematically illustrated in Figure 7.8 (a). It is shown that the sample is rotated by 360° around an axis in the substrate plane, during which the remanence (M_r) is measured by VSM as a dependence on the angle θ_o between the applied field (H) and the plane normal. The measured out-of-plane AR for the samples with the incremental potentials are presented in Figures 7.8 (b)-(e). When there is no potential applied (Figure 7.8 (b)), M_r almost remains constant during the film rotation. This is because the softly-landed Fe_3O_4 nanoparticles retain their original spherical shapes, by which no shape anisotropy can be induced. With applying the potential from 2.5 to 10 kV (Figures 7.8 (c)-(e)), all the Fe/Fe_3O_4 nanocomposites show the sine-like AR. It is seen that all the M_r values are maximized and minimized with H being parallel and perpendicular to the substrate, respectively. This clearly demonstrates that the samples' easy-axes all lie in their planes, which is an evidence for the in-plane anisotropy. Since the in-plane rotation axes are arbitrarily chosen, the direction of the maximum M_r in the out-of-plane AR cannot be concluded

to be the only easy-axis. Therefore, the in-plane anisotropy of the entire nanocomposite film cannot be determined to be uniaxial by this method.

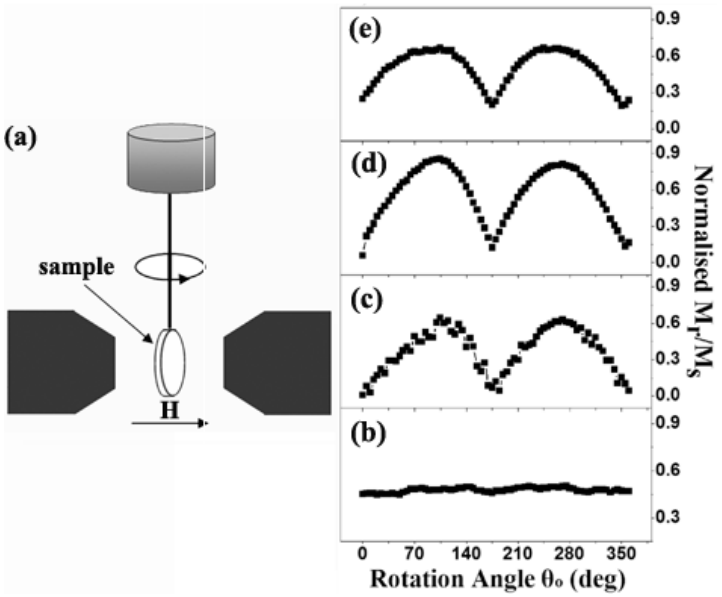

Figure 7.8(a) Schematic drawing of equipment structure for the out-of-plane angular remanence measurements and the measured out-of-plane angular remanence for the Fe/Fe_3O_4 nanocomposites prepared at the potentials of (b) 0 kV, (c) 2.5 kV, (d) 5 kV and (e) 10 kV.

Furthermore, the in-plane uniaxial anisotropy of the Fe/Fe_3O_4 nanocomposites can be confirmed by measuring the in-plane AR around the film normal, whose schematic measurement equipment is represented in Figure 7.9 (a). Figures 7.9 (b)-(e) show the measured results for the nanocomposite films with the increasing bias voltages. It is seen in Figure 7.9 (b) that M_r is almost independent of the rotation angle θ_i for the sample without applying the potential, due to the isotropic characteristic of the spherical nanoparticles. Applying the potential remarkably induces the uniaxial anisotropy in the film planes of the Fe/Fe_3O_4 nanocomposites, which is evident in their cosine-like in-plane AR. As shown in Figures 7.9 (c)-(e), the periods of the in-plane AR curve are 180° for all the samples and the maximum M_r deviates from the minimum by 90°. This strongly indicates the

existence of only one easy-axis in the sample plane, which makes 90° with the in-plane hard-axis. Since the out-of-plane AR has verified the in-plane anisotropy, the sole in-plane easy-axis should have the minimum anisotropy energy and thus is also the only easy-axis of the entire sample. Accordingly, it is confirmed that the Fe/Fe_3O_4 nanocomposite films are induced to be in-plane uniaxially anisotropic by the oblique ENI at RT, with the easy- and hard-axes being parallel and perpendicular to the Si substrate, respectively.

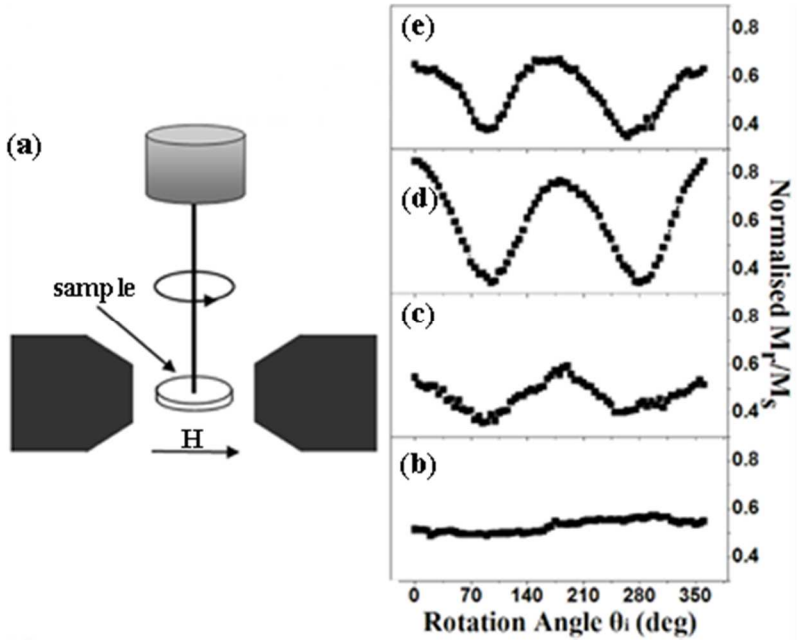

Figure 7.9(a) Schematic drawing of equipment structure for the in-plane angular remanence measurements and the measured in-plane angular remanence for the Fe/Fe_3O_4 nanocomposites prepared at the potentials of (b) 0 kV, (c) 2.5 kV, (d) 5 kV and (e) 10 kV.

With *H* applied along the in-plane easy- and hard-axes determined by the in-plane AR, the magnetic hysteresis loops were measured for the Fe/Fe_3O_4 nanocomposites by increasing the potentials, as shown in Figure 7.10. From Figure 7.10 (a) it can be seen that the Fe_3O_4 nanoparticle film is almost isotropic with the softly-landing nanoparticles maintaining their initial spherical shapes, which agrees with the AR results. By increasing the potential from 2.5 to 10 kV, the oblique ENI

induces the strong in-plane uniaxial anisotropy in the Fe/Fe_3O_4 nanocomposite films. This is clearly justified by the much larger M_r of the in-plane easy-loops than that of the in-plane hard-loops, as displayed in Figure 7.10 (b-d). This well-defined in-plane uniaxial anisotropy can be further confirmed by the remarkable difference between the easy and the hard loops of the Fe/Fe_3O_4 nanocomposite films in Figure 7.10.

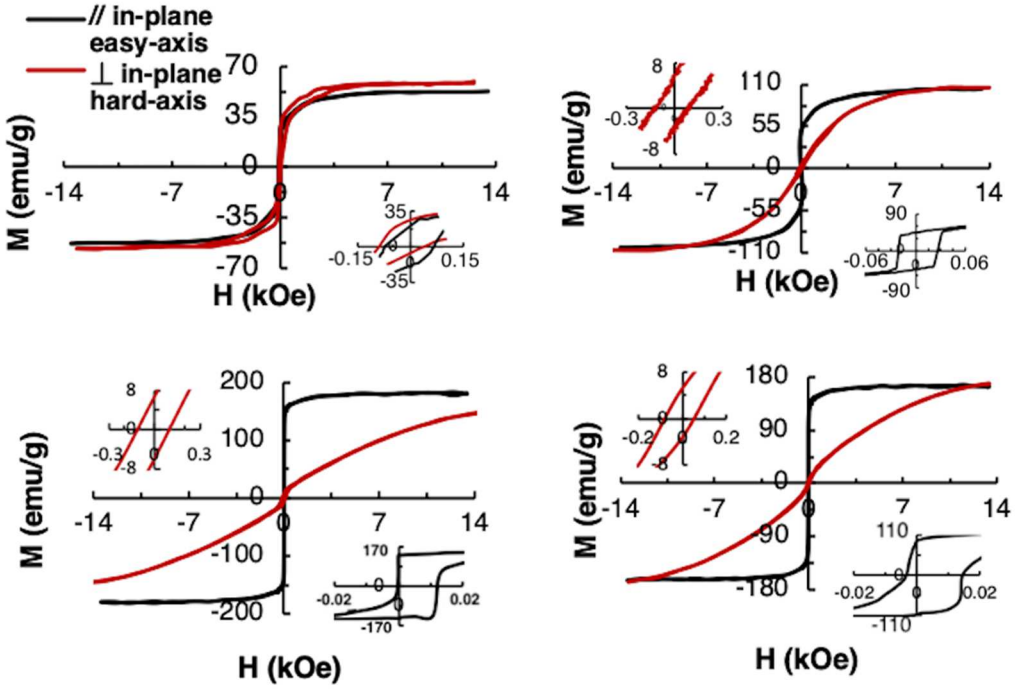

Figure 7.10 In-plane easy and hard magnetic hysteresis loops of the Fe/Fe_3O_4 nanocomposites prepared with the potentials of (a) 0 kV, (b) 2.5 kV, (c) 5 kV and (d) 10 kV. Insets are magnified images near zero field.

As illustrated in Figure 7.10, the Fe/Fe_3O_4 nanocomposites demonstrate excellent magnetic softness, with the easy coercivity (H_{cE}) decreasing from 54.4 to 6 Oe as the potential increases from 0 to 5 kV. It is well established that the exchange interaction can force the magnetization to deviate

from the local easy-axis and thus average out the magneto-crystalline anisotropy $\langle K \rangle$ over the exchange correlation length as[34]

$$\langle K \rangle = \frac{K_1}{\sqrt{N}} = K_1^4 \frac{D^6}{A^3} \quad 7.7$$

Where K_1 is the first-order anisotropy constant, N the number of grains within the ferromagnetic exchange length, D the grain size and A the exchange stiffness. Since strengthening the ENI improves the nanoparticles packing-density and reduces the Fe_3O_4/Fe ratio, the number of particles per unit volume is increased and the anisotropy constant K_1 is reduced. Hence the effective anisotropy $\langle K \rangle$ is weakened, which causes the decrease of H_{cE}.[37,43,45] Further elevating the potential to 10 kV increases the Fe_3O_4 fraction, thus suppressing the exchange stiffness between the Fe/Fe_3O_4 core-shell nanoparticles. Consequently, H_{cE}rises slightly to 8 Oe. Meanwhile, M_s of the samples increases from 53.2 up to 183.3 emu/g with increasing the potential from 0 to 5 kV, which is ascribed to the improved particle packing-density[43,45] and the increased Fe fraction from 0 to 73%. As the bias voltage rises to 10 kV, M_s falls to 166.6 emu/g with the Fe fraction declining to 67%. Accordingly, the excellent magnetic softness of the Fe/Fe_3O_4 nanocomposites indicates a potential for good magnetic response at high frequencies. In addition, easy remanence ratio (S_E) of the samples goes up from 0.5 to 0.85 with increasing the potential from 0 to 5 kV. Then it drops to 0.67 as the potential reaches 10 kV. The variation of S_E may indicate the changed nanoparticle alignment by ENI (see Figure 7.11).

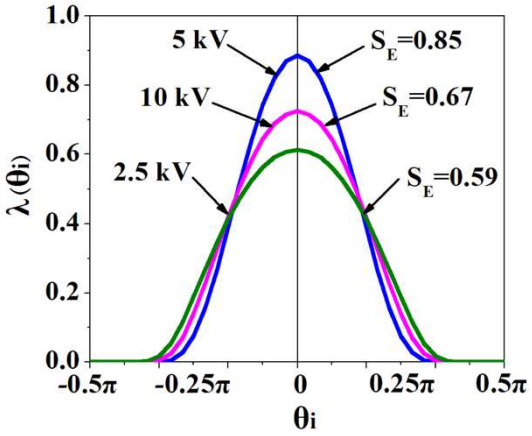

Figure 7.11 Particle orientation distribution probability densities of the Fe/Fe_3O_4 nanocomposites prepared at the potentials of 2.5 kV, 5 kV and 10 kV, respectively.

Since M_r is the average projection of M_s on the direction of H under zero applied field, S_E with different particle alignments can be obtained by[46]

$$S_E = \frac{M_r}{M_s} = \frac{1}{\sqrt{2\pi}\sigma}\int_{-\pi/2}^{\pi/2} \exp\left(-\frac{tg^2\theta_i}{2\sigma^2}\right)\cos\theta_i d(tg\theta_i), \quad 7.8$$

where θ_i is the angle between H and the easy a axis on the sample plane, and the interaction effect is neglected for the simplicity of calculation. The particles orientation distribution probability density $\lambda(\theta_i)$ is assumed to obey a tangent type Gaussian distribution function

$$\lambda(\theta_i) = \frac{1}{\sqrt{2\pi}\sigma}\exp\left(-\frac{tg^2\theta_i}{2\sigma^2}\right), \quad 7.9$$

which is adopted to fulfill $\int_{-\infty}^{+\infty}\lambda(x)\,dx = 1$ with x replaced by $tg\theta_i$. σ is a parameter used to describe the alignment degree. By solving the supplementary equations (5) and (6), the orientation distribution of the Fe/Fe_3O_4 nanoparticles with different S_E are obtained. As derived above, the degree of the nanoparticle alignment increases with the increasing potential from 2.5 to 5 kV, hence causing the increment of S_E. As the potential further increases to 10 kV the alignment is weakened, which results in the S_E reduction.

As also exhibited in Figure 7.10, the in-plane uniaxial anisotropy field (H_K) for the nanocomposites increases from 8.4 kOe to above 13.5 kOe with increasing the potential from 2.5 to 5 kV. Here, H_K is determined by the intersection of the in-plane easy-loop with the in-plane hard-loop. As the potential further rises to 10 kV, H_K declines to 12.4 kOe. It is sensible that the oblique ENI at RT can induce and tailor the in-plane uniaxial anisotropy of the Fe/Fe_3O_4 nanocomposites by changing the shapes of the individual nanoparticles and their alignment. This is essential to obtain excellent and controllable magnetic high-frequency properties in these nanocomposite films.[3,10–12]

In addition, the hysteresis loops of the nanoparticles shifted along the field axis. This loop shift is known as exchange bias. The shift is significant at bias voltages of 5 kV and 10 kV when measured along the easy axis and is approximately equal to 6 Oe at both the voltages. Our previous work reported that the exchange bias arising from magnetic coupling between the spins at the iron core surface and the iron oxide inner surface at the core-shell interface is due to exchange coupling between the oxide shell and the ferromagnetic core and dipole-dipole interactions between the particles.[47] Literatures have suggested that uniaxial shape anisotropy can also induce the exchange bias.[48,49] We anticipate that the exchange bias arising in our case is due to shape anisotropy effect. The change in shape could have changed the preference of the alignment of the spins and induces the exchange bias in the nanocomposite.

7.4.3. Electrical and High-Frequency Properties

By a conventional four-probe method, resistivities were measured for the samples with the enhanced ENI at RT. With no potential applied, the Fe_3O_4 nanoparticle film exhibit the high resistivity of 23,800 μΩ·cm, which is the same order as that of polycrystalline Fe_3O_4 films ($\sim 10^4$ μΩ·cm).[38,50] At the potential of 2.5 kV, the resistivity of the Fe/Fe_3O_4 nanocomposite film abruptly drops to 214 μΩ·cm. The nanocomposite still maintains the high resistivity of 123 μΩ·cm as the Fe fraction is maximized at the potential of 5 kV. The resistivity degradation may also result from the

increased nanoparticle packing-density by strengthening the ENI (see figure 7.6). With further increasing the potential to 10 kV, the Fe_3O_4 fraction increases and provides more electrical barriers between the nanoparticles, thereby improving the nanocomposite's resistivity to 139 μΩ·cm.

To evaluate the power loss of the Fe/Fe_3O_4 nanocomposites, the frequency dependence of the imaginary permeability was measured up to 8.5 GHz, which is shown in Figure 7.12. At the potential of 2.5 kV, the spectrum flattens at up to 3.7 GHz and rises to a maximum at 4.8 GHz, which is then followed by a downward trend. With increasing the potential to 5 kV, μ'' remains almost zero until the frequency reaches 4.7 GHz, indicating little power loss in this band range. Afterward, μ'' increases but is not maximized at a frequency as high as 8.5 GHz, which suggests that the ferromagnetic resonance frequency f_{FMR} is larger than 8.5 GHz. For the nanocomposite prepared at 10 kV, f_{FMR}determined to be 5 GHz where μ'' spectrum exhibits a peak. Strikingly, μ'' continues to rise after the resonance peak, which has also been observed in the permalloy films deposited on Si substrates.[51] This may arise from the varied dielectric constant of the strip line, which is inhomogeneously filled with Si and air. Due to the high permittivity ($\varepsilon_r = 11.7 - 12.9$) of Si, it is usually difficult to appraise the permeability of magnetic films on Si wafers.[51] Therefore, a detailed equivalent circuit model is further needed to take into account the fixture's effective dielectric constant for quantitatively analyzing the permeability spectra of the Fe/Fe_3O_4 nanocomposites.

Usually, a ferromagnet's power loss arises from three main sources. In the low frequency range, the hysteresis loss plays a crucial role and can be minimized by avoiding the domain wall displacement. The eddy current loss dominates over the intermediate range, which can be suppressed by enhancing the resistivity to increase the skin depth. Moreover, ferromagnetic resonance occurs when the frequency is high enough to match the characteristic precession frequency of the spins in the material. According to the Kittel's equation, f_{FMR} can be theoretically represented as[9]

$$f_{FMR} = \frac{\gamma}{2\pi}\sqrt{J_s \mu_0 H_k} \quad (3)$$

where γ is the gyro magnetic constant which is in the order of 178 GHz/T for Fe based materials and J_s refers to the saturation polarization. The high ρ with the relatively high product of H_K and M_s shifts the sample's f_{FMR} to 4.8 GHz, as the potential of 2.5 kV is applied. With increasing the potential to 5 kV, both H_K and M_s of the nanocomposite are significantly enhanced (illustrated in Figure 7.10). Thus, f_{FMR} rises beyond 8.5 GHz, in spite of the decreased ρ. Since both H_K and M_s of the sample declines as the potential increases to 10 kV, f_{FMR} falls to 5 GHz. Thus, it is interpreted that changing ENI can control the high-frequency dynamic properties for the Fe/Fe_3O_4 nanoparticle composites, through tuning both H_K and M_s at RT.

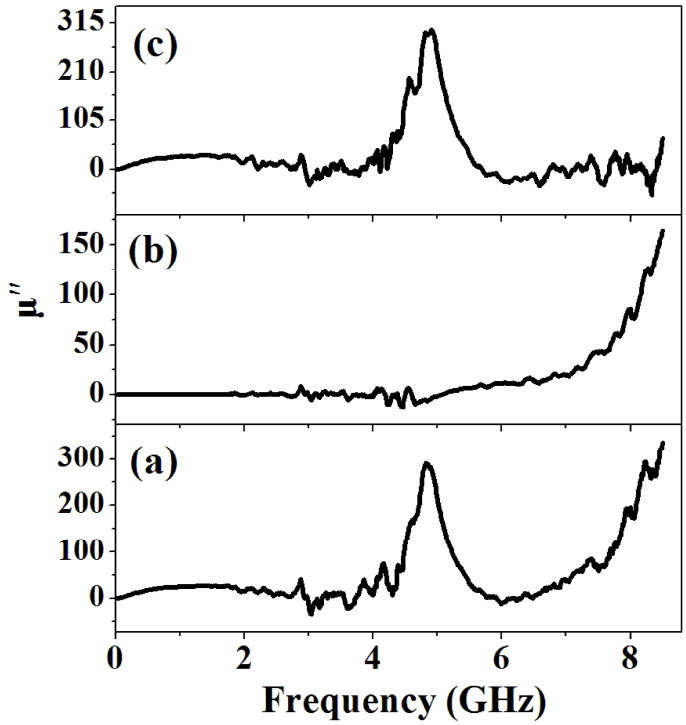

Figure 7.12 The imaginary permeability spectra for the Fe/Fe_3O_4 nanocomposites prepared with the potentials of (a) 2.5 kV, (b) 5 kV and (c) 10 kV.

7.5. Conclusion

At RT, oblique energetic nanoparticle impact (ENI) is employed to induce and tailor the in-plane uniaxial anisotropy in the Fe/Fe_3O_4 nanoparticle-assembled nanocomposites, which is attributed to the tunable uniaxial shape anisotropy of the individual Fe/Fe_3O_4 core-shell nanoparticles and the nanoparticle alignment. Moreover, excellent magnetic softness and good electrical properties are obtained by combining the high saturation magnetization of the Fe cores and the large resistivity of the Fe_3O_4 shells. The nanocomposite prepared at the bias voltage of 5 kV exhibits H_k larger than 13.5 kOe, M_s 183.3 emu/g and ρ 123 μΩ·cm, which shows a great potential of the highest f_{FMR} of 8.5 GHz. These new soft magnetic materials with Si-process compatibility are highly promising for efficient and controllable high-frequency magnetic performance in the next-generation wireless network and miniaturized electronic devices.

7.6. Acknowledgements

This work supported by DOD-AFRL (FA9453-06-1-0355-P1) and DOE-BES (DE-FG02-06ER15777) is greatly acknowledged. The TEM and XRD measurements were conducted at the Environmental Molecular Sciences Laboratory, a national scientific user facility at Pacific Northwest National Laboratory managed by the Department of Energy's Office of Biological and Environmental Research. Pacific Northwest National Laboratory is operated for the U.S. Department of Energy by Battelle under Contract DE-AC06-76RLO 1830.

7.7. References

(1) Henry, C. SpaceX Launches Second Batch of Starlink Broadband Satellites. *SpaceNews*. online November 11, 2019.

(2) Falub, C. V.; Bless, M.; Hida, R.; Meduňa, M.; Ammann, A. Innovative Soft Magnetic Multilayers with Enhanced In-Plane Anisotropy and Ferromagnetic Resonance Frequency for Integrated RF Passive Devices. *AIP Advances* **2017**, *8* (4), 048002. https://doi.org/10.1063/1.4993688.

(3) Korenivski, V. GHz Magnetic Film Inductors. *Journal of Magnetism and Magnetic Materials* **2000**, *215–216*, 800–806. https://doi.org/10.1016/S0304-8853(00)00292-4.

(4) Gardner, D. S.; Schrom, G.; Hazucha, P.; Paillet, F.; Karnik, T.; Borkar, S.; Saulters, J.; Owens, J.; Wetzel, J. Integrated On-Chip Inductors with Magnetic Films. In *2006 International Electron Devices Meeting*; 2006; pp 1–4. https://doi.org/10.1109/IEDM.2006.347002.

(5) Seemann, K.; Leiste, H.; Ziebert, C. Soft Magnetic FeCoTaN Film Cores for New High-Frequency CMOS Compatible Micro-Inductors. *Journal of Magnetism and Magnetic Materials* **2007**, *316* (2), e879–e882. https://doi.org/10.1016/j.jmmm.2007.03.126.

(6) Ohnuma, S.; Fujimori, H.; Masumoto, T.; Xiong, X. Y.; Ping, D. H.; Hono, K. FeCo–Zr–O Nanogranular Soft-Magnetic Thin Films with a High Magnetic Flux Density. *Appl. Phys. Lett.* **2003**, *82* (6), 946–948. https://doi.org/10.1063/1.1537456.

(7) Wang, S. X.; Sun, N. X.; Yamaguchi, M.; Yabukami, S. Properties of a New Soft Magnetic Material. *Nature* **2000**, *407* (6801), 150–151. https://doi.org/10.1038/35025142.

(8) Beach, G. S. D.; Berkowitz, A. E.; Parker, F. T.; Smith, D. J. Magnetically Soft, High-Moment, High-Resistivity Thin Films Using Discontinuous Metal/Native Oxide Multilayers. *Appl. Phys. Lett.* **2001**, *79* (2), 224–226. https://doi.org/10.1063/1.1383998.

(9) Périgo, E. A.; Weidenfeller, B.; Kollár, P.; Füzer, J. Past, Present, and Future of Soft Magnetic Composites. *Applied Physics Reviews* **2018**, *5* (3), 031301. https://doi.org/10.1063/1.5027045.

(10) Buznikov, N. A.; Rozanov, K. N. The Effect of Stripe Domain Structure on Dynamic Permeability of Thin Ferromagnetic Films with Out-of-Plane Uniaxial Anisotropy. *Journal of Magnetism and Magnetic Materials* **2005**, *285* (3), 314–326. https://doi.org/10.1016/j.jmmm.2004.07.050.

(11) Kittel, C. On the Theory of Ferromagnetic Resonance Absorption. *Phys. Rev.* **1948**, *73* (2), 155–161. https://doi.org/10.1103/PhysRev.73.155.

(12) Snoek, J. L. Dispersion and Absorption in Magnetic Ferrites at Frequencies above One Mc/s. *Physica* **1948**, *14* (4), 207–217. https://doi.org/10.1016/0031-8914(48)90038-X.

(13) Jin, S.; Zhu, W.; van Dover, R. B.; Tiefel, T. H.; Korenivski, V.; Chen, L. H. High Frequency Properties of Fe–Cr–Ta–N Soft Magnetic Films. *Appl. Phys. Lett.* **1997**, *70* (23), 3161–3163. https://doi.org/10.1063/1.119120.

(14) Yamaguchi, M.; Hyeon Kim, K.; Ikedaa, S. Soft Magnetic Materials Application in the RF Range. *Journal of Magnetism and Magnetic Materials* **2006**, *304* (2), 208–213. https://doi.org/10.1016/j.jmmm.2006.02.143.

(15) Krusch, K. Sputter Parameters and Magnetic Properties of Permalloy for Thin Film Heads. *IEEE Transactions on Magnetics* **1986**, *22* (5), 626–628. https://doi.org/10.1109/TMAG.1986.1064586.

(16) Kataoka, N.; Hosokawa, M.; Inoue, A.; Masumoto, T. Magnetic Properties of Fe-Based Binary Crystalline Alloys Produced by Vapor Quenching. *Jpn. J. Appl. Phys.* **1989**, *28* (3A), L462. https://doi.org/10.1143/JJAP.28.L462.

(17) Kataoka, N.; Sumiyama, K.; Nakamura, Y. Metastable Crystalline and Amorphous Fe–V Alloys Produced by Vapor Quenching. *Transactions of the Japan Institute of Metals* **1986**, *27* (11), 823–829. https://doi.org/10.2320/matertrans1960.27.823.

(18) Hayakawa, Y.; Makino, A.; Fujimori, H.; Inoue, A. High Resistive Nanocrystalline Fe-M-O (M=Hf, Zr, Rare-Earth Metals) Soft Magnetic Films for High-Frequency Applications (Invited). *Journal of Applied Physics* **1997**, *81* (8), 3747–3752. https://doi.org/10.1063/1.365498.

(19) Ha, N. D.; Phan, M.-H.; Kim, C. O. Novel Nanostructure and Magnetic Properties of Co–Fe–Hf–O Films. *Nanotechnology* **2007**, *18* (15), 155705. https://doi.org/10.1088/0957-4484/18/15/155705.

(20) Ohnuma, M.; Hono, K.; Onodera, H.; Ohnuma, S.; Fujimori, H.; Pedersen, J. S. Microstructures and Magnetic Properties of Co–Al–O Granular Thin Films. *Journal of Applied Physics* **1999**, *87* (2), 817–823. https://doi.org/10.1063/1.371948.

(21) Wang, Y.; Zhang, H.; Wang, L.; Bai, F. The Adjustable Anisotropy Field in FeCoTiO/SiO2/FeCoTiO Trilayer Films by Oblique Sputtering and Stripe Patterning. *AIP Advances* **2016**, *6* (5), 055912. https://doi.org/10.1063/1.4943243.

(22) Lu, G.; Zhang, H.; Pan, L.; Zhong, Z. Tuning of Soft Magnetic Properties in FeCoHfO Thin Films by Various Sputtering Power and Pressure. *Materials Research Innovations* **2014**, *18* (sup4), S4-619-S4-624. https://doi.org/10.1179/1432891714Z.000000000756.

(23) Viala, B.; Minor, M. K.; Barnard, J. A. Microstructure and Magnetism in FeTaN Films Deposited in the Nanocrystalline State. *Journal of Applied Physics* **1996**, *80* (7), 3941–3956. https://doi.org/10.1063/1.363352.

(24) Liu, Z. W.; Liu, Y.; Yan, L.; Tan, C. Y.; Ong, C. K. Thickness-Dependent Properties of FeTaN Thin Films Deposited on Flexible Substrate. *Journal of Applied Physics* **2006**, *99* (4), 043903. https://doi.org/10.1063/1.2170588.

(25) Ishiwata, N.; Wakabayashi, C.; Urai, H. Soft Magnetism of High□nitrogen□concentration FeTaN Films. *Journal of Applied Physics* **1991**, *69* (8), 5616–5618. https://doi.org/10.1063/1.347940.

(26) Ohnuma, S.; Kobayashi, N.; Masumoto, T.; Mitani, S.; Fujimori, H. Magnetostriction and Soft Magnetic Properties of (Co1−xFex)–Al–O Granular Films with High Electrical Resistivity. *Journal of Applied Physics* **1999**, *85* (8), 4574–4576. https://doi.org/10.1063/1.370412.

(27) Sato, T.; Miura, Y.; Matsumura, S.; Yamasawa, K.; Morita, S.; Sasaki, Y.; Hatanai, T.; Makino, A. New Applications of Nanocrystalline Fe(Co–Fe)–Hf–O Magnetic Films to Micromagnetic Devices. *Journal of Applied Physics* **1998**, *83* (11), 6658–6660. https://doi.org/10.1063/1.367586.

(28) Bekker, V.; Seemann, K.; Leiste, H. Development and Optimisation of Thin Soft Ferromagnetic Fe–Co–Ta–N and Fe–Co–Al–N Films with in-Plane Uniaxial Anisotropy for HF Applications. *Journal of Magnetism and Magnetic Materials* **2006**, *296* (1), 37–45. https://doi.org/10.1016/j.jmmm.2005.01.025.

(29) Qiang, Y.; Antony, J.; Sharma, A.; Nutting, J.; Sikes, D.; Meyer, D. Iron/Iron Oxide Core-Shell Nanoclusters for Biomedical Applications. *J Nanopart Res* **2006**, *8* (3), 489–496. https://doi.org/10.1007/s11051-005-9011-3.

(30) Wang, C. M.; Baer, D. R.; Thomas, L. E.; Amonette, J. E.; Antony, J.; Qiang, Y.; Duscher, G. Void Formation during Early Stages of Passivation: Initial Oxidation of Iron Nanoparticles at Room Temperature. *Journal of Applied Physics* **2005**, *98* (9), 094308. https://doi.org/10.1063/1.2130890.

(31) Wang, C.; Baer, D. R.; Amonette, J. E.; Engelhard, M. H.; Antony, J.; Qiang, Y. Morphology and Electronic Structure of the Oxide Shell on the Surface of Iron Nanoparticles. *J. Am. Chem. Soc.* **2009**, *131* (25), 8824–8832. https://doi.org/10.1021/ja900353f.

(32) Peng, D. L.; Hihara, T.; Sumiyama, K.; Morikawa, H. Structural and Magnetic Characteristics of Monodispersed Fe and Oxide-Coated Fe Cluster Assemblies. *Journal of Applied Physics* **2002**, *92* (6), 3075–3083. https://doi.org/10.1063/1.1501754.

(33) Khanal, L. R.; Williams, T.; Qiang, Y. High-Temperature Investigation on Morphology, Phase and Size of Iron/Iron-Oxide Core–Shell Nanoclusters for Radiation Nanodetector. *J. Phys. D: Appl. Phys.* **2018**, *51* (25), 255302. https://doi.org/10.1088/1361-6463/aac47e.

(34) Herzer, G. Grain Size Dependence of Coercivity and Permeability in Nanocrystalline Ferromagnets. *IEEE Transactions on Magnetics* **1990**, *26* (5), 1397–1402. https://doi.org/10.1109/20.104389.

(35) Haberland, H.; Karrais, M.; Mall, M.; Thurner, Y. Thin Films from Energetic Cluster Impact: A Feasibility Study. *Journal of Vacuum Science & Technology A* **1992**, *10* (5), 3266–3271. https://doi.org/10.1116/1.577853.

(36) Moseler, M.; Rattunde, O.; Nordiek, J.; Haberland, H. On the Origin of Surface Smoothing by Energetic Cluster Impact: Molecular Dynamics Simulation and Mesoscopic Modeling. *Nuclear Instruments and Methods in Physics Research Section B: Beam Interactions with Materials and Atoms* **2000**, *164–165*, 522–536. https://doi.org/10.1016/S0168-583X(99)01081-2.

(37) Meyer, D.; Faheem, M.; Campanell, M.; Antony, J.; Sharma, A.; Qiang, Y. Magnetic Nanocrystalline Films Softened by Obliquely Accelerating Iron Nanoclusters. *IEEE Transactions on Magnetics* **2007**, *43* (6), 3010–3012. https://doi.org/10.1109/TMAG.2007.893477.

(38) Korenivski, V.; Van Dover, R. B.; Mankiewich, P. M.; Ma, Z.-X.; Becker, A. J.; Polakos, P. A.; Fratello, V. J. A Method to Measure the Complex Permeability of Thin Films at Ultra-High Frequencies. *IEEE Transactions on Magnetics* **1996**, *32* (5), 4905–4907. https://doi.org/10.1109/20.539283.

(39) Qiang, Y.; Thurner, Y.; Reiners, T.; Haberland, H. Hard Coatings (TiN, TixAl1−xN) Deposited at Room Temperature by Energetic Cluster Impact. *Surface and Coatings Technology* **1998**, *100–101*, 27–32.

(40) Betz, G.; Husinsky, W. R. Cluster Bombardment of Solids: A Molecular Dynamics Study. *Nuclear Instruments and Methods in Physics Research Section B: Beam Interactions with Materials and Atoms* **1997**, *122* (3), 311–317.

(41) Haberland, H.; Insepov, Z.; Michael Moseler. Molecular-Dynamics Simulation of Thin-Film Growth by Energetic Cluster Impact. *Physical Review B* **1995**, *51* (16), 11061.

(42) Rattunde, O.; Moseler, M.; Häfele, A.; Kraft, J.; Rieser, D.; Haberland, H. Surface Smoothing by Energetic Cluster Impact. *Journal of Applied Physics* **2001**, *90* (7), 3226.

(43) Peng, D. L.; Yamada, H.; Hihara, T.; Uchida, T.; Sumiyama, K. Dense Fe Cluster-Assembled Films by Energetic Cluster Deposition. *Appl. Phys. Lett.* **2004**, *85* (14), 2935–2937. https://doi.org/10.1063/1.1801170.

(44) Stoner, E. C.; Wohlfarth, E. P. A Mechanism of Magnetic Hysteresis in Heterogeneous Alloys. *Philosophical Transactions of the Royal Society of London. Series A, Mathematical and Physical Sciences* **1948**, *240* (826), 599–642. https://doi.org/10.1098/rsta.1948.0007.

(45) Peng, D. L.; Yamada, H.; Sumiyama, K.; Hihara, T.; Kumagai, K. Soft Magnetic Property and Magnetic Exchange Correlation in High-Density Fe-Co Alloy Cluster Assemblies. *Journal of Applied Physics* **2007**, *102* (3), 033917. https://doi.org/10.1063/1.2767247.

(46) Qi Yao; W. Liu, second; Z.D. Zhang. Effective Anisotropy Field in Anisotropic Nanostructured Ferromagnetic Materials. *physica status solidi (b)* **2009**, *246* (7), 1709–1715.

(47) Kaur, M.; McCloy, J. S.; Jiang, W.; Yao, Q.; Qiang, Y. Size Dependence of Inter- and Intracluster Interactions in Core–Shell Iron–Iron Oxide Nanoclusters. *J. Phys. Chem. C* **2012**, *116* (23), 12875–12885. https://doi.org/10.1021/jp301453w.

(48) Hoffmann, A.; Grimsditch, M.; Pearson, J. E.; Nogués, J.; Macedo, W. A. de A.; Schuller, I. K. Tailoring the Exchange Bias via Shape Anisotropy in Ferromagnetic/Antiferromagnetic Exchange-Coupled Systems. *Physical Review B* **2003**, *67* (22), 220406.

(49) Girgis, E.; Portugal, R. D.; Temst, K.; Haesendonck, C. V. Size and Shape Dependences on Magnetization Reversal in Ferromagnetic/Antiferromagnetic Bilayer Patterned into Nano-Dot Arrays. *J. Phys. D: Appl. Phys.* **2006**, *39* (9), 1733–1738. https://doi.org/10.1088/0022-3727/39/9/004.

(50) Eerenstein, W.; Palstra, T. T. M.; Hibma, T.; Celotto, S. Origin of the Increased Resistivity in Epitaxial ${\mathrm{Fe}}_{3}{\mathrm{O}}_{4}$ Films. *Phys. Rev. B* **2002**, *66* (20), 201101. https://doi.org/10.1103/PhysRevB.66.201101.

(51) Moraitakis, E.; Kompotiatis, L.; Pissas, M.; Niarchos, D. Permeability Measurements of Permalloy Films with a Broad Band Stripline Technique. *Journal of Magnetism and Magnetic Materials* **2000**, *222* (1), 168–174. https://doi.org/10.1016/S0304-8853(00)00560-6

Chapter 8: Summary and Conclusion

8.1. Project 1: Advanced Nano-sensor and Monitoring system of Radiation Detection for Nuclear energy Applications at High Temperature

This study contributes to the research in the area of identifying the thermal effects on nanomaterials, which induced changes in magnetic and structural behavior. In regard to this, investigations were carried out on magnetic nanomaterials to study the underlying mysteries behind heat-induced property changed in the material, which hinder the current generation nuclear reactor and to create materials that can have controlled property change at high temperature. In order to meet the objective, research was mainly focused on the study of magnetic and structural property changes in nanomaterials due to high temperature. As this field of research is directly related to nuclear energy and nanotechnology, a literature review was conducted and presented in this dissertation which uncovers the ongoing research and research so far in this field. Since previous results have already shown iron-based nanoparticle are very sensitive toward Si^{2+} irradiation and heavy ions like Si^{2+} behave as neutron in terms of the radiation effect and defect creation, these nanoparticles are best candidate material for the radiation sensing and monitoring radiation fluxes in the nuclear reactor. However, the core of the nuclear reactor possesses very high temperature (at least 500 ^{o}C), it is very crucial to investigate temperature induced structure-property relationship of the nanoparticle for possible application as radiation sensing materials for monitoring the radiation fluxes in the high temperature core of the nuclear reactor. Model nanoparticles (Fe_3O_4 and Fe-Fe_3O_4) for this study were prepared by using third generation cluster deposition technique. The nanoparticle granular films were then heat-treated up to 800 ^{o}C in different medium, such as argon, vacuum and oxygen. Both the types of nanoparticles showed stable morphology, phase and crystal structure in vacuum environment even at 800 ^{o}C. However, Fe at the core of Fe-Fe_3O_4 nanoparticle oxidized and showed mixed phase of Fe_3O_4 and Fe_2O_3, and Fe_3O_4 nanoparticles completely oxidize to Fe_2O_3 at 800 ^{o}C in argon and oxygen environments. Since, in most of the cases, cores of nuclear reactors are vacuum, the stable

structure and property of nanoparticles in vacuum at high temperature open new doors for application as radiation sensing material to monitor radiation fluxes in the high temperature core of nuclear reactors and could positively contribute to the assurance of enhanced safety of the future reactors.

8.2. Project 2: Advanced Magnetic Nanomaterials for Application of Ultrahigh Frequency Electronics

This research mainly contributes in the area of study of materials for their application as high frequency soft magnetic materials. The wireless network is rapidly progressing towards commercialization of 5G and development of 6G. Since the frequency spectrum of 5G and 6G ranges from few hundred megahertz to tens gigahertz (GHz), development of ultrahigh frequency compatible magnetic nanomaterials is critical. Further, the rise of internet of things, and demands for lighter, faster, and smarter devices that incorporate computing, communication, and sensing functionalities in highly miniaturized packages, integration of thin film magnetic core that has high saturation magnetization, uniaxial anisotropy, and high resistivity on an electronic circuit is very important. Previous research have shown that soft magnetic film with induced ellipsoidal core-shell nanoparticles integrated on to silicon microchips are very promising as passive components (such as inductor, transformer) on miniaturized electronic devices for ultrahigh frequency performance. However, existing technologies require high temperature annealing to induce uniaxial anisotropy, which is incompatible with the silicon integrated designs. In this work, we developed soft magnetic nanocomposite films by energetic impact of spherical and negatively charged Fe/Fe_3O_4 magnetic nanoparticles at room temperature prepared through a nanocluster deposition technique. We then directed them to energetically impact onto oblique Si substrates by applying positive voltage from 0-10 kV to the substrate. After the energetic impact the spherical shape of the NP changes to hemi-ellipsoidal shape and systematically studied the structural, magnetic and electrical properties. The change in shape made the soft magnetic nanocomposite films to induce in-plane uniaxial anisotropy along the longer axis. Result showed that good and adjustable uniaxial anisotropy and magnetic

softness have been obtained with the large resistivities demonstrating excellent potential for high-frequency performance up to 8.5 gigahertz in miniaturized electronic devices. The microstructural engineering and composition adjustments could offer new discoveries for future generation wireless network and electronic.

Appendix A: Publisher Permission for Chapter 2

JOHN WILEY AND SONS LICENSE
TERMS AND CONDITIONS

Feb 28, 2020

This Agreement between University of Idaho -- Lokendra Khanal ("You") and John Wiley and Sons ("John Wiley and Sons") consists of your license details and the terms and conditions provided by John Wiley and Sons and Copyright Clearance Center.

License Number	4777900636573
License date	Feb 28, 2020
Licensed Content Publisher	John Wiley and Sons
Licensed Content Publication	ENERGY TECHNOLOGY (ELECTRONIC)
Licensed Content Title	Advanced Nanomaterials for Nuclear Energy and Nanotechnology
Licensed Content Author	Lokendra R. Khanal, Jennifer A. Sundararajan, You Qiang
Licensed Content Date	Dec 13, 2019
Licensed Content Volume	0
Licensed Content Issue	0
Licensed Content Pages	23

Appendix B: Publisher Permission for Chapter 4

Copyright Clearance Center Marketplace™

IOP Publishing, Ltd - License Terms and Conditions

This is a License Agreement between Lokendra Raj Khanal ("You") and IOP Publishing, Ltd ("Publisher") provided by Copyright Clearance Center ("CCC"). The license consists of your order details, the terms and conditions provided by IOP Publishing, Ltd, and the CCC terms and conditions.

All payments must be made in full to CCC.

Order Date	02-Mar-2020	Type of Use	Republish in a thesis/dissertation
Order license ID	1020988-1		
ISSN	0022-3727	Publisher	IOP Publishing
		Portion	Page

LICENSED CONTENT

Publication Title	Journal of Physics D : Applied Physics	Country	United Kingdom of Great Britain and Northern Ireland
Author/Editor	Institute of Physics (Great Britain), Institute of Physics and the Physical Society.	Rightsholder	IOP Publishing, Ltd
		Publication Type	Journal
Date	12/31/1969		
Language	English		

REQUEST DETAILS

Portion Type	Page	Rights Requested	Main product
Page range(s)	255302	Distribution	Worldwide
Total number of pages	8	Translation	Original language of publication
Format (select all that apply)	Print	Copies for the disabled?	Yes
Who will republish the content?	Publisher, not-for-profit	Minor editing privileges?	Yes
Duration of Use	Life of current edition	Incidental promotional use?	No
Lifetime Unit Quantity	Up to 499	Currency	USD

NEW WORK DETAILS

Title	Advanced Magnetic Nanomaterials and Nanotechnology for Applications of Nuclear Radiation Detection and Ultrahigh Frequency Electronics	Institution name	University of Idaho
		Expected presentation date	2020-05-01
Instructor name	Dr. You Qiang		

ADDITIONAL DETAILS

Appendix C: Publisher Permission for Chapter 5

Relationship between nanostructure-magnetic property induced by temperature for iron oxide nanoparticles in vacuum, Ar and O2 environments

Author: Lokendra R. Khanal,Mostafa Ahmadzadeh,John S. McCloy,You Qiang

Publication: Journal of Magnetism and Magnetic Materials

Publisher: Elsevier

Date: 15 March 2020

Please note that, as the author of this Elsevier article, you retain the right to include it in a thesis or dissertation, provided it is not published commercially. Permission is not required, but please ensure that you reference the journal as the original source. For more information on this and on your other retained rights, please visit: https://www.elsevier.com/about/our-business/policies/copyright#Author-rights

BACK CLOSE WINDOW